POLYTECHNIC OF TURIN

Ph.D. Course in Aerospace Engineering

Ph.D. Thesis

External Aerodynamic Simulations in a Rotating Frame of Reference

Supervisors:

Prof. Renzo Arina	Candidate:
Dott. Ceresola Nicola	Filomena Cariglino
Ing. Pelizzari Emilio	

To my husband Gregorio and my daughter Mariarita.

To my parents, my brother and my grandmother Maria.

Acknowledgments

I thank my advisor Dr. Nicola Ceresola for his unyielding and invaluable support. He helped me work through numerous problems during my research. His ideas and suggestions form part of this dissertation. I thank the other members of my committee, for their kindness in answering questions I had for them, and for their very useful suggestions and comments. Without their teaching I would not have been able to obtain the numerical implementations presented here.

Secondly, I would like to thank my husband for his infinite patience, his support and to have always believed in my abilities and in the success of my training.

Finally, I would to thank my colleague Roberto Labruto for his precious suggestions and his support.

Index

List of Symbols

b =   generic scalar

$\vec{B}$ =   generic vector

c =   airfoil chord

$C_{(\blacksquare)}$ =   generic aerodynamic coefficient

C_l =   lift coefficient

C_m =   pitch moment coefficient

C_p =   pressure coefficient

$C_{(\blacksquare)_q}$ =   generic stability derivative

C_T =   coefficient thrust

D =   propeller diameter, [m]

E =   total energy per unit of mass, [J/kg]

e =   internal energy per unit of mass, []

$\vec{f_e}$ =   vector of external forces, [N]

$\vec{F_I}$ =   inviscid flux vector

$\vec{F_V}$ =   viscous flux vector

F, G, H = components of inviscid fluxes

F_v, G_v, H_v = components of viscous fluxes

J = advance ratio

M = Mach number

n = propeller rotational speed, [rps]

p = pressure, [Pa]

p, q, r = body roll rate, pitch rate, yaw rate, [rad/s]

q = pitch rate

$\hat{q}$ = normalized pitch rate ($qc/2V$)

q_i = heat flux, [W/m^2]

$\overrightarrow{Q_X}$ = source vector

$\vec{r}$ = position vector relative to the rotation center, [m]

t = time in physical space, [s]

T = effective thrust, [N]

$u_\infty, v_\infty, w_\infty$ = freestream velocity components, [m/s]

$\vec{v}, \vec{V}$ = velocity vector, [m/s]

$\overrightarrow{v_b}$ = rotational speed vector of the coordinate system, [m/s]

v_i = generic component of the velocity vector, [m/s]

$\vec{V_\infty}$ =   freestream velocity vector, [m/s]

v_1, v_2, v_3 =   components of velocity vector, [m/s]

W_f =   work of the external forces, [J]

$\vec{X}$ =   vector of conservative variables

x, y, z =   position vector components relative to the rotation center, [m]

x_c, y_c, z_c =   position vector components relative to the rotation center, [m]

α =   angle of attack

δ_{ij} =   Kroenecker symbol

ρ =   density, [kg/m³]

τ_{ij} =   generic component of the shear tensor, [Pa]

$\vec{\omega}$ =   rotational speed vector, [rad/sec]

$\omega_x, \omega_y, \omega_z$ =   components of rotational speed vector, [rad/s]

$\| \quad \|$ = norm of a vector

Abstract

This thesis presents the development of a tool integrated in the UNS3D code, proprietary of Alenia Aermacchi, for the simulation of external aerodynamic flow in a rotating reference frame, with the main objective of predicting propeller-aircraft integration effects. The equations in a rotating frame of reference have been formulated in terms of the absolute velocity components; in this way, the artificial dissipation needed for convergence is lessened, as the Coriolis source term is only introduced in the momentum equation and it is not necessary a transformation of the variables between the rotating and no rotating zones. An Explicit Algebraic Reynolds Stress turbulence model is used. A first assessment of effectiveness of this method is made computing stability derivatives of a NACA 0012 airfoil. Finally, steady Navier-Stokes and Euler simulations of a four-blade single-rotating propeller are presented, demonstrating the efficiency of the chosen approach in terms of computational cost.

Chapter I

Introduction

1. The analysis of unsteady fluid flows around moving bodies and boundaries

The present work is aimed at extending the features of an existing computational fluid dynamics solver (UNS3D) to the solution of fluid flows in unsteady geometric domains, thus basically around moving bodies and boundaries. Topics of noticeable and recent interest such as the study on the trails of single or contra-rotating propellers and fans, the secondary flows inside turbomachines, the aeroelastic flutter phenomena of wings, rotorcraft blades or even buildings and chimneys are all examples requiring moving domain capabilities inside the fluid dynamics solvers.

Despite the study of unsteady flows has always been of primary importance since the dawn of computational fluid dynamics, the analysis of the flows around moving bodies and boundaries grew a noticeable spread only later on: even if several theoretical results for the analytical solutions have been already available since prewar studies, the lack of an adequate scientific background on numerical approaches and moreover the limited computational speeds available have always been critical issues to overcome. Other potential issues were the need of unsteady boundary conditions, for which adequate support by the numerical solver

had to be developed, and even transient initial conditions, for which further preliminary calculations were necessary, thus improving the criticism of computational powers available.

Nowadays, methods for the treatment of moving domains are more and more commonly available both in commercial and academic solvers and so the study of fluid flows around or inside moving domains is finally widespread both in the research field and in the development and design fields. The support for unsteady geometries is therefore a more and more compelling requirement for the vast majority of both specialized and non-specialized solvers, and a noticeable interest is also gathered around the look for a best possible approach in terms of computational quickness, flexibility, robustness, reliability and overall simplicity.

2. Structure of the work

The thesis is divided into five chapters. In the present introductory Chapter I, we present the main approaches for treating moving domains in Computational Fluid Dynamics solvers, some of their prominent advantages and drawbacks, the reasons behind the choices of Moving Reference Frame method as subject of this work, the global organization of the work and its objectives.

Chapter II is a development of the governing equations in non-inertial frame system that are applicable to compressible, unsteady, three-dimensional viscous flows. The method for including the non-inertial frame terms into an existing absolute frame solver (UNS3D) are presented in this chapter.

Chapter III presents the solution methodology and the basic structure of UNS3D program.

Chapter IV is dedicated to results. Two applications are presented: the first application is the determination of the stability derivatives for a NACA 0012 airfoil and the latter is the simulation of the flow field around a rotating propeller. The first application allows us to assess the method by comparing the results to a reference test case, for which several authors have obtained a solution [9, 10, 11]. In this case the flow field is computed using Euler equations. The second application is a more complex test case, which has the purpose to evaluate the accuracy, efficiency and robustness of the current method to predict the complex flow field of a rotating propeller. For this test case a comparison with experimental results for cruise conditions in terms of thrust coefficient is also made.

Chapter V is devoted to conclusions and suggestions for future work.

3. Overview of the presently available numerical strategies

Considering all the possible variations, the number of proposed numerical methods to account for the domain movement available in the literature is noticeable. By restricting the search around some topical tasks, among which are the study of rotating propeller blades, turbomachines channels and wings in flutter, the possible numerical approaches are the following:

- a pure Lagrangian solver, with body movement achieved thanks to the assignment of strict boundary conditions. The theoretical literature behind is vast, and other main advantages are that the domain deformations and movement are inborn features and so is also the study of "free surface" problems. The drawbacks are the constant need for untangling, remeshing and remapping of the fluid field, even for

steady domains, the delicate and complex cell centered finite volume formulation and the degradation on the shape of the bodies/boundaries after several iterations;

- a Moving Reference Frame rigidly fixed on the moving body, for which the solver must correctly handle the additional non-inertial forces. The critical advantages are the very simple theoretical formulation, the complete absence of mesh updates and remeshing steps. Among the drawbacks we must consider that only rigid movements can be achieved (at least in the presently selected and developed version of MRF), that the whole domain is moving so mutual relative movements are only available as boundary conditions, that the additional contributes are in the form of source terms, thus potentially introducing additional errors, and that the analysis input and outputs must be defined in the relative reference system, so transformation routines will be needed;

- an Arbitrary Lagrangian-Eulerian approach, that enables free mesh movement thanks to the introduction of additional flux terms in the solver to account for it. It statedly combines the advantages of Eulerian and Lagrangian approaches while attempting at minimizing their drawbacks. It is therefore credited as ideal for fluid-body interaction studies, but depending on the formulation can manifest great versatility and flexibility and can also neglect remeshing in selected cases. Recognized disadvantages are the vastness of the family of methods laying behind the same name, the usefulness of remeshing and remapping capabilities to prevent degraded performances and solution qualities, and the complexity of free surface modeling, contrary to the pure Lagrangian methods;

- an over-set grid method, such as "Chimera", that allows domain movement thanks to the relative movement of the grids, but requiring an intensive solver's source

code rewriting and a more complex preliminary treatment of the analysis cases, thus falling beyond the frames of the present work.

Among the discussed possible choices, the Moving Reference Frame has been selected, developed, validated and tested since they stately offered the best features increase while being integrally compatible with the original solver's source code. As well promptly explain later on, limited version of the Moving Reference Frame extension has been chosen and developed in the present work. More precisely, only a rigid non-inertial Moving Reference Frame has been adopted, avoiding the theoretical and practical complexity of a non-rigid frame, which could grant only limited further functionality improvements.

Chapter II

The Moving Reference Frame Approach

1. Preliminary considerations

As previously stated in the general introduction, a very basic method providing a reliable way to account for moving geometries in the computational domain is known as the "Moving Reference Frame" approach, for which we actually move the whole study in a non-inertial relative reference system. Even if not mathematically complex, the Moving Reference Frame approach can already provide a significant functionality improvement to the CFD solver, since it enables a thorough study of fluid flows around bodies or boundaries in rigid motion, the latter being a three-dimensional accelerating or oscillating rotation or translation, while avoiding mesh deformations issues completely.

2. The non-inertial MRF for moving geometries

A consistent CFD study of rotating or oscillating bodies such as propellers and flutter studies for airfoils or finite three-dimensional rigid wings can be easily performed by simply introducing the rigid motion as a parameter for the analysis of the fixed mesh containing the

aforesaid body/boundary. The solver will in fact work in a relative observer's perspective, evaluating the fluid field in a single mesh representing a fixed domain, thus around fixed bodies and boundaries; those latter, thanks to the introduction of the non-inertial terms in the solver's equations, will actually correspond to moving geometries in the inertial perspective. The only significant limitation of the MRF for moving geometries is that a single global rigid law of motion must be inferred for all the bodies in the domain, that are actually rigid boundaries in the mesh. Some improvements may be obtained by using an expanded set of source terms for the fluid dynamics equations, including expansion/contraction terms that may account for some relative motion between the rigid boundaries, but the mathematical complexity of the MRF parameters will raise quickly for very little practical advantage, so other methods may be more profitably used instead.

3. The non-inertial MFR for large translational velocities

The Moving Reference Frame approach counts another less manifest feature: a very large global component in fluid motion, like in "Hubble flows" and among high Mach number problems generally, is usually source of significant numerical errors in a traditional inertial reference frame study. The ratio between the thermal energy and the kinetic energy is in fact extremely small due to the superimposed global motion, so the numerical solution in a floating point environment will manifest large errors on the thermal energy and thus on the pressure field, compromising the quality of velocity and density solutions too. In the Moving Reference Frame approach, the global motion is completely detracted from the numerical computation, so that even very little local variations can be observed and precisely calculated. This aspect puts the Moving Reference Frame approach in maximum consideration for

astrophysical and plasma nuclear magneto fluid-dynamics studies: rotating, expanding or contracting fluid flows in accelerating volumes, rotating ducts, collapsing stellar cores and pyrotechnic or supernovae explosions, or even in Inertial Confinement Fusion (ICF) problems can be successfully studied in a consistent, precise and much simpler way [16].

The aforesaid feature correspond, on the other hand, to another minor disadvantage for the MRF analysis of moving bodies: big domains will easily grow large fictitious advective components even for slow angular velocities, thus degrading the quality of the real solution in the absolute reference frame.

4. Basic concepts and setbacks of the MRF approach

In a Moving Reference Frame analysis, a full reference frame transformation is actually done and not a simple coordinate transformation like in Moving Mesh methods (among which the Arbitrary Lagrangian Eulerian can be included): both the solver inputs, the variables and the outputs becomes integrally relative, and not just in the sense they are functions of a new relative coordinate system, like in the Moving Mesh approaches. While conceptually more complicated, the development setbacks are pretty straightforward: while casting the governing equations to describe the flow in a non-inertial frame there are two choices regarding the velocity vector. Either it can be the velocity vector with respect to the inertial reference frame [1, 17], hereafter called the absolute velocity vector for brevity, or it can be the velocity vector with respect to the non-inertial reference frame [18], hereafter called the relative velocity vector for brevity. Depending upon this choice various formulations result. Therefore, developing a Moving Reference Frame extension to the solver will initially consist, as we will discuss further on, in the simple introduction of the non-inertial terms, such as

fictitious forces and expansion/contraction effects, in the original Euler/Navier-Stokes equations. As already stated previously, by adopting this basic technique alone any mesh update is actually neglected, at least at the beginning: mathematical and development complexities and computational time will then be noticeably lower than in other methods. On the other hand, if analysis input parameters and output requirements are in the absolute reference frame, which is a very typical case, the development of transformations from/to the solver's now relative reference system will be needed. These transformations are not necessary if the Navier-Stokes equations are formulated in a non-inertial reference frame in terms of absolute velocity. This approach has the advantages to use a steady-state formulation, if the flow field can be viewed as a steady state in the reference frame. Thus, many efficient acceleration techniques, such as local time stepping and multigrid method, can be used.

This section will aim at the determination and explanation of the Navier-Stokes equations formulations in terms of absolute velocities and the additional terms, derived from this choice.

5. Governing equations

5.1. Derivation of the Navier-Stokes equations in a non-inertial reference frame

Considering a material point P seen from both an inertial frame "1" and a non-inertial frame "2", and accounting for both the translation and the rotation of frame "2", the following kinematical relations can be obtained:

$$\overrightarrow{r_{1P}}(t) = \overrightarrow{r_{12}}(t) + \overrightarrow{r_{2P}}(t) \tag{1}$$

Deriving this equation in time twice, we obtain the relation for the velocity and the acceleration:

$$\overrightarrow{V_{1P}} = \overrightarrow{V_{12}} + \vec{V} + \vec{\omega} \times \overrightarrow{r_{2P}} \tag{2}$$

$$\overrightarrow{a_{1P}} = \overrightarrow{a_{12}} + \overrightarrow{a_{2P}} + 2\vec{\omega} \times \overrightarrow{u_{2P}} + \vec{\omega} \times \vec{\omega} \times \overrightarrow{r_{2P}} + \dot{\vec{\omega}} \times \overrightarrow{r_{2P}} \tag{3}$$

It is then convenient to rename the variables as follows :

$$\overrightarrow{V_{1P}} = \vec{V} \tag{4}$$

$$\overrightarrow{V_{12}} = \overrightarrow{V_r} \tag{5}$$

$$\overrightarrow{V_{2P}} = \overrightarrow{V_0} \tag{6}$$

$$\overrightarrow{r_{2P}} = \vec{r} \tag{7}$$

The material acceleration in a non-inertial reference frame can then be written as follows:

$$\overrightarrow{V_r} = \vec{V} - \overrightarrow{V_0} - 2\vec{\omega} \times \overrightarrow{V_0} - \vec{\omega} \times \vec{\omega} \times \vec{r} - \dot{\vec{\omega}} \times \vec{r} \tag{8}$$

where:

- $\vec{V_0}$ is the frame "2" linear acceleration,

- $2\vec{\omega} \times \vec{V_0}$ is the "Coriolis acceleration",

- $\vec{\omega} \times \vec{\omega} \times \vec{r}$ is the "centrifugal acceleration",

- $\vec{\omega} \times \vec{r}$ is due to the frame "2" angular acceleration.

The additional fictitious forces that account for both the translation and the rotation of the non-inertial frame will then be:

$$-\rho \vec{V_0} - 2\rho\vec{\omega} \times \vec{V_0} - \rho\vec{\omega} \times \vec{\omega} \times \vec{r_{2P}} - \rho\vec{\omega} \times \vec{r} \qquad (9)$$

that is, four negative contributes in the right hand side of the momentum equation.

By simply scalar multiplication for the velocity vector, the aforesaid additional momentum terms give birth, in turn, to subsequent energy terms:

$$-\rho\vec{V_0}\vec{V_0} - 2\rho\vec{V_0}\left(\vec{\omega} \times \vec{V_0}\right) - \rho\vec{V_0}\left(\vec{\omega} \times \vec{\omega} \times \vec{r}\right) - \rho\vec{V_0}\left(\vec{\omega} \times \vec{r}\right) \qquad (10)$$

5.2. Original system of Navier-Stokes equations

The Navier-Stokes equations in a inertial frame of reference are expressed as:

$$\frac{\partial \vec{X}}{\partial t} + \nabla \vec{F_I} - \nabla \vec{F_V} = 0 \qquad (11)$$

where $\vec{X}$ is defined as:

$$\vec{X} = \begin{bmatrix} \rho \\ \rho\vec{V} \\ \rho E \end{bmatrix} \qquad (12)$$

$\overrightarrow{F_I}$ and $\overrightarrow{F_V}$ are the respective flux vectors:

$$F_{Ii} = \begin{bmatrix} \rho V_i \\ \rho V_1 V_i + p\delta_{1i} \\ \rho V_2 V_i + p\delta_{2i} \\ \rho V_3 V_i + p\delta_{3i} \\ (\rho E + p)V_i \end{bmatrix} \tag{13}$$

$$F_{Vi} = \begin{bmatrix} 0 \\ \tau_{i1} \\ \tau_{i2} \\ \tau_{i3} \\ q_i + V_j \tau_{ij} \end{bmatrix} \tag{14}$$

The system of Euler equations will not be explicitly described since it can always be considered a sub-case of the Navier-Stokes system and all the subsequent analytical achievements are valid in both the cases.

5.3. Navier-Srokes equations in a non-inertial reference frame (relative velocities)

By introducing the formerly deferred additional non-inertial terms in both the momentum and the energy equations, the original system of Navier-Stokes equations become:

$$\begin{cases} \dfrac{\partial \rho}{\partial t} + \nabla \cdot \left(\rho \vec{V_r}\right) = 0 \\[2mm] \dfrac{\partial \rho \vec{V_r}}{\partial t} + \nabla \cdot \left[\rho \vec{V_r} \times \vec{V_r} + p\bar{\bar{I}} - \bar{\bar{\tau}}\right] = -\rho\vec{\omega} \times (\vec{\omega} \times \vec{r}) \quad \Leftarrow \; centrifugal\ force \\ \hspace{5cm} - 2\rho\vec{\omega} \times \vec{V_r} \quad \Leftarrow \; Coriolis\ force \\ \hspace{5cm} -\rho\dot{\vec{\omega}} \times \vec{r} \quad \Leftarrow \; unsteadness\ (rotational) \\ \hspace{5cm} -\rho\vec{V_0} \quad \Leftarrow \; translational\ inertia \\ \dfrac{\partial \rho E_r}{\partial t} + \nabla \cdot \left[(\rho E_r + p)\vec{V_r} - \bar{\bar{\tau}} \cdot \vec{V_r} - k_T \nabla T\right] = -\rho\vec{V_r} \cdot (\vec{\omega} \times (\vec{\omega} \times \vec{r})) \\ \hspace{6cm} - 2\rho\vec{V_r} \cdot \left(\vec{\omega} \times \vec{V_r}\right) \\ \hspace{6cm} -\rho\vec{V_r} \cdot \left(\dot{\vec{\omega}} \times \vec{r}\right) \\ \hspace{6cm} -\rho\vec{V_r} \cdot \vec{V_0} \end{cases} \tag{15}$$

E_r is the total energy per unit of mass as seen from a non-inertial frame:

$$E_r = e + \frac{1}{2}\, \vec{V_r} \cdot \vec{V_r} \tag{16}$$

5.4. Navier-Stokes equations in a non-inertial reference frame (absolute velocities)

To express the Equation (11) in terms of a relative reference frame and using the absolute velocities, the following relations for substantial and local derivatives are used:

$$\frac{Db}{Dt} = \frac{D'b}{Dt'} \tag{17}$$

$$\frac{DB}{Dt} = \frac{D'B}{Dt'} + \vec{\omega} \times \vec{B} \tag{18}$$

$$\frac{\partial b}{\partial t} = \frac{\partial' b}{\partial t'} - \left(\vec{V_0} + \vec{\omega} \times \vec{r}\right) \cdot \nabla b \tag{19}$$

$$\frac{\partial B}{\partial t} = \frac{\partial' B}{\partial t'} - \left(\vec{V_0} + \vec{\omega} \times \vec{r}\right) \cdot \nabla \vec{B} + \vec{\omega} \times \vec{B} \tag{20}$$

where the prime ' denotes the operation with respect to the relative reference frame. By using relations (17) – (20), the right hand side of Equation (11) becomes

$$\vec{Q_X} = \begin{bmatrix} 0 \\ -\rho(\vec{\omega} \times \vec{V}) \\ 0 \end{bmatrix} \tag{21}$$

With this formulation, the source term vector (Equation (21)) contains only the contribution of the Coriolis force and the contribution of the centrifugal force is omitted. In this way the magnitude of the source term is greatly reduced and a smaller amount of artificial dissipation is required to ensure convergence.

23

To take into account the rotation and the translation of the coordinate system, Equation (13) is modified in the following way:

$$F_{Ii} = \begin{bmatrix} \rho V_i \\ \rho V_1(V_i - v_{b_i}) + p\delta_{1i} \\ \rho V_2(V_i - v_{b_i}) + p\delta_{2i} \\ \rho V_3(V_i - v_{b_i}) + p\delta_{3i} \\ (\rho E + p)V_i \end{bmatrix} \tag{22}$$

where $\vec{v_b}$ is defined as:

$$\vec{v_b} = \vec{V_0} + \vec{\omega} \times \vec{r} \tag{23}$$

Therefore the Navier-Stokes equations, in differential form, became:

$$\begin{cases} \dfrac{\partial \rho}{\partial t} + \nabla \cdot (\rho \vec{V}) = 0 \\[2mm] \dfrac{\partial \rho \vec{V}}{\partial t} + \nabla \cdot [\rho \vec{V} \times (\vec{V} - \vec{v_b}) + p\bar{\bar{I}} - \bar{\bar{\tau}}] = -\rho \vec{\omega} \times \vec{V} \qquad \Leftarrow \; Coriolis\; force \\[2mm] \dfrac{\partial \rho E}{\partial t} + \nabla \cdot [(\rho E + p)\vec{V} - \bar{\bar{\tau}} \cdot \vec{V} - k_T \nabla T] = 0 \end{cases} \tag{24}$$

5.4.1. Conservative Form of the Governing Equations

The non-inertial Navier Stokes equations (24) can be written in the Cartesian coordinate system x, y, z of the non-inertial reference frame in the following compact form:

$$\frac{\partial \vec{X}}{\partial t} + \frac{\partial \vec{F}}{\partial x} + \frac{\partial \vec{G}}{\partial y} + \frac{\partial \vec{H}}{\partial z} = \vec{Q_X} + \frac{\partial \vec{F_v}}{\partial x} + \frac{\partial \vec{G_v}}{\partial y} + \frac{\partial \vec{H_v}}{\partial z} \tag{25}$$

where $\vec{X}$ is defined as

$$\vec{X} = \begin{bmatrix} Q_1 \\ Q_2 \\ Q_3 \\ Q_4 \\ Q_5 \end{bmatrix} = \begin{bmatrix} \rho \\ \rho V_1 \\ \rho V_2 \\ \rho V_3 \\ \rho E \end{bmatrix} \tag{26}$$

Here

$$\vec{F} = \begin{bmatrix} \rho V_1 \\ \rho V_1(V_1 - (V_{0_1} + \omega_y z - \omega_z y)) + p \\ \rho V_1(V_2 - (V_{0_2} + \omega_z x - \omega_x z)) \\ \rho V_1\left(V_3 - (V_{0_3} + \omega_x y - \omega_y x)\right) \\ V_1(\rho E + p) \end{bmatrix} \quad ; \quad \vec{F_v} = \begin{bmatrix} 0 \\ \tau_{xx} \\ \tau_{xy} \\ \tau_{xz} \\ \tau_{xx}V_1 + \tau_{xy}V_2 + \tau_{xz}V_3 + k_T \dfrac{\partial T}{\partial x} \end{bmatrix} \quad (27)$$

$$\vec{G} = \begin{bmatrix} \rho V_2 \\ \rho V_2(V_1 - (V_{0_1} + \omega_y z - \omega_z y)) \\ \rho V_2(V_2 - (V_{0_2} + \omega_z x - \omega_x z)) + p \\ \rho V_2(V_3 - (V_{0_3} + \omega_x y - \omega_y x)) \\ V_2(\rho E + p) \end{bmatrix} \quad ; \quad \vec{G_v} = \begin{bmatrix} 0 \\ \tau_{yx} \\ \tau_{yy} \\ \tau_{yz} \\ \tau_{yx}V_1 + \tau_{yy}V_2 + \tau_{yz}V_3 + k_T \dfrac{\partial T}{\partial y} \end{bmatrix} \quad (28)$$

$$\vec{H} = \begin{bmatrix} \rho V_3 \\ \rho V_3(V_1 - (V_{0_1} + \omega_y z - \omega_z y)) \\ \rho V_3(V_2 - (V_{0_2} + \omega_z x - \omega_x z)) \\ \rho V_3(V_3 - (V_{0_3} + \omega_x y - \omega_y x)) + p \\ V_3(\rho E + p) \end{bmatrix} \quad ; \quad \vec{H_v} = \begin{bmatrix} 0 \\ \tau_{zx} \\ \tau_{zy} \\ \tau_{zz} \\ \tau_{zx}V_1 + \tau_{zy}V_2 + \tau_{zz}V_3 + k_T \dfrac{\partial T}{\partial z} \end{bmatrix} \quad (29)$$

are the components of the conservative and viscous fluxes and $\vec{Q}_X$, for the formulation in terms of absolute velocities, is given by:

$$\vec{Q_X} = \begin{bmatrix} 0 \\ -\rho(\omega_y V_3 - \omega_z V_2) \\ -\rho(\omega_z V_1 - \omega_x V_3) \\ -\rho(\omega_x V_2 - \omega_y V_1) \\ 0 \end{bmatrix} \quad (30)$$

An important thing to be noted here is that, except for the source term $\vec{Q_X}$, the functional form of the non-inertial Navier-Stokes equations is similar to the functional form of the standard conservative equations defined for inertial reference frames and including the Algebraic Lagrangian Eulerian (ALE) approach for generalized motion of the grid. Therefore, it is possible to implement a conservative formulation in terms of the conservative variables $\vec{X}$ defined in Equation (26) and the introduction of the ALE approach permits a local application of the non-inertial frame of reference as a building block in a more complex configuration framework, without any interface between the non-inertial and inertial part of the same mesh, because this formulation guarantees the flux conservation.

Let's start by showing that all the physical variables and fluxes can be re-written in terms of the conservative variables Q. From equation (26) one gets that

$$\rho = Q_1 \tag{31}$$

$$V_1 = \frac{Q_2}{Q_1}; \qquad V_2 = \frac{Q_3}{Q_1}; \qquad V_3 = \frac{Q_4}{Q_1} \tag{32}$$

$$E = \frac{Q_5}{Q_1} \tag{33}$$

$$e = \frac{Q_5}{Q_1} - \frac{1}{2}\left[\left(\frac{Q_2}{Q_1}\right)^2 + \left(\frac{Q_3}{Q_1}\right)^2 + \left(\frac{Q_4}{Q_1}\right)^2\right]. \tag{34}$$

According to the principles of thermodynamics the temperature can be given in terms of the internal energy and density, and as a consequence for any fluid, the temperature can also be written in terms of the conserved quantities Q_i. A similar fact is true for the static pressure p and the speed of sound a since by the state equation, they are functions of the temperature and density only. In particular if the fluid is given by a (calorically perfect) gas one can write

$$e = c_v T; \qquad p = (\gamma - 1)\rho e; \qquad c = \sqrt{\gamma R T} \tag{35}$$

$$V = \sqrt{V_1^2 + V_2^2 + V_3^2}; \qquad M = \frac{V}{c} \tag{36}$$

and as a consequence:

$$T = \frac{Q_5}{c_v Q_1} - \frac{1}{2c_v}\left[\left(\frac{Q_2}{Q_1}\right)^2 + \left(\frac{Q_3}{Q_1}\right)^2 + \left(\frac{Q_4}{Q_1}\right)^2\right] \tag{37}$$

$$p = (\gamma - 1)Q_1\left(\frac{Q_5}{Q_1} - \frac{1}{2}\left[\left(\frac{Q_2}{Q_1}\right)^2 + \left(\frac{Q_3}{Q_1}\right)^2 + \left(\frac{Q_4}{Q_1}\right)^2\right]\right) \tag{38}$$

$$E + \frac{p}{\rho} = \frac{\gamma Q_5}{Q_1} - \frac{(\gamma - 1)}{2}\left[\left(\frac{Q_2}{Q_1}\right)^2 + \left(\frac{Q_3}{Q_1}\right)^2 + \left(\frac{Q_4}{Q_1}\right)^2\right] \tag{39}$$

Using equations (31)-(39) one can write the conservative flux vectors as

$$\vec{F} = \begin{bmatrix} Q_2 \\ Q_2\left(\frac{Q_2}{Q_1} - (V_{0_1} + \omega_y z - \omega_z y)\right) + (\gamma-1)Q_1\left(\frac{Q_5}{Q_1} - \frac{1}{2}\left[\left(\frac{Q_2}{Q_1}\right)^2 + \left(\frac{Q_3}{Q_1}\right)^2 + \left(\frac{Q_4}{Q_1}\right)^2\right]\right) \\ Q_2\left(\frac{Q_3}{Q_1} - (V_{0_2} + \omega_z x - \omega_x z)\right) \\ Q_2\left(\frac{Q_4}{Q_1} - (V_{0_3} + \omega_x y - \omega_y x)\right) \\ \frac{Q_2}{Q_1}\left(\frac{\gamma Q_5}{Q_1} - \frac{(\gamma-1)}{2}\left[\left(\frac{Q_2}{Q_1}\right)^2 + \left(\frac{Q_3}{Q_1}\right)^2 + \left(\frac{Q_4}{Q_1}\right)^2\right]\right) \end{bmatrix} \quad (40)$$

$$\vec{G} = \begin{bmatrix} Q_3 \\ Q_3\left(\frac{Q_2}{Q_1} - (V_{0_1} + \omega_y z - \omega_z y)\right) \\ Q_3\left(\frac{Q_3}{Q_1} - (V_{0_2} + \omega_z x - \omega_x z)\right) + (\gamma-1)Q_1\left(\frac{Q_5}{Q_1} - \frac{1}{2}\left[\left(\frac{Q_2}{Q_1}\right)^2 + \left(\frac{Q_3}{Q_1}\right)^2 + \left(\frac{Q_4}{Q_1}\right)^2\right]\right) \\ Q_3\left(\frac{Q_4}{Q_1} - (V_{0_3} + \omega_x y - \omega_y x)\right) \\ \frac{Q_3}{Q_1}\left(\frac{\gamma Q_5}{Q_1} - \frac{(\gamma-1)}{2}\left[\left(\frac{Q_2}{Q_1}\right)^2 + \left(\frac{Q_3}{Q_1}\right)^2 + \left(\frac{Q_4}{Q_1}\right)^2\right]\right) \end{bmatrix} \quad (41)$$

$$\vec{H} = \begin{bmatrix} Q_4 \\ Q_4\left(\frac{Q_2}{Q_1} - (V_{0_1} + \omega_y z - \omega_z y)\right) \\ Q_4\left(\frac{Q_3}{Q_1} - (V_{0_2} + \omega_z x - \omega_x z)\right) \\ Q_4\left(\frac{Q_4}{Q_1} - (V_{0_3} + \omega_x y - \omega_y x)\right) + (\gamma-1)Q_1\left(\frac{Q_5}{Q_1} - \frac{1}{2}\left[\left(\frac{Q_2}{Q_1}\right)^2 + \left(\frac{Q_3}{Q_1}\right)^2 + \left(\frac{Q_4}{Q_1}\right)^2\right]\right) \\ \frac{Q_4}{Q_1}\left(\frac{\gamma Q_5}{Q_1} - \frac{(\gamma-1)}{2}\left[\left(\frac{Q_2}{Q_1}\right)^2 + \left(\frac{Q_3}{Q_1}\right)^2 + \left(\frac{Q_4}{Q_1}\right)^2\right]\right) \end{bmatrix} \quad (42)$$

In a similar way, the viscous fluxes $\vec{F}_v$, $\vec{G}_v$ and $\vec{H}_v$ can be expressed as functions of the conservative quantities.

Using equations (31)- (39) in (30), $\vec{Q}_X$ can also be expressed in terms of the conservative variables as:

$$\vec{Q}_X = \begin{bmatrix} 0 \\ -(\omega_y Q_4 - \omega_z Q_3) \\ -(\omega_z Q_2 - \omega_x Q_4) \\ -(\omega_x Q_3 - \omega_y Q_2) \\ 0 \end{bmatrix} \tag{43}$$

5.4.2. Integral Formulation of the Navier-Stokes Equations

Integrating the conservative form of the non-inertial Navier-Stokes equations around a finite volume V enclosed by a surface S one gets:

$$\begin{cases} \dfrac{d}{dt}\displaystyle\int_V \rho \, dV + \oint_S \rho\vec{V} \, d\vec{S} = 0 \\ \dfrac{d}{dt}\displaystyle\int_V \rho\vec{V} \, dV + \oint_S \rho\vec{V}(\vec{V} - \vec{v}_b) \, d\vec{S} + \oint_S (p\bar{\bar{I}} - \bar{\bar{\tau}})d\vec{S} = -\int_V \vec{\omega} \times \rho\vec{V} \, dV \\ \dfrac{d}{dt}\displaystyle\int_V \rho E \, dV + \oint_S \rho E\vec{V} \, d\vec{S} - \oint_S (\vec{V}\bar{\bar{\tau}} + k_T \nabla T) \, d\vec{S} = 0 \end{cases} \tag{44}$$

This equations can be written in a compact form, in the following way:

$$\frac{\partial}{\partial t} \int_V \vec{X} \, dV + \oint_S (\vec{F_I} - \vec{F_V}) \, d\vec{S} = \int_V \vec{Q}_X \, dV \tag{45}$$

5.4.3. Non-Dimensional Form of the Navier-Stokes Equations in Non-Inertial Reference Frame

The form of the above equations remains unchanged if an appropriate non-dimensionalization is performed. As a consequence, equations (24) can also be considered as the no dimensional non-inertial Navier-Stokes equations. For example, if the non-dimensional

variables (denoted with an asterix: *) are defined in terms of reference (far-field) conditions (denoted with the "∞" symbol) and a reference length l as:

$$\vec{V} = V_\infty \vec{V^*}; \qquad \vec{r} = l\vec{r^*}; \qquad t = \frac{l}{V_\infty}t^*; \qquad \vec{\omega} = \frac{V_\infty}{l}\vec{\omega^*} \qquad (46)$$

$$\rho = \rho_\infty \rho^*; \qquad p = \rho_\infty V_\infty^2 p^*; \qquad T = T_\infty T^*; \qquad e = V_\infty^2 e^*; \qquad \mu = \mu_\infty \mu^* \qquad (47)$$

The non-dimensional equations are obtained simply by replacing each variable by its corresponding non-dimensional variable. Parameters including the viscosity coefficient μ, the thermal conduction coefficient k_T and the specific heat at constant volume c_v should be replaced by:

$$\mu \rightarrow \frac{\mu^*}{Re_\infty} \qquad (48)$$

$$k_T \rightarrow \frac{k_T T_\infty}{l^2} \frac{1}{\rho_\infty V_\infty^2} \frac{l}{V_\infty} = \frac{\mu^*}{Re_\infty \, Pr \, M_\infty^2 [\gamma - 1]} \qquad (49)$$

$$c_v \rightarrow \frac{c_v T_\infty}{V_\infty^2} = \frac{c_v \, \gamma \, R T_\infty}{\gamma [c_p - c_v] V_\infty^2} = \frac{c_v}{\gamma [c_p - c_v] M_\infty^2} = \frac{1}{\gamma [\gamma - 1] M_\infty^2} \qquad (50)$$

where $Re_\infty = \frac{\rho_\infty V_\infty l}{\mu_\infty}$ is the Reynolds number, $Pr = \frac{\mu c_p}{k_T}$ is the Prandtl number and $M_\infty = \frac{V_\infty}{c_\infty}$ is the Mach number.

6. Kinematics

By adopting relative dynamics, we have just discovered the appearance of new terms which are function of either the velocity or the acceleration, and yet even in the successive developments of transformation routines we realistically observe the contemporary presence of velocity and acceleration vectors. This fact alone has very important setbacks: as well known, angular acceleration vector is the first time derivative of the angular velocity vector, so the first one is completely known as soon as the second is. A single time derivation step links the two, but from the development point of view this isn't so trivial: computers don't have an inborn derivation capability. They can be "taught" derivation in two possible way:

- finite numerical derivation
- symbolic analytical derivation

Both of them are widely and successfully undertaken, but hide some drawbacks: the numerical derivation forcefully gives rise to computational errors that depend on the derivation algorithm, on the step and on the to-be-derived function but can't be fully overcome, whereas the symbolic analytical derivation requires a very extensive development, even if an already available mathematical library is going to be used, and this would fall seriously beyond the goals of the proposed work. Two remaining choices were left:

- the end user's supply of both the velocity and acceleration symbolic relations as analysis input parameters
- providing a limited set of kinematical cases for which the symbolic relations for both position, velocity and acceleration are hard-coded in their exact form

The first choice isflaw-vulnerable since no verification is performed on the correctness and coherence of the input functions, so problems di-cult to discover and unexpected results may appear. The second choice was therefore pursued.

6.1. Constant translational acceleration

The linear translation case is pretty straightforward: the moving reference frame is undergoing a single constant acceleration vector that will develop its initial velocity vector. There is no dependence from the initial position, that is therefore omitted. We then obtain the well-known uniformly accelerated motion:

$$
\begin{aligned}
s(t) &= v_0 + \frac{1}{2} at^2 \\
\dot{s}(t) &= v_0 + at \\
\ddot{s}(t) &= a
\end{aligned}
\tag{51}
$$

The only active MRF source terms will be the translational inertia term in the momentum equation, written in terms of relative velocity, and its corresponding one in the energy equation, whereas in the other formulation, all the sources terms are inactive.

6.2. Constant rotation

A constant initial angular velocity is the only free parameter for the constant rotational speed case. As before, there is no dependence from the initial position.

$$
\begin{aligned}
\vartheta(t) &= \omega t \\
\dot{\vartheta}(t) &= \omega \\
\ddot{\vartheta}(t) &= 0
\end{aligned}
\tag{52}
$$

The only active MRF formulation, using relative velocity, source terms will be the centrifugal and Coriolis forces in the momentum equation and their corresponding ones in the energy equation and if we consider the MFR formulation with the absolute velocity, the unique source term, which represents the Coriolis force, is present.

6.3. Oscillating translation

The translational oscillation case incorporates also the constant acceleration and initial velocity vectors. Again, there is no dependence from the initial position. The equations are as follows:

$$
\begin{aligned}
s(t) &= v_0 + \frac{1}{2} at^2 + A \sin\left(\frac{2\pi}{T}t + \varphi\right)\hat{\xi} \\
\dot{s}(t) &= v_0 + at + A\frac{2\pi}{T}\cos\left(\frac{2\pi}{T}t + \varphi\right)\hat{\xi} \\
\ddot{s}(t) &= a - A\frac{4\pi^2}{T^2}\sin\left(\frac{2\pi}{T}t + \varphi\right)\hat{\xi}
\end{aligned}
\tag{53}
$$

Despite the complexity of the law of motion, the only MRF source term active is the same of the constant translation acceleration case.

6.4. Oscillating rotation

The rotational oscillation case includes the constant rotation case too. As usual, there is no dependence from the initial position. The equations are then:

$$
\begin{aligned}
\vartheta(t) &= \omega t + A \sin\left(\frac{2\pi}{T}t + \varphi\right)\hat{\xi} \\
\dot{\vartheta}(t) &= \omega + A\frac{2\pi}{T}\cos\left(\frac{2\pi}{T}t + \varphi\right)\hat{\xi} \\
\ddot{\vartheta}(t) &= -A\frac{4\pi^2}{T^2}\sin\left(\frac{2\pi}{T}t + \varphi\right)\hat{\xi}
\end{aligned}
\tag{54}
$$

The active MRF source terms will be all the rotational ones, therefore in the formulation with relative velocity the active source terms are the Coriolis and the centrifugal force and the unsteadiness (rotational) term, whereas in the second formulation the Coriolis forces is present.

6.5. Combined oscillation

The combined oscillation case includes both the translational and the rotational oscillations superimposed, thus retaining their original kinematical relations. All the derived MRF source terms will be active.

Chapter III

Numerical Formulation

1. Introduction

The section describes the spatial and time discretization of Navier-Stokes equations. The spatial discretization is based on a finite volume, node centered approach operating on an hybrid unstructured grid. The artificial dissipation model is derived from the nonlinear scheme of Jameson [14], with no eigenvalue blending. Scalar or matrix dissipation can be chosen. The numerical scheme, used for the time discretization is a second order backward difference scheme and dual time stepping. A five stage Runge-Kutta scheme is used to drive toward zero the residual at each time step. With the use of residual averaging, a local CFL number of 4.9 could be employed in the multistage sub iteration process. The Algebraic Lagrangian Eulerian approach for generalized motion of the grid is included [8].

The Weiss and Smith version of low Mach number preconditioning is implemented in the code [6]. A sensor depending on cell Reynolds number was also introduced to avoid applying the preconditioning inside boundary layers.

Matrix dissipation was also found to be beneficial, allowing a strong reduction of the dissipation associated with convective eigenvalues, hence enabling a better resolution of vortices.

2. Space Discretization

2.1. Finite Volume Discretization

A finite volume discretization of equation (45) may be written according to

$$\frac{d}{dt}\left(\Omega_i X_i\right) + \Phi_i\left(\vec{X}, \vec{x}, \vec{v}_b\right) = Q_{X_i}\left(\vec{X}, \vec{x}, \vec{v}_b\right) \tag{55}$$

where

$$\Phi_i\left(\vec{X}, \vec{x}, \vec{v}_b\right) = \sum_{j \in K_i} \Phi_{ij}\left(\vec{X}, \vec{x}, \vec{v}_b\right) \tag{56}$$

$$Q_{X_i}\left(\vec{X}, \vec{x}, \vec{v}_b\right) = \sum_{j \in K_i} Q_{X_{ij}}\left(\vec{X}, \vec{x}, \vec{v}_b\right) \tag{57}$$

and

$$\Phi_{ij}\left(\vec{X}, \vec{x}, \vec{v}_b\right) = \left(\vec{F}_{I_{ij}}(\vec{X}, \vec{v}_b) - \vec{F}_{V_{ij}}(\vec{X})\right) \cdot \vec{\eta}_{ij} \tag{58}$$

In these expressions $\vec{x}_i$ indicates the position vector of node i, ε_i the set of the elements belonging to the patch P_i of elements surrounding a given internal node I and K_i the set formed by the nodes on the boundary of P_i. $\vec{F}_{I_{ij}}$, $\vec{F}_{V_{ij}}$ and $\vec{\eta}_{ij}$ represent a discretization of the convective ALE fluxes, viscous fluxes and the integrated finite volume normal related to the node-pair ij, respectively.

Integrating equation (55) between t^n and t^{n+1} leads to

$$\int_{t^n}^{t^{n+1}} \frac{d}{dt}\left(\Omega_i X_i\right) dt + \int_{t^n}^{t^{n+1}} \Phi_i\left(\vec{X}, \vec{x}, \vec{v}_b\right) dt = \int_{t^n}^{t^{n+1}} Q_{X_i}\left(\vec{X}, \vec{x}, \vec{v}_b\right) dt \tag{59}$$

3. Time Integration and Dual Time Step Approach

A second-order time accurate implicit algorithm that is popular in CFD is the second-order backward difference scheme. A generalization of this algorithm for dynamic meshes may be written as

$$\alpha^{n+1}\Omega_i^{n+1}X_i^{n+1} + \alpha^n\Omega_i^n X_i^n + \alpha^{n-1}\Omega_i^{n-1}X_i^{n-1} + \Delta t^n\Phi_i\left(X^{n+1},\vec{r},\vec{v_b}\right) - \Delta t^n Q_{X_i}\left(X^{n+1},\vec{r},\vec{v_b}\right) = 0 \qquad (60)$$

where

$$\Omega_i^n = \Omega_i(\vec{r}^n), \qquad \vec{r}^n = \vec{r}(t^n), \qquad \Delta t^{n+1} = t^{n+1} - t^n \qquad (61)$$

$$\alpha^{n+1} = \frac{1+2\beta}{1+\beta}, \qquad \alpha^n = -(1+\beta), \qquad \alpha^{n-1} = \frac{\beta^2}{1+\beta}, \qquad \beta = \frac{\Delta t^n}{\Delta t^{n-1}} \qquad (62)$$

and $\vec{r}$, $\vec{v}_b$ denote some linear combination of the mesh configurations and their velocities, i.e.

$$\vec{r} = \vec{r}\left(\vec{r}^{n-1},\vec{r}^n,\vec{r}^{n+1}\right), \qquad\qquad \vec{v_b} = \vec{v_b}\left(\vec{v_b}^{n-1},\vec{v_b}^n,\vec{v_b}^{n+1}\right) \qquad (63)$$

In the present work, the following choice has been made for $\vec{r}$, $\vec{v}_b$, denoted by $\tilde{r}$ and $\tilde{v}_b$, respectively

$$\tilde{r} = \frac{\vec{r}^{n+1} + \vec{r}^n}{2}, \qquad\qquad \widetilde{v_b} = \frac{\vec{r}^{n+1} - \vec{r}^n}{\Delta t^n} \qquad (64)$$

The basic idea of the dual time-stepping approach is to treat the equation (60) as a steady state problem and to solve it as an artificial unsteady equation:

$$\frac{\partial \vec{X}}{\partial t^*} + R^*(\vec{X}) = 0 \tag{65}$$

where

$$R^* = \frac{1}{\Delta t^n} \left(\alpha^{n+1} \Omega_i^{n+1} X_i^{n+1} + \alpha^n \Omega_i^n X_i^n + \alpha^{n-1} \Omega_i^{n-1} X_i^{n-1} + \Phi_i\left(X_i^{n+1}, \vec{r}, \overrightarrow{v_b}\right) - Q_{X_i}(X^{n+1}, \vec{r}, \overrightarrow{v_b}) \right) \tag{66}$$

Since the artificial time t^* is used as a relaxation parameter to find the steady solution of problem (65), variable local time steps Δt^* and residual averaging techniques are allowed. The pseudo-steady

Equation (65) is solved by using an explicit multistage algorithm originally developed for steady state applications.

4. Enforcement of Compatibility Conditions

The numerical source error due to the non inertial reference frame, can be examined analytically by imposing the conservation of the freestream. In this case all the flow derivatives are zero and the velocity vector is:

$$\vec{V} = \overrightarrow{V_\infty} + (\vec{\omega} \times \vec{r}) \tag{67}$$

where $\overrightarrow{V_\infty}$ is equal to:

$$\overrightarrow{V_\infty} = \begin{pmatrix} u_\infty \\ v_\infty \\ w_\infty \end{pmatrix} \tag{68}$$

The continuity, momentum, and energy equations (Eq. (24)) can then be reduced to the following expressions:

$$\rho[\vec{\omega} \cdot (\nabla \times \vec{r})] = 0 \tag{69}$$

$$\rho \vec{V}[\vec{\omega} \cdot (\nabla \times \vec{r})] + \rho \overrightarrow{V_\infty} \cdot \nabla \vec{V} = -\rho(\vec{\omega} \times \vec{V}) \qquad (70)$$

$$\rho E[\vec{\omega} \cdot (\nabla \times \vec{r})] = 0 \qquad (71)$$

For the first application case, where we have a steady rotation parallel to the y-direction, equations (69)-(71) can be reduced to the following expression:

$$0 = \omega_y \left(\frac{\partial z}{\partial x} - \frac{\partial x}{\partial z} \right) \qquad (72)$$

that is identically zero for any non-zero angular velocity ω_y. Whereas, for the second case, with a rotation parallel to x-direction , the Eq. 72 becomes:

$$0 = \omega_x \left(-\frac{\partial z}{\partial y} + \frac{\partial y}{\partial z} \right) \qquad (73)$$

In both cases, for the numerical formulation the right-hand side is not exactly zero, however, producing a freestream error.

Using the results of Eq. (72) and Eq. (73), and denoting the right-hand side as S_Ω, a simple and straightforward source term correction can be applied in Eq. (11). In particular, an additional source term $\vec{K}$ can be included to exactly cancel the freestream error:

$$\frac{\partial \vec{X}}{\partial t} + \nabla \vec{F}_I + \nabla \vec{F}_V = \overrightarrow{Q_X} + \vec{K} \qquad (74)$$

where $\vec{K}$ for a rotation around the y-axis is:

$$\vec{K} = S_{\Omega} \begin{bmatrix} \rho \\ 0 \\ \rho V_2 \\ 0 \\ \rho E \end{bmatrix} \tag{75}$$

whereas for the propeller the Eq. (75) becames:

$$\vec{K} = S_{\Omega} \begin{bmatrix} \rho \\ \rho V_1 \\ 0 \\ 0 \\ \rho E \end{bmatrix} \tag{76}$$

5. RANS Turbulence Model

The k-ω turbulence model proposed by Hellsten [2] has been employed. The model constants have been calibrated requiring consistent behaviour near boundaries between turbulent and laminar flow, inside shear flows and for zero pressure gradient wall flows. In particular, the calibration has been considered taking into account a variable c_{μ}, as it is the case if an algebraic stress model (EARSM) is included.

The Wallin-Johansson Explicit Algebraic Stress Mode (WJ-EARSM) [15] is implemented using Hellsten's k-ω as the basis RANS model. The model is an exact solution of the corresponding ARSM in two-dimensional mean flow. In three dimensions there is still a complete, while approximate, solution.

The full anisotropic version of the model is used, i.e. the anisotropic part of the Reynolds stress tensor is directly introduced in the momentum equations, while the isotropic part is taken into account in the form of an effective variable c_{μ}.

39

6. Boundary Conditions

The boundary conditions along solid walls for Navier-Stokes (viscous) flows are different from those for Euler flows. In the case of viscous flows, the velocity of the flow must vanish at the walls, while in the case of Euler flows, it is only required that the flow does not go through the wall.

As a consequence of the foregoing statement, at the airfoil the condition of non-penetration has been imposed, whereas on the blade surface, no-slip and no-penetration conditions are used by setting the absolute velocity equal to the absolute local blade velocity and the adiabatic wall condition and zero-normal pressure gradient condition at the wall are imposed at the blade surface.

In general, the boundary conditions applied at the far-field boundary are the same for Navier-Stokes and Euler flows, therefore the farfield boundaries are treated by using characteristic boundary conditions.

7. Mixing inertial/non-inertial reference frames in a multi-block system

Complex engineering simulations involving both fixed and moving parts of a vehicle or a machinery, such as the simulation of the effect of the rotation of a propeller on the aerodynamics of an aircraft or on the hydrodynamics of a ship are usually carried out defining several grid blocks in relative movement. The most used techniques in the literature are

- the unsteady Chimera technique

- the sliding grids approach

Both methodologies involve the creation of very complex data structures requiring the development and use of dedicated, specialized CFD codes. In addition, an efficient implementation in a multi-processor environment is hard to be attained due to the difficulty in achieving a satisfactory load balance between processors.

In case we are interested in the quasi-steady effect of the moving parts on the aerodynamic of the configuration (regardless, for example, acoustic effects or unsteady aero-structural coupling) we can consider the aerodynamic field as frozen in correspondence to a single phase angle of the periodic movement. In this case a simpler and faster approach can be followed, solving the Euler/Navier-Stokes equations in a mixed frame of reference. In practice, two or more mesh blocks are defined in which inertial or accelerated reference frames are respectively prescribed.

A simple data structure are then created in order to ensure the correct conservation of fluxes on both sides of the boundary between different RF.

The algorithm can be roughly described as follows:

- the coordinates of the grid points corresponding to the "non-inertial" blocks are read

- the grid elements residing across the block boundaries are found and flagged, say in blue

- for each "blue" element, the points residing in the "inertial" side are also red flagged.

- a set of "ghost" points is defined, corresponding two-way with the set of "red" points.

At each iteration of the solver:

- the Coriolis source term is computed for all points internal to non-inertial blocks and for "ghost" points, set to zero elsewhere

- the fluxes on all but "blue" elements are computed

- the fluxes on "blue" elements are computed, taking the source term of "ghost" points

It is worth noting that in the absolute velocity formulation there is no need to make any variable conversion at the block interfaces, resulting in a simpler and faster procedure.
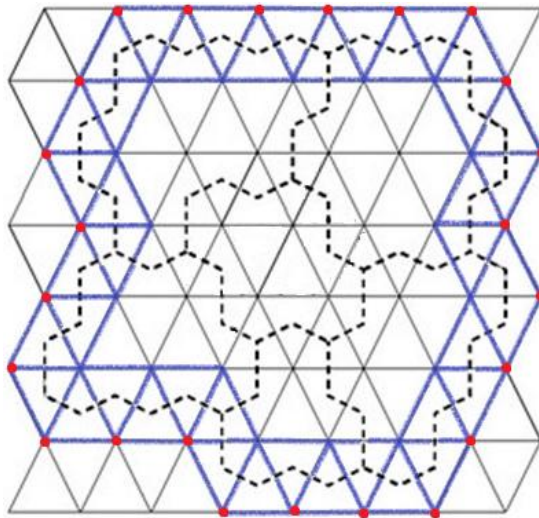
Figure 1: Data structure for mixing inertial/non-inertial reference frames in a multi-block system

Chapter IV

Numerical Results

1. Model validation: steady rotary NACA 0012 airfoil

To validate the numerical model, the stability derivatives for a NACA 0012 were computed using finite differences and compared with the results obtained by Limache and Cliff [9]. In the experiment, an airfoil is submitted to a steady rotation performed at constant incidence α for a given pitch rate q, generating a steady flowfield in a reference frame attached to the airfoil. The radius of the loop is inversely proportional to q. Thus, as q reduces to zero, the radius approaches infinity and steady level flight is recovered.

The results presented below are all computed for an angle of attack equal to zero, so we use the wind-axis reference frame for the computation of the derivatives.

1.1. Aerodynamically Motion

In this Section it will be proved that the aerodynamically steady motions are well-defined and physically meaningful.

Consider the vector $\vec{v}_c$ that describes the velocity of a specified point of the airfoil with respect to a fixed observer in the inertial reference frame where the undisturbed air is assumed to be at rest. Note that the quantities $\vec{v}_c$, α, β are scalars so that their rates of change

are independent of the reference frame. For vector quantities the rates of change in two reference frames are related by the standard Eulerian formula

$$\frac{d\vec{v}_c}{dt} = \frac{d'\vec{v}_c}{d't} + \vec{\omega} \times \vec{v}_c \tag{77}$$

where $\vec{\omega}$ is the angular velocity of non-inertial reference frame respect to the inertial frame.

For an aerodynamically steady motion the speed of the airfoil $\vec{v}_c$ and the aerodynamic angles α, β must remain constant. Then, it follows that:

- the orientation of any body-frame is fixed with respect to the wind-frame, i.e. the body-frame and the wind-frame have the same angular velocity with respect to the inertial frame. Furthermore, in an aerodynamically steady motion, the components of the angular velocity are constant and this implies that:

$$\frac{d'\vec{\omega}}{dt} = 0 \tag{78}$$

- the velocity of the body-frame with respect to the inertial frame is a fixed vector in the body-frame, so:

$$\frac{d'\vec{v}_c}{d't} = 0 \tag{79}$$

This property combined with the Equation (77) leads to

$$\frac{d\vec{v}_c}{dt} = \vec{\omega} \times \vec{v}_c \tag{80}$$

Equation (80) defines a system of linear, constant-coefficient, ordinary differential equations for the components of $\vec{v}_c$ in the inertial frame. The system (80) can be integrated to yield

$$\begin{bmatrix} u_c(t) \\ v_c(t) \\ w_c(t) \end{bmatrix} = \left(\vec{v}_{c0} \cdot \frac{\vec{\omega}}{\omega} \right)\left(\frac{\vec{\omega}}{\omega} \right) t + \left[\vec{v}_{c0} - \left(\vec{v}_{c0} \cdot \frac{\vec{\omega}}{\omega} \right)\frac{\vec{\omega}}{\omega} \right] cos(\omega t) + \left(\frac{\vec{\omega}}{\omega} \times \vec{v}_{c0} \right) sin(\omega t) \quad (81)$$

A second integration gives the inertial-frame position components as

$$\begin{bmatrix} x_c(t) \\ y_c(t) \\ z_c(t) \end{bmatrix} = \begin{bmatrix} x_{c0}(t) \\ y_{c0}(t) \\ z_{c0}(t) \end{bmatrix} + \left(\vec{v}_{c0} \cdot \frac{\vec{\omega}}{\omega} \right)\left(\frac{\vec{\omega}}{\omega} \right) t + \left[\vec{v}_{c0} - \left(\vec{v}_{c0} \cdot \frac{\vec{\omega}}{\omega} \right)\frac{\vec{\omega}}{\omega} \right] \frac{sin(\omega t)}{\omega} - \left(\frac{\vec{\omega}}{\omega} \times \vec{v}_{c0} \right) \frac{cos(\omega t)}{\omega} \quad (82)$$

Equations (81)-(82) are a parametric description of a spiral. Note that Equation (81) includes a constant component along the direction $\vec{e}_\omega \equiv \vec{\omega}/\omega$ and a harmonic part. The constant vector multiplying $cos(\omega t)$ in Equation (81) is the orthogonal complement of the constant part, while the constant vector multiplying $sin(\omega t)$ is orthogonal to the plane spanned by $\{\vec{v}_{c0}, \vec{e}_\omega\}$. The magnitude of the vectors in the harmonic part are, in fact, equal. Such spiral motions are the most general class of motions of an aircraft for which an aerodynamically steady description is possible. For a related discussion see the book by von Mises [23].

1.2. Particular Cases

Let's restrict the general steady-motion to the case where $\vec{\omega}$ and $\vec{v}_0$ are orthogonal. In this case Equations (81) and (82) reduce to

$$\begin{bmatrix} u_c(t) \\ v_c(t) \\ w_c(t) \end{bmatrix} = \vec{v}_{c0} cos(\omega t) + \left(\frac{\vec{\omega}}{\omega} \times \vec{v}_{c0} \right) sin(\omega t) \quad (83)$$

$$\begin{bmatrix} x_c(t) \\ y_c(t) \\ z_c(t) \end{bmatrix} = \frac{\vec{v}_{c0}}{\omega} sin(\omega t) - \left(\frac{\vec{\omega}}{\omega} \times \frac{\vec{v}_{c0}}{\omega} \right) cos(\omega t) \quad (84)$$

Moreover, in equation (84) the constant vector multiplying *sin(ωt)* has the same magnitude as that multiplying *cos(ωt)* and is orthogonal to it. Than, it follows that, the motion is planar, and that in fact it is a circular path.

This result can be seen more clearly if, the coordinate system is chosen in such a way that $\vec{\omega}$ points in the y-axis and $\vec{v}_{c0}$ in the direction of the x-axis. Then, equations (83) and (84) simplify to:

$$\begin{bmatrix} u_c(t) \\ v_c(t) \\ w_c(t) \end{bmatrix} = \begin{bmatrix} v_{c0}\cos(qt) \\ 0 \\ -v_{c0}\sin(qt) \end{bmatrix} \tag{85}$$

$$\begin{bmatrix} x_c(t) \\ y_c(t) \\ z_c(t) \end{bmatrix} = \begin{bmatrix} \dfrac{v_{c0}}{q}\sin(qt) \\ 0 \\ \dfrac{v_{c0}}{q}\cos(qt) \end{bmatrix} \tag{86}$$

It is obvious from the above expression that the motion is a circular motion in the plane (x, z). This circular motion is exactly a circular aerodynamically steady motion. Note in particular that the radius of the circular path satisfies the relationship:

$$R_c = \frac{v_{c0}}{q} \tag{87}$$

Finally note that in the limit where $\vec{\omega} \rightarrow 0$ the general motion reduces to the condition

$$\vec{v_c} = \vec{v_{c0}} \tag{88}$$

which is the well-known uniform, rectilinear, steady motion.

1.3. Airfoil in Planar Steady Motion

Consider an airfoil moving in a rectilinear motion through the air at constant speed V_∞ and at constant angle of attack α. Following the usual convention and as shown in Fig. 2, the body-fixed coordinate system is chosen such that the z-axis points in the direction of the span and the x, y axes form the plane of the airfoil. The x-axis is chosen to be along the chord of the airfoil.
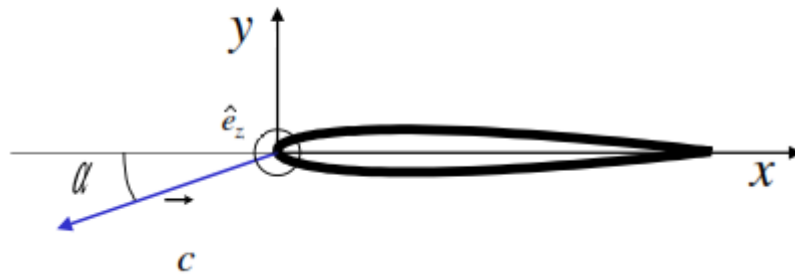
Figure 2: Body- fixed coordinate system

Since the problem is two-dimensional the only aerodynamic forces and moments that have to be considered are the lift , the drag and the pitching moment. For the class of rectilinear motion defined above these three aerodynamics forces and their corresponding non-dimensional coefficients can be represented in terms of the steady function $\bar{F}$ as:

$$F = \bar{F}(V_\infty, \alpha) \tag{89}$$

Assuming the flow is inviscid, these aerodynamic forces can be determined by an appropriate integration of the static pressure along the airfoil's surface. By running the CFD code at different Mach numbers and angles of attack the three set of functions can be constructed:

$$C_l = \bar{C}_l(M, \alpha) \tag{90}$$

$$C_d = \overline{C_d}(M, \alpha) \tag{91}$$

$$C_m = \overline{C_m}(M, \alpha) \tag{92}$$

In a general planar motion, the three functions that describe the airfoil motion are $\bar{V}(t)$, $\bar{\alpha}(t)$ and the pitch-rate $\bar{q}(t)$. The dependence of the aerodynamic forces on the pitch rate can not be obtained from the equation (89). This dependence can only be determined by calculating the aerodynamic forces acting on a general class of aerodynamically steady motions: circular motions as the one shown in Fig. 3. For the present case of the airfoil problem, the choice of the body-fixed coordinate system, defined above, implies that the angular velocity vector can be written as

$$\vec{\omega} = q\tilde{e}_z \tag{93}$$

where q defines the pitch-rate. In Fig. 3 it can also be observed how the coordinate system moves with respect to the inertial reference frame. It is clear that the system of reference in non-inertial.
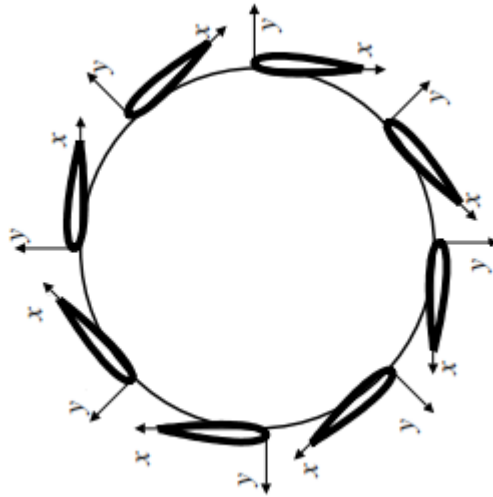
Figure 3: Steady circular motion for an airfoil

For the numerical determination of the aerodynamic forces along these planar aerodynamically steady motions, the flow equations derived in Section 2 must be used. It is necessary:

48

- setting $w = 0$

- zeroing any dependence with respect to z

- setting $p = q = 0$ and using q instead of r

We note the following about the code UNS3D:

- we do not need time-accurate solutions since we are looking for the steady state solution;

- for the case of generalized aerodynamically steady motions, the residual contain additional terms due to the presence of the source term;

- the additional term Q may change some stability properties [19], and this is the case indeed. For stability purposes the Jacobian must contain terms involving the Jacobian of the source term. It must be pointed out that we did not get the convergence when these terms were neglected;

- following Tobak and Schiff we will define the non-dimensional pitch rate as:

$$\hat{q} = \frac{qc}{V} \tag{94}$$

Other authors (such as Etkin) define the non-dimensional pitch-rate as $\hat{q} = qc/2V$

- the non-dimensional pitch rate is related to the radius of the circular trajectory through

$$\hat{q} = \frac{c}{R_c} \tag{95}$$

- The numerical scheme will allow us to evaluate the aerodynamic forces and moments and its non-dimensional coefficients. As a consequence, equations (90)-(92) can be generalized to include the dependence on the pitch-rate q:

$$C_l = \overline{C_l}(M, \alpha, \hat{q}) \tag{96}$$

$$C_d = \overline{C_d}(M, \alpha, \hat{q}) \tag{97}$$

$$C_m = \overline{C_m}(M, \alpha, \hat{q}) \tag{98}$$

1.4. Numerical results

In Fig. 4 is shown the 2D unstructured grid. The outer boundary is at a distance 30 times the length of the airfoil's chord with respect to the grid center, coincident with the leading edge of the airfoil. The grid is made by 12334 nodes and 12096 elements.
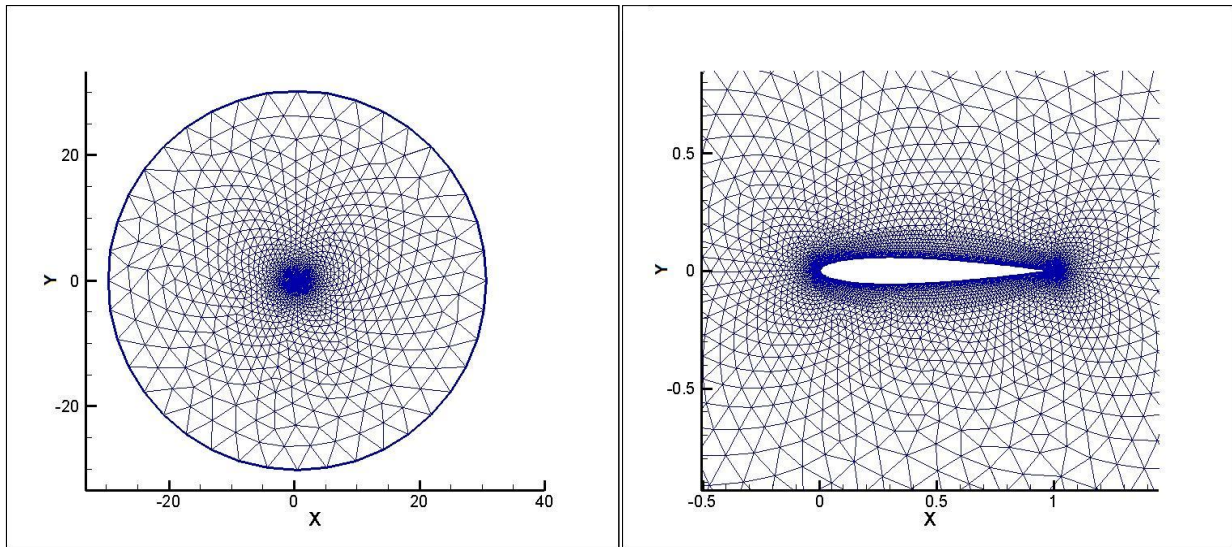
Figure 4: Mesh: a) wide- view, b) close- view

To verify the implementation of 3D Navier-Stokes equations in terms of absolute velocities, we compare results for the NACA0012 airfoil rotating at a finite q to those produced by Limache [10] simulating inviscid flow around a NACA 0012 airfoil at Mach equal to 0.2 for non-dimensional pitch rate q̂ equal to 0, 0.01, 0.03, and 0.05. In facts, at the present test conditions (low Mach number, low incidence) we do not expect that the integral quantities computed using viscous and inviscid methods, respectively, differ significantly.
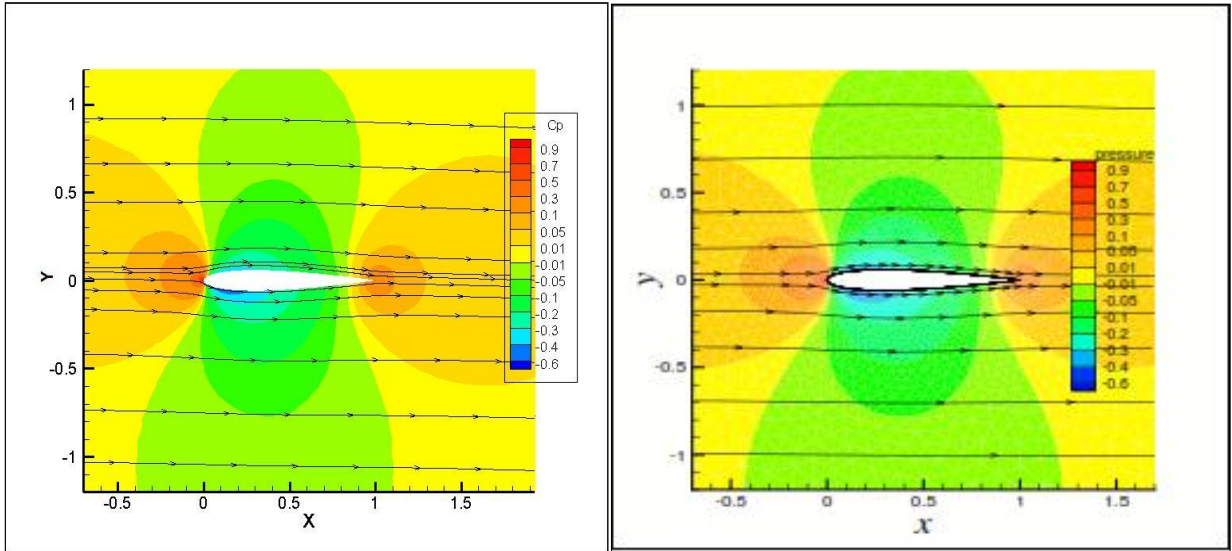
Figure 5: C$_p$ contours and streamlines comparison for rotating NACA 0012 airfoil at Mach = 0.2 and α = 0°: a) present work, $\hat{q} = 0.01$, b) Limache [10], $\hat{q} = 0.01$

The C_p distributions around the airfoil are shown in Fig. 5 where the computed C_p distributions and streamlines of relative velocity are compared with those presented in [10] for $\hat{q} = 0.01$. In Fig. 6 the pressure coefficient contours and streamlines of relative velocity in the whole computational domain are shown.
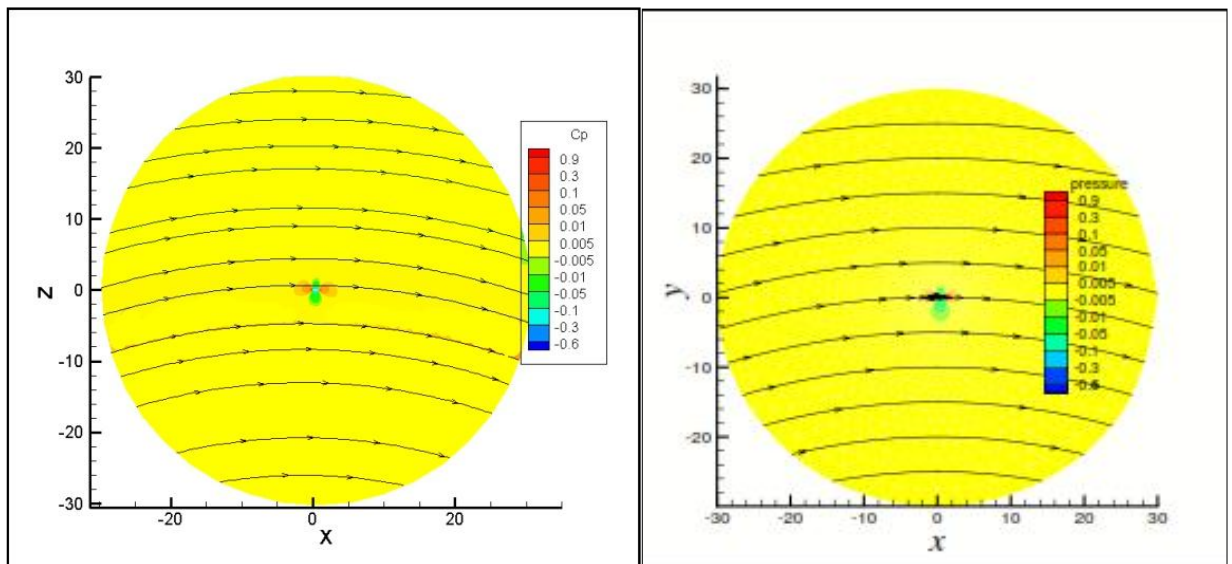
Figure 6: C$_p$ contours and streamlines comparison for rotating NACA 0012 airfoil at Mach = 0.2 and α = 0°: a) present work, $\hat{q} = 0.01$, b) Limache [10], $\hat{q} = 0.01$

51

As we mentioned, these flow solutions correspond to cases where the airfoil is flying in circular trajectories as in Fig. 3.

Fig. 5-6 show the pressure coefficient contours and the velocity streamlines for the case where the airfoil has a non-dimensional pitch-rate of $\hat{q} = 0.001$. According to equation (95) this value corresponds to a circular trajectory of radius R_c equal to 100 times the airfoil chord.

In Fig. 7 we see the flow solutions for the case where the pitch rate has been set to $\hat{q} = 0.003$. This value corresponds to a circular trajectory of radius R_c equal to 33 times the airfoil chord. In Fig. 8 we see the flow solutions for the case where the pitch rate has been increased to $\hat{q} = 0.005$. This value corresponds to a circular trajectory of radius R_c equal to 20 times the airfoil chord.

From the close-view of the Figures 5- 8 an interesting phenomenon can be seen: as the pitch rate increases nose-down the pressure in the upper surface of the airfoil tends to increase while in the lower surface tends to decrease. Then, it follows that an increasing negative lift is produced as q increases nose-down. This behavior is also clear from the Table 1 where the results corresponding to Limache and Cliff [9] are shown between parentheses. From these numerical simulations, it follows that C_ is a decreasing function of the (nose-down) pitch-rate q. Conversely, C_ is an increasing function of a (nose-up) pitch rate q. Similarly, from the results shown in Table 1, it follows that a restoring pitching moment (nose-up) is produced when the airfoil is pitching (nose-down). The magnitude of this restoring moment increases with the magnitude of the pitch rate.

If we look at the far-field behavior of the flow solutions, we see that the streamlines tend to be circular curves. This result is in complete agreement with the physics of the problem

since that is the behavior an observer in the body-fixed reference frame will see when the airfoil is flying in a steady circular trajectory. The result is also in agreement with the mathematics, since the flow defined in equation (86) corresponds to circular streamlines.

These results are in agreement with what is observed in reality and the two implementations match quite well over a range of $\hat{q}$ values.

Finally, observe that in all the solutions the center of the circular streamlines is located at a distance equal to the radius R_c. This phenomenon can be seen clearly for the case $\hat{q} = 0.005$ (corresponding to $R_c = 20c$) shown in Fig. 8. It is important to mention that this phenomenon appears naturally from the flow solution and has not been imposed explicitly.

The other condition that we can check at the far-field is if the pressure coefficient tends to zero as $\|\vec{x}\| \rightarrow \infty$.

This property seems to be true for all the $\hat{q}$ values and the cause of this phenomenon is the choice of the use of the absolute velocity for the formulation of the equations. In fact, the unperturbed velocity is longer uniform and the rotational component that increases proportionally to q and $\|\vec{x}\|$ as $\|\vec{x}\| \rightarrow \infty$ is deleted by the freestream error.

Table 1 Comparison of lift and moment coefficients for the NACA 0012 at $\alpha = 0°$ and Mach $= 0.2$ al various values of $\hat{q}$ (Results from Limache [10] are in parentheses)

$\hat{q}$	C_l	C_m
0.01	-0.051 (-0.053)	-0.02 (-0.018)
0.03	-0.153 (-0.157)	-0.06 (-0.053)
0.05	-0.26 (-0.262)	-0.1 (-0.088)
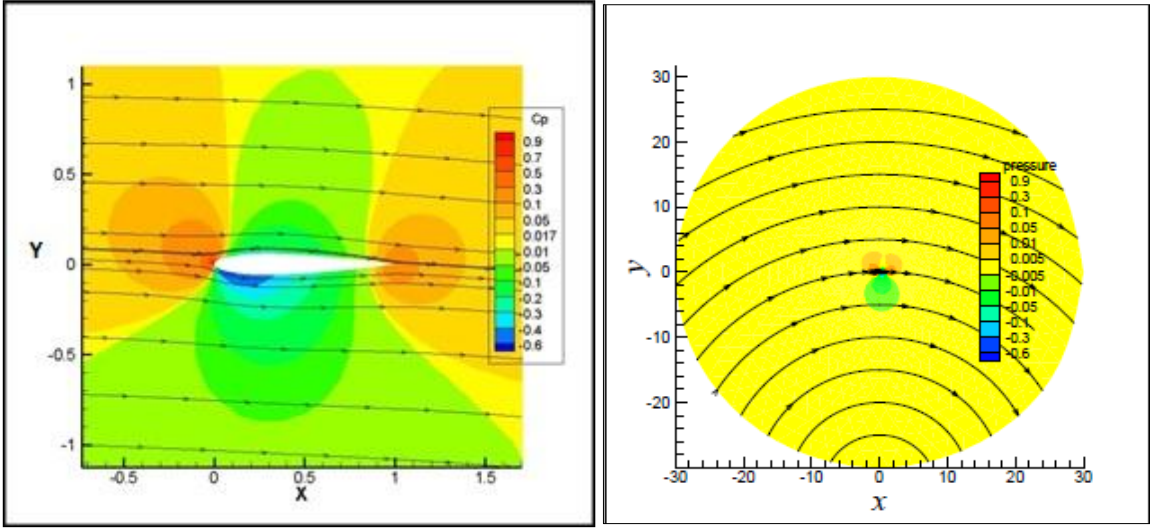
Figure 7: C_p contours and streamlines for rotating NACA 0012 airfoil at Mach $= 0.2$ and $\alpha = 0$, $\hat{q} = 0.03$
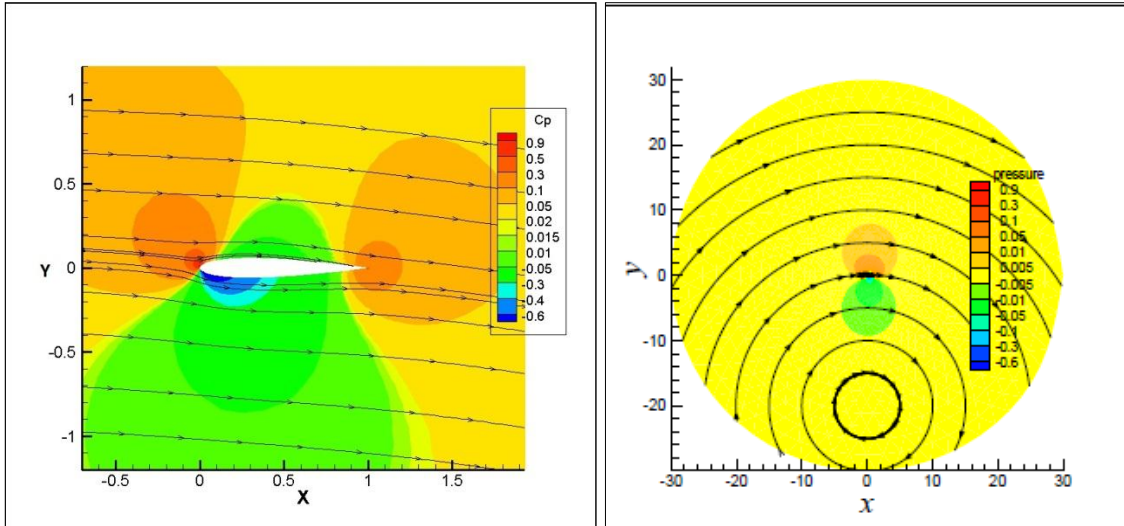
Figure 8: C_p contours and streamlines for rotating NACA 0012 airfoil at Mach = 0.2 and α = 0, $\hat{q} = 0.05$

The stability derivatives are calculated using finite differences:

$$C_{(\blacksquare)_q} \approx \frac{C_{(\blacksquare)}(M, \alpha, q + \Delta q) - C_{(\blacksquare)}(M, \alpha, q,)}{\Delta q}$$

In Table 2 the stability derivatives are compared with the results obtained by Limache.

Table 2 Comparison of stability derivatives for the NACA 0012 at α = 0° and Mach = 0.2

Derivatives	UNS3D	Limache and Cliff
C_{lq}	-5.225	-5.250
C_{mq}	-1.932	-1.766

It is possible concluding that the results obtained by UNS3D are in good agreement with the numerical results obtained by Limache and Cliff [9].

2. Propeller Application

2.1. Geometrical Model
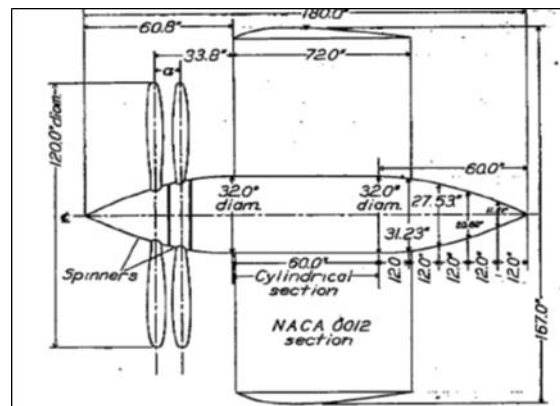
Figure 9: Geometrical and experimental model

In Fig. 9 it is possible to see the geometry of the experimental model used by D. Biermann and Eiiwin P. Haetman [5]. The experimental results were performed for four- and six-blade single-rotating and dual-rotating propellers with and without the symmetrical wing in place. The maximum propeller speed was 550 rpm. The results for four-blade single-rotating propeller were made up with two two-way hubs mounted in tandem and the spacing between front and rear blades are not equal and therefore the front blade led the rear by 85.4 deg. In

this session only the four-blade single-rotating propeller with and without wing are considered for the comparison with the experimental results in terms of thrust coefficient. The propeller, namely an Hamilton Standard 3155-6, consists of four blades installed on a single way hub in front of a streamline body, or nacelle, housing the engine needed to spin it. The four blades are streamlined using Clark Y profiles and the angle between two blades is 90 deg.

In the report of Biermann and Haetman [4] several blade pitch angles, defined as the angle between the rotation plane and the airfoil chord at 75% of the radius of the propeller, ranging from 20 deg to 65 deg. In our case it was decided to investigate a propeller with a blade pitch angle of 45 deg. The propeller diameter is 3.08 m. Starting from the geometrical details reported in the mentioned report, a mathematical model describing the propeller has been created with CATIA V5 (Fig. 10). The wing, shaped using NACA 0012 airfoils, is located in a mid position of the spinner and set at an angle of attack of 0 deg. Wing chord is 1828.8mm and wing span is 4241.8mm.
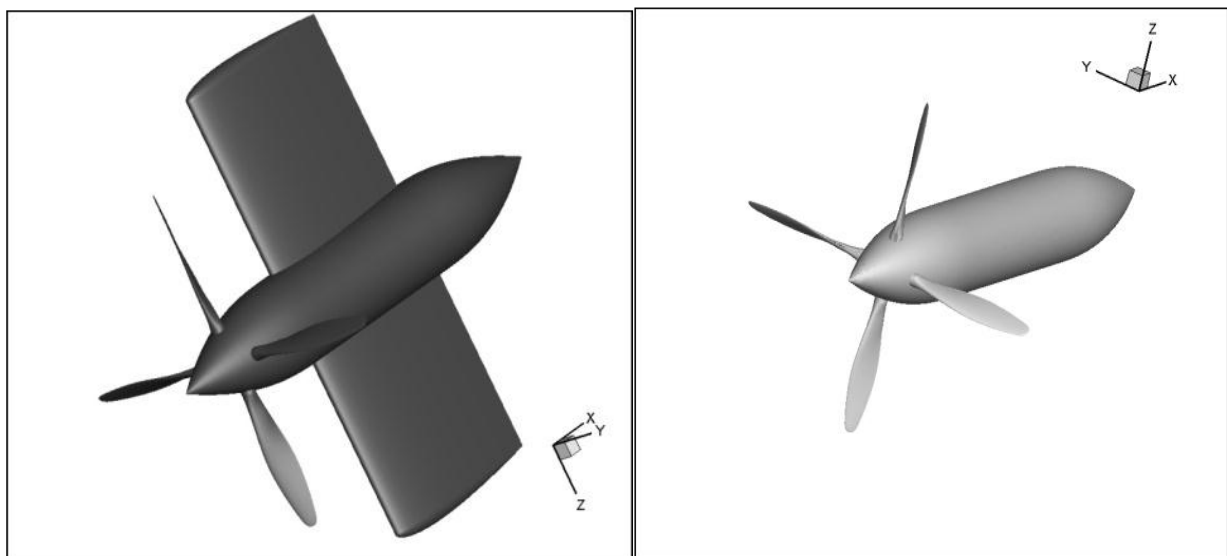
Figure 10: CATIA model: a) propeller with wing, b) propeller without wing

2.2. Results for the four-blade single-rotating propeller + spinner (viscous)

A 3D unstructured grid of the propeller + spinner has been generated with ICEM-CFD (Fig. 11). This grid is strongly refined in the region around the blades and on the blade surfaces. It is made by:

- 5672824 nodes

- 16265544 elements

- 21 prismatic layer on solid surfaces to correctly match boundary layer behavior
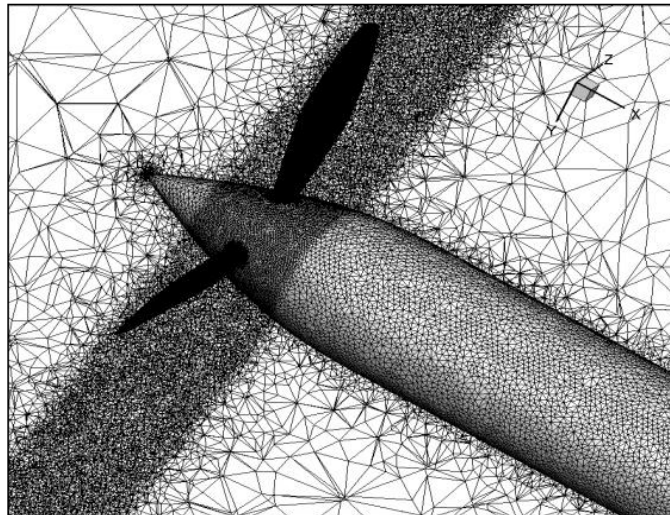

Figure 11: Grid generated with CFD-ICEM.

In the code UNS3D it is possible to specify an arbitrary velocity for a specific group of nodes within the mesh (ALE formulation). The resulting fluxes are automatically interfaced in order to ensure conservation at the boundary between rotating and non rotating zones. The solution is then computed specifying a rotational velocity, as described in Eq. (23), only for the nodes inside the rotating block (Fig. 12) and taking into account the source terms (Eq. (21)) and the correction terms as in Eq. (75)-(76).
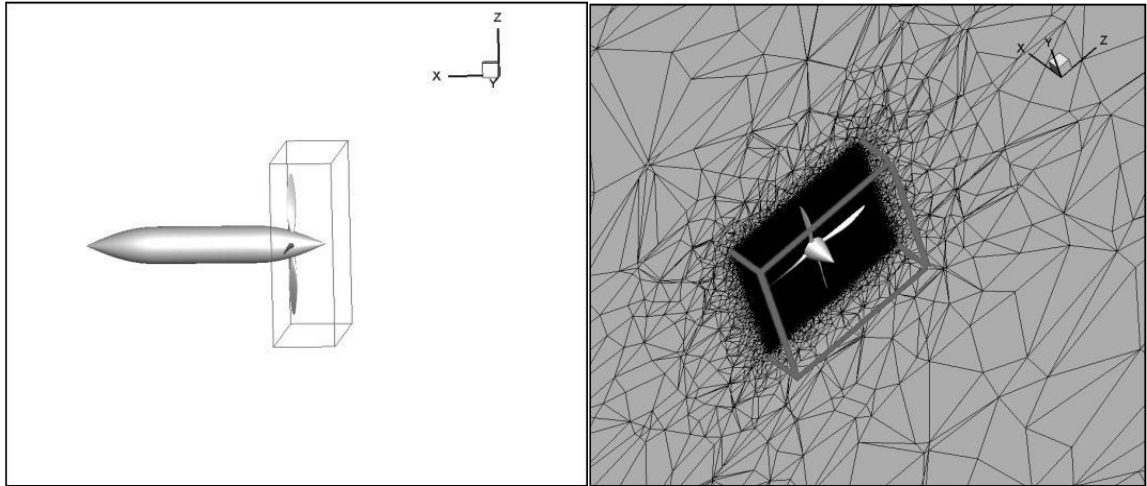
Figure 12: Rotating block within the mesh: a) propeller, b) mesh inside the block.

Five different operating conditions, shown in Table 3, were investigated. The axial undisturbed velocity has been set equal to 49.1744 m/s, corresponding to the maximum wind tunnel test speed of 110 mph [4].

Table 3 Operating conditions investigated

Advance Ratio	Velocity, m/s	Rotational speed, rps
1.43	49.1744	11.14
1.5	49.1744	10.6
1.8	49.1744	8.9
2.0	49.1744	8.0
2.4	49.1744	6.6

In Fig. 13 it is possible to note a general increasing level of the relative Mach number from the nacelle surface toward the tip, which is the result of the increasing rotational speed with increasing radius.
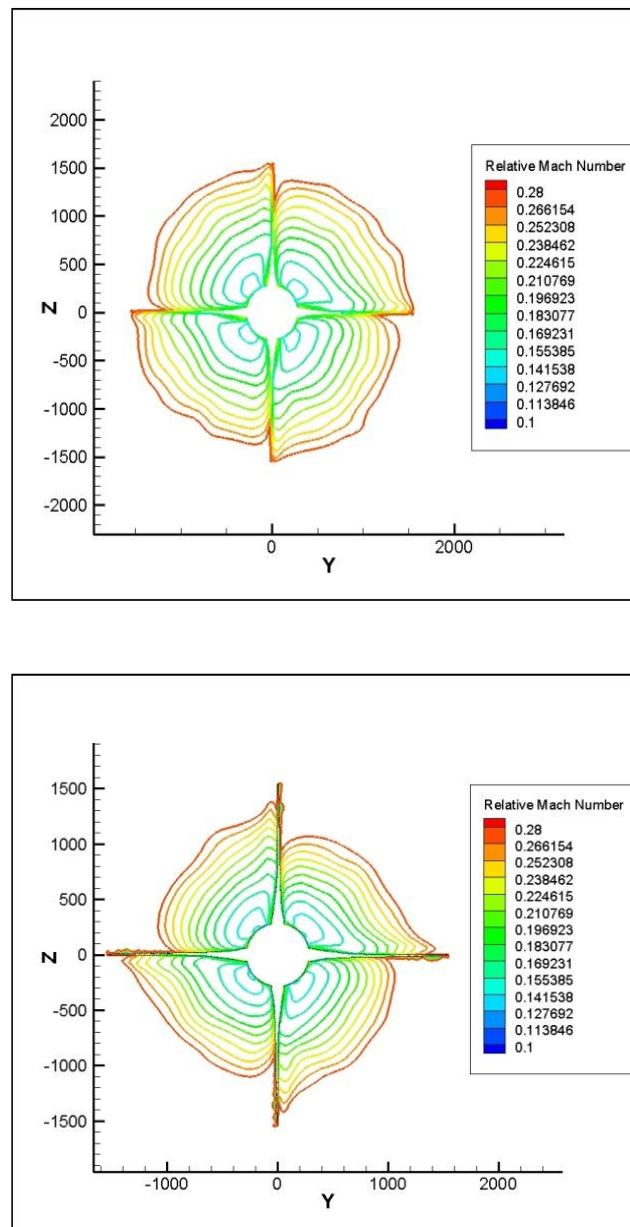
Figure 13: Relative Mach number contours in the plane (y,z): a) J=1.8, b) J=1.43

Both the pressure coefficient, Fig. 14, and Mach number distribution, Fig. 15, on the suction side of the blade indicate higher load on the forward portion of the blade. Near the

nacelle surface on the suction side, the high pressure and low Mach number regions are caused by the rapid increase in spinner diameter. On the pressure side of the blade, the high relative Mach numbers at about mid-chord, which is the location of maximum thickness on the blades, is apparently related to the thickness distribution of the airfoils used in the blade.
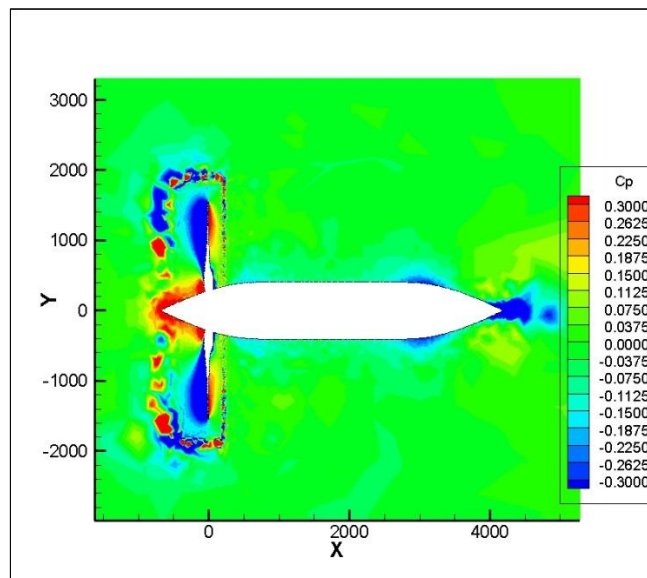

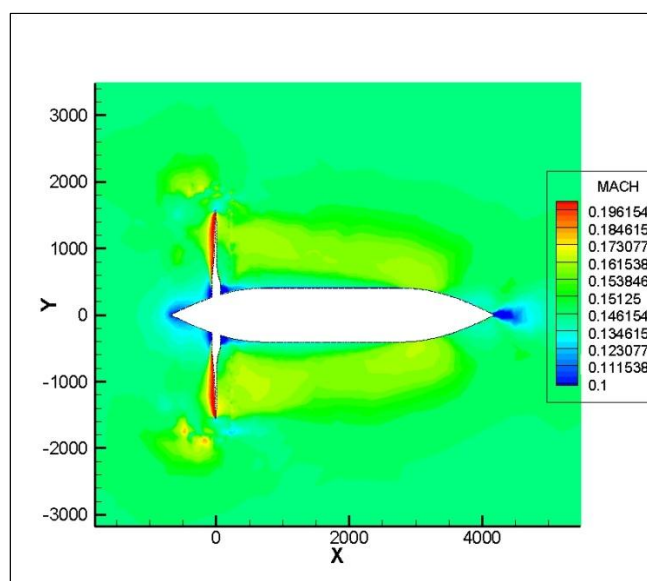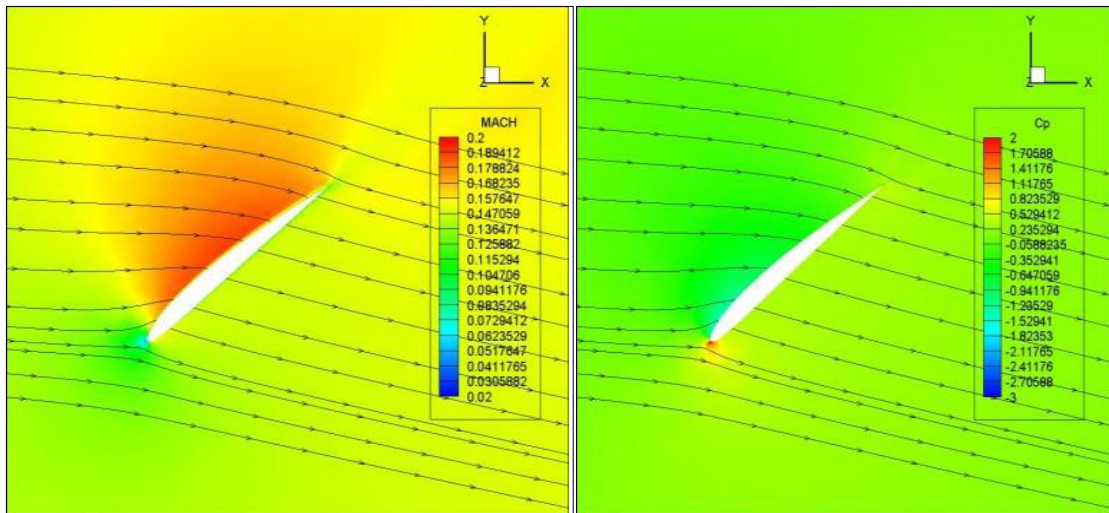**Figure 14: Pressure coefficient distribution around the propeller in the plane (x, y) for J=1.8**

Figure 15: Mach number distribution around the propeller in the plane (x, y) for J=1.8

The Mach number distribution on the blades generally follows the same trends as the pressure coefficient, as demonstrated in Fig. 16.

Figure 16: Mach number and pressure coefficient over a 65% section of a blade for J=1.8

Note, that the flow is accelerated as it passes through the propeller. As the flow accelerates, the region defined by the streamlines passing through the propeller region (slipstream) contracts. Patches of higher velocity flow correspond to passage of individual blades. The acceleration of fluid is related to the pressure gradient, which determines the thrust on the propeller. Part of the acceleration occurs upstream of the propeller as the pressure on upstream (suction) side of the blade is lower than the ambient pressure, and part of the acceleration occurs downstream as the pressure on downstream (pressure) side of the blade is higher than the ambient pressure. This is documented by the pressure coefficient contours in Fig. 17.

The flow around a blade is essentially 3D because of the presence of the spinner that induces radial displacement of the incoming fluid, but also because of the local pressure distributions along the radius.
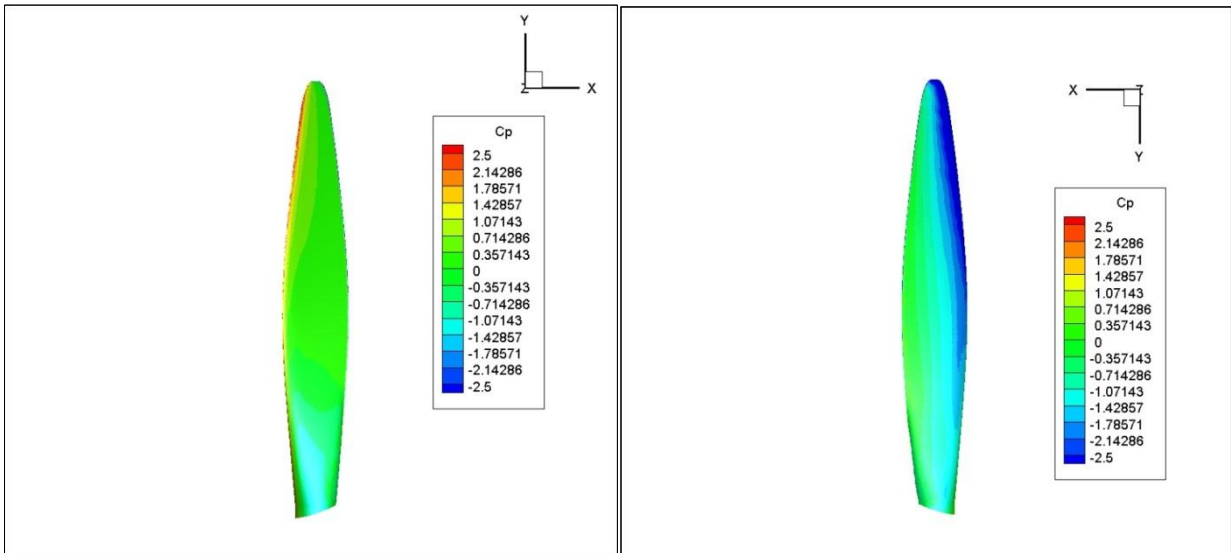

Figure 17: Pressure coefficient on the pressure and the suction side of a blade for J=1.8

In Fig. 18 it is possible to see as the particles pass around the propeller due to the rotational speed. It can be seen that the stream has a swirl velocity after it passed through the propeller. The direction of the swirl velocity is the same as the propeller blade rotation direction. It is also clearly that the slipstream contracts through the propeller. And the contraction of the slipstream at J=1.8 is smaller than that of J=1.43, so the degree of the contraction of the slipstream is determined by the advanced ratio.
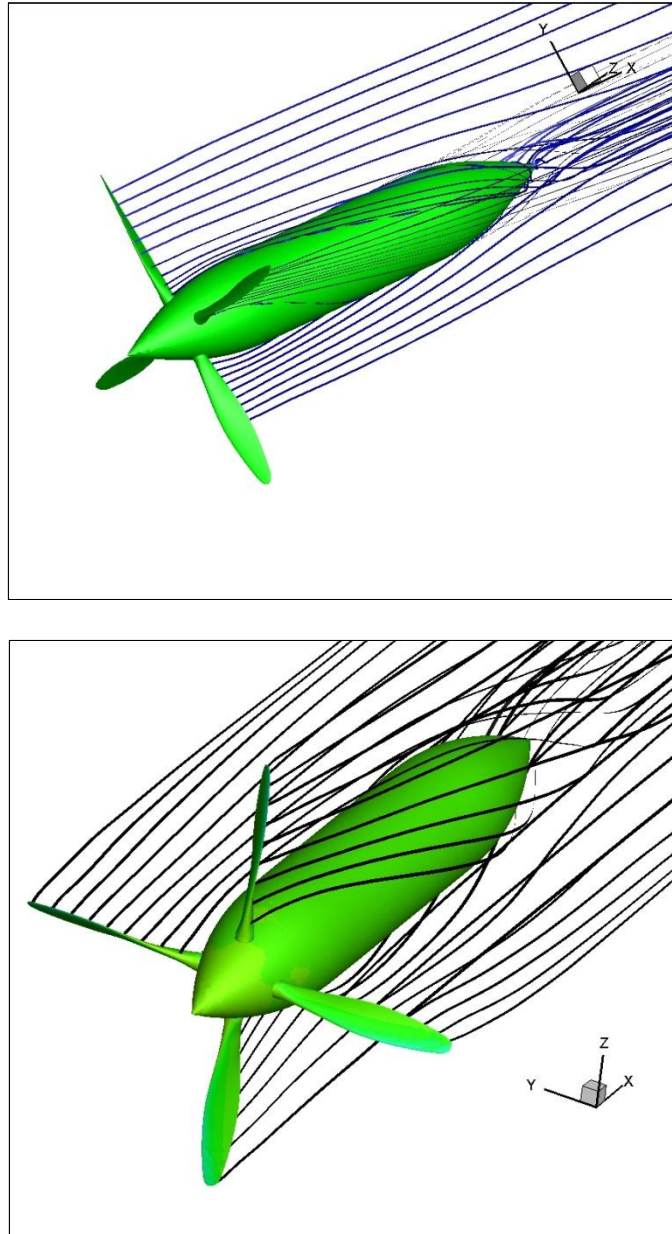
Figure 18: Slipstream around the propeller for J=1.8 and J=1.43

The flow field generated by the propeller is characterized, as expected, by the formation and convection of strong tip vortices.

Concerning vertical structures, there are essentially three regions of intense vorticity: the tip vortex, the horse-shoe vortex at the root and a sheet of trailing vorticity. These structures

are illustrated in Fig. 19. The tip vortex follows the helical path of the tip and has a strong intensity. Its core extension, measured to the point of maximum circumferential velocity, is typically of the order of 5% to 10% of the blade chord [20] and tends to increase with decreasing blade tip thickness [21]. The horse-shoe vortex in comparison has a much smaller spatial extent [22]. The wake of the blade contains a sheet of trailing vorticity that usually vanishes within one chord length.
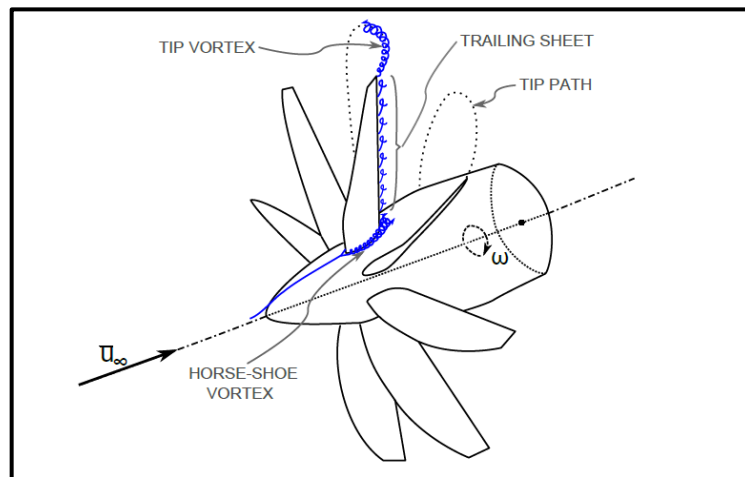
Figure 19: Main flow features around a propeller blade

These phenomena can be explained if we consider a bound vorticity on a lifting surface, which varies in magnitude along the span. In this situation a free vortex filament must emanate from the trailing edge with magnitude equal to the change of bound vorticity. The derivative of the strength of the free vortex sheet in the spanwise direction must be equal to the negative of the derivative of the strength of the bound vorticity in the spanwise direction. The vortex sheet may be thought of as drifting with the fluid. There can be no forces on it, no discontinuity of pressure, and no discontinuity of normal velocity, only a discontinuity of tangential velocity the magnitude of which is the vortex strength of the sheet.

Although the pressures on either side of the sheet are equal, suggesting that it may translate freely without deformation, there is a serious difficulty at the edge of the sheet where there is a singularity in the velocity field.

We suppose that, after an initial distortion, the vortex sheets shed from the trailing edges of the propeller blades form a set of interleaved helicoidal sheets which translate uniformly downstream parallel to the axis without further deformation as if they were rigid surfaces. The change in radial velocity across the sheet is the vortex strength of the sheet and everywhere has the magnitude required for it to be in equilibrium. The helicoidal vortex sheets are floating freely in an irrotational field with equal velocity on either side of the sheet, hence equal pressure. Since there is no pressure discontinuity across the sheets, it may be hypothesized that the sheets move axially backward without deformation. The system of helicoidal vortex sheets moving backward without deformation is a mathematical model which provides a means of connecting the induced velocity at the propeller with the propeller loading. Most importantly, under certain assumptions it has been shown to be the slipstream condition for maximum efficiency for a given required thrust. Consequently, it dictates the radial load distribution on the propeller blades for best efficiency. For these reasons, it is the essential framework for a propeller design system.

Vortex sheets are considered to be of vanishing thickness, simple surfaces of velocity discontinuity.

All of the fluid in the slipstream is contained between the vortex sheets and is therefore everywhere irrotational even as the distance between sheets becomes vanishingly small.

In a real fluid the sheets always have some thickness and in the limit the fluid must be filled with vorticity. The vortex sheet treatment is only valid where the distance between the

sheets is at least comparable with the thickness of the sheets. Passing from the case of the plane vortex sheet behind a wing to the case of the postulated helicoidal sheets behind a propeller, the outer parts of the sheets are absorbed into a set of helical vortices equal in number to the number of interleaved sheets and the inner parts are absorbed in a single vortex of opposite sense lying on the axis.

Freely moving helicoidal vortex sheets in the slipstream of a propeller would seem to be an unrealistic hypothesis in view of the necessity of an edge force with nothing on which to act.

However, they can and do exist in the modified model of helicoidal sheets which are more or less gradually absorbed into a set of helical vortices. Several arguments may be put forth to justify the helicoidal vortex sheets as adequate representations of the trailing vortex system for the purpose of relating the loading of the propeller to the velocities induced by the trailing vortices at the propeller blades. First consider the following two principles:

- In the evolution of a free vortex system in the absence of external forces acting on the fluid, hydrodynamic impulse is conserved.
- If in an unbounded fluid at rest at infinity there is a vortex system having a certain impulse, replacement of the vortex system by another of the same impulse may result in a very different distribution of velocity in the neighborhood of the vortex, but the velocity fields will be identical at large distances.

From these two principles it is inferred that the velocities induced at the propeller by downstream portions of the fully rolled-up helical vortex system are the same as would be induced by undeforming helicoidal vortex sheets. Immediately behind the propeller there are helicoidal vortex sheets. It is only the part of the vortex system in an intermediate region

where the sheets are rolling up that there may be some doubt of the accuracy of the helicoidal sheet model as contributor to the velocity induced at the propeller.

Consequently, it is justifiable to consider that the system of helicoidal vortex sheets translate backward without deformation. This is to be understood as a special case since for arbitrary radial distribution of circulation the axial induced velocity of the trailing vortices will not be uniform and the vortex sheets will have a continuously changing form. The vortex system of heavily loaded propellers may, in some circumstances, roll up in quite strange and unexpected ways.

In our case, as the propeller rotates, it induces swirls in the slipstream and the blade tip vortices pass by periodically. This phenomenon is more evident when the advance factor decreases. In fact for lower advance factors, we see a strong vortex shedding, which starts from each blade and travels downstream with the perturbation velocity creating strong spiral type regions in the rear wake for each blade (Fig. 21). Furthermore strong hub and tip vortices (Fig. 20) are continuously shed from the respective blade regions and 'absorb' the weaker vorticity regions at inner blade radii producing also spiral type patterns. A strong tip vortex with negative vorticity and nearby a red spot corresponding to a counter-rotating vortex. At the trailing edge of the blade, free vortices are shed the rotation of which is opposite to that of the leading-edge vortex (change in gradient sign of the circulation distribution curve). The trailing-edge vortex is originally connected to the trailing vortex sheet. When the leading-edge vortex leaves the blade trailing-edge, it interacts with the vortex sheet, which is thus warped and gives birth to a concentrated trailing-edge vortex. This one is embedded in the flow field of the dominant leading-edge vortex. The latter induces velocities at the trailing vortex which lead to an helical path of the trailing vortex around the leading-edge vortex.
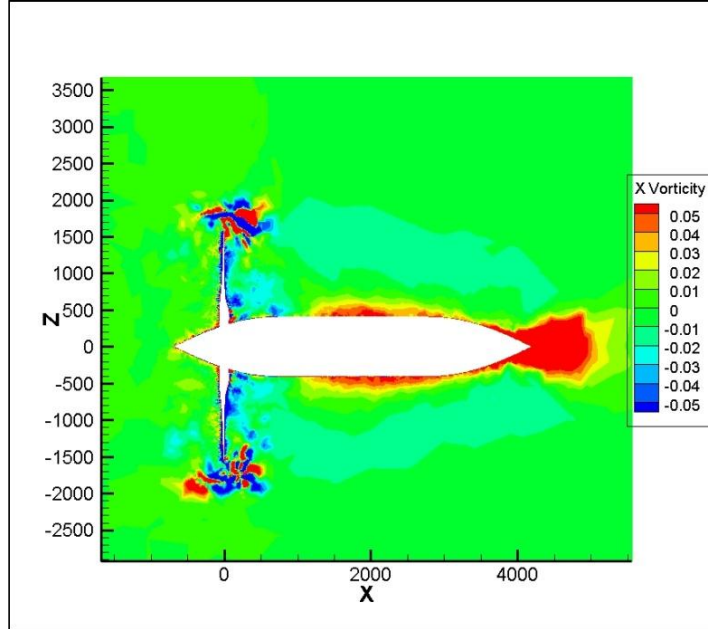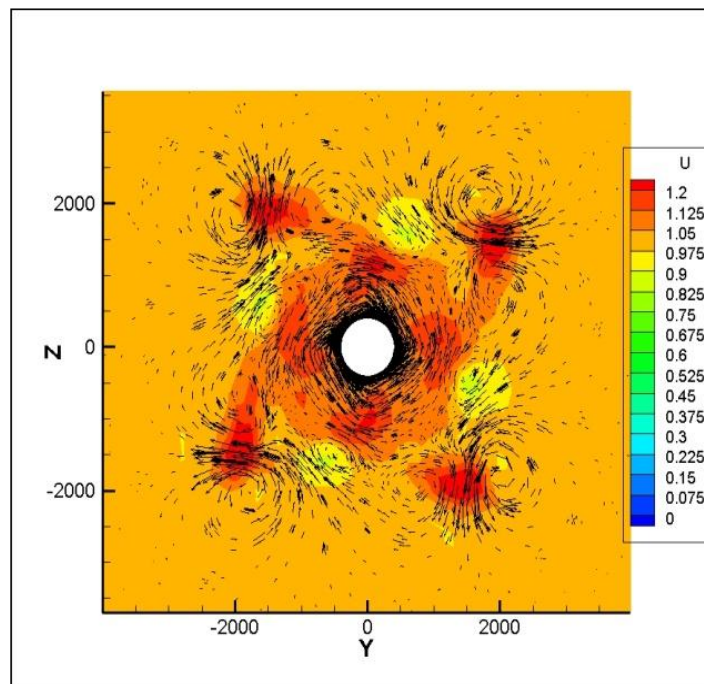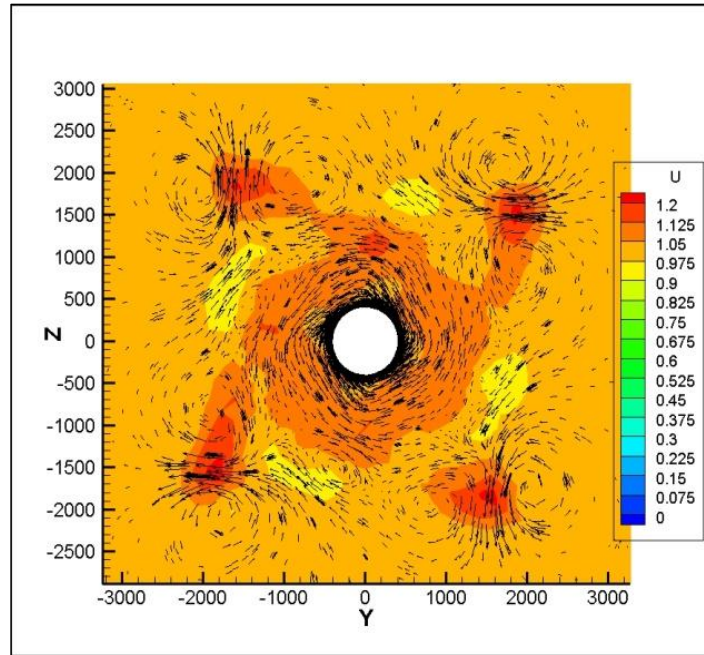
Figure 20: X-vorticity in the plane (x,z) for J=1.43.

Figure 21: X-velocity in the plane x = 750 mm: a) J=1.8, b) J=1.5.

The vortices can be followed in their evolution as long as the resolution of the computational grid is reasonably good, whereas are rapidly damped when the grids stretches

towards the outflow. In the Fig. 22 are also visible the vortices that form at the root of the blades and eventually merge into the hub vortex.
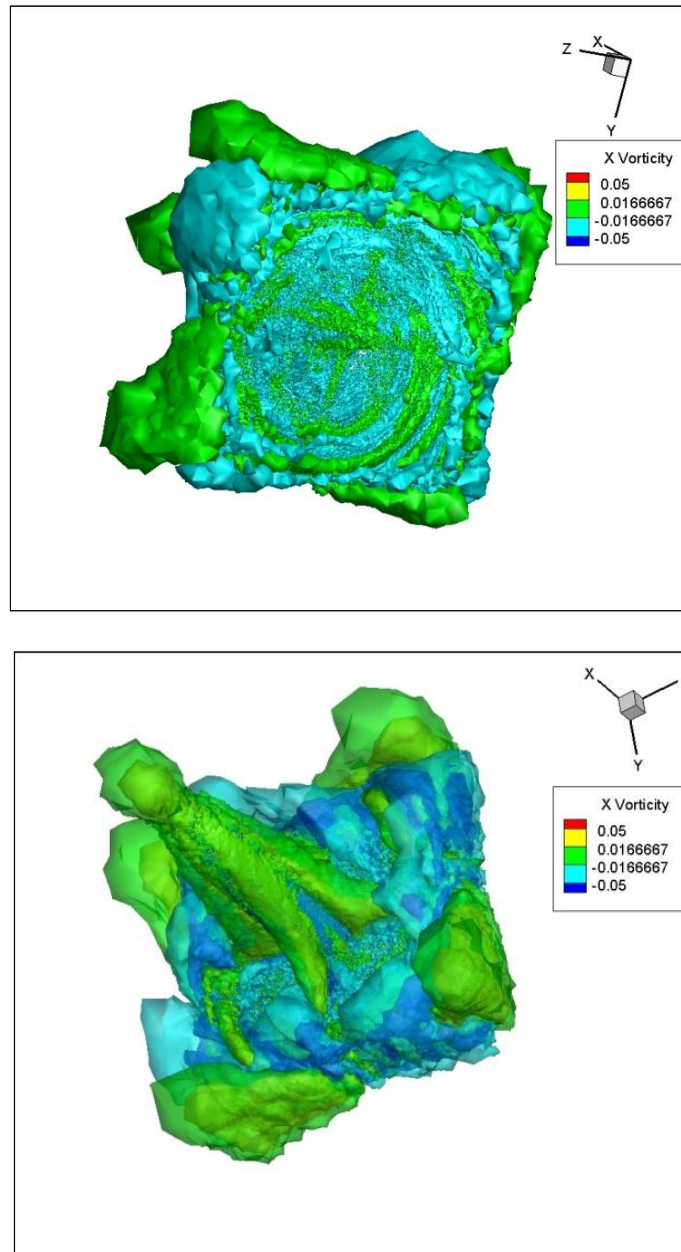

Figure 22: X-vorticity around the propeller for J=1.8

The effect of a nacelle on the distribution of the loading on a propeller for maximum efficiency can be developed from the requirement that the trailing vortex system be a helicoidal sheet moving as if rigid, exactly as in the case of an isolated propeller. First consider

an ideally loaded propeller moving in free air without interference from any adjacent body. At some distance behind the propeller the trailing vortices appear as a regular helicoidal sheet. Now, at some lesser distance behind the propeller, interpose on its axis a streamlined nacelle. The nacelle, being at a sufficient distance, has no effect on the propeller.

Neglecting viscous effects and the instability of vortex sheets, it also has no effect on the final form of the vortex system, which will flow around the nacelle and finally resume its fixed helicoidal form.

Now consider how the propeller must be modified if it is moved downstream to a position immediately in front of the nacelle and is required to give rise to the same final form of the trailing vortex system, the remote helicoidal trailing vortex sheet being regarded as an unchanging given (Fig. 23). The flow in front of the nacelle will be retarded and there will be a radial displacement of streamlines. As it is moved to proximity to the nacelle, blade elements of the free running propeller must be displaced radially and the bound circulation of each element must remain unchanged if the final trailing vortex system is to remain unchanged.
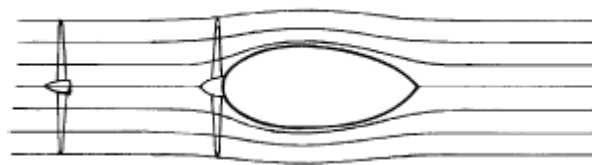
Figure 23: A free running propeller and an equivalent propeller on a nacelle

Since, in locating the propeller close to the nacelle, the relative peripheral velocity at a blade element is subject to little change while the axial component may be substantially reduced by an additional interference from the nacelle, the angle of attack and the circulation will be increased unless the local blade angle b is reduced. The design of a propeller in the presence of a nacelle with ideal load distribution requires the determination of the radial

coordinates of blade elements in relation to the radii of the hypothesized free-running propeller and the determination of the blade angle which results in the proper bound circulation.

The flow around the nacelle may be described by a distribution of sources and sinks on the axis.

However, the flow in the region of a propeller just ahead of a nacelle or fuselage is probably adequately represented by a single source.

The transformation of the design of a free-running propeller to a propeller at the nose of a nacelle will result in the stretching of the circulation distribution over a greater radius. This will usually result in a somewhat greater thrust, but both propellers result in the same trailing helicoidal vortex system, hence the same net thrust. The difference is due to a drag force on the nacelle induced by the proximity of the propeller. We may also observe that the design of a pusher propeller with ideal load distribution is, if we neglect the effects of viscosity, exactly the same as for a tractor propeller.

In Fig. 24 and Fig. 25 the axial velocity profiles downstream the blades are shown at different position of x and it is possible to note how the swirl induced by the rotation of the propeller vanishes with the increasing of the distance from the blades.

To understand this phenomenon, we can hypothesize that the blade elements lie on radial lines and may be considered to act as two-dimensional foils upon which the forces are the same as would be found in a uniform two-dimensional flow with the same local velocity and direction. For this to be justifiable, the velocity field must be effectively uniform in the immediate region of the airfoil. Aircraft propeller blades are almost always narrow enough that this assumption is reasonable. It is possible to develop a correction to the camber of

73

blade elements to compensate for the curvature of the velocity field, but this refinement is probably not worthwhile for typical aircraft propellers.

From the following argument it can readily be seen that the induced velocities at the propeller plane tend to be half the induced velocity at a corresponding point on the helicoidal vortex sheet far behind the propeller.

Assume a set of equally spaced right helicoidal vortex sheets extending in both directions from a plane normal to the axis. Consider any point on the vortex sheets where they intersect the plane. From the Biot–Savart law, it can be seen that the induced velocity at such a point due to a vortex element at an arbitrary distance from the plane is exactly equal and in the same sense as the velocity induced by a like element at the same distance in the other direction from the plane (See Appendix B). Consequently, if the helicoidal vortices are semi-infinite, extending in only one direction from the plane, the velocities on the plane will be half what they would be for the doubly infinite system. This is taken as an adequate approximation for the velocities induced at the propeller plane by the trailing vortex system except that the tangential velocity is modified for the effect of radial displacement of the trailing vortex system immediately behind the propeller.

It must be recognized that representing the vortex system behind the propeller by regular semi-infinite helicoidal vortex sheets is a simplification since both the pitch and the radius of the vortices will be modified to some extent immediately behind the propeller. Also, the helicoidal sheets are unstable and at some distance behind the propeller will roll up into a set of helical vortex filaments, one for each blade, and another of opposite sense on the axis. It was shown that the rolling up of the sheets at a distance from the propeller has no significant effect on the velocity field at the propeller, but the contraction of the trailing vortex system immediately behind the propeller must be taken into account. The exception to this is the case

of a lightly loaded propeller where a simplified treatment is appropriate. The radial displacement of the trailing vortex system immediately behind the propeller occurs in any case and is augmented by the effect of a hub of significant size. The effect of the radial displacement is taken into account by observing that the circulation as measured by a line integral on a circle of radius r must be the same at any plane behind the propeller when r is drawn through the same vortex filament.
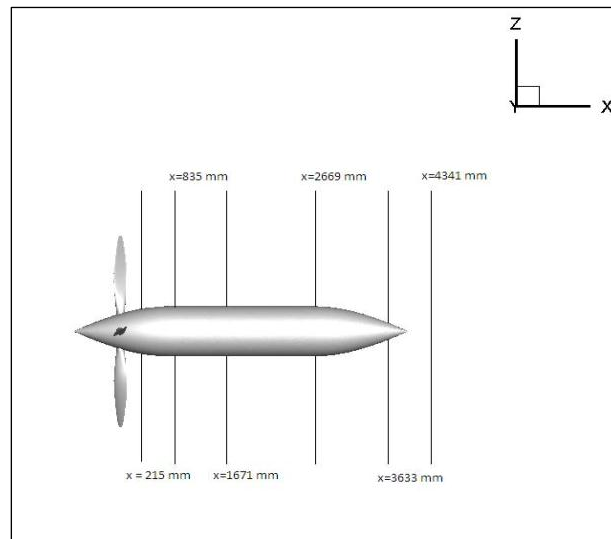
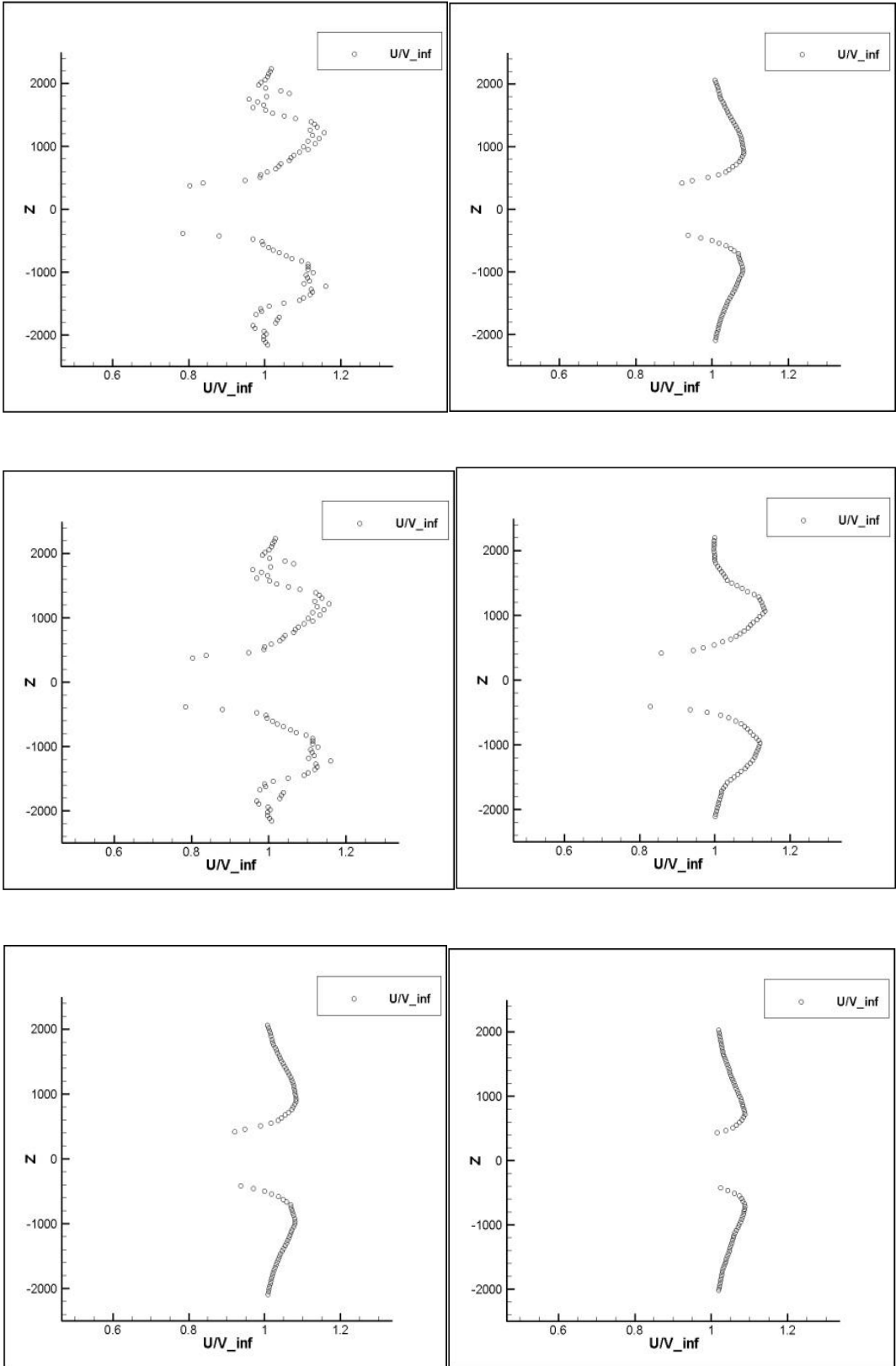Figure 24: Sections for the analysis of the axial velocity profiles

Figure 25: Axial velocity profiles downstream the blades at positions of Fig. 8 for J=1.8.

With the aim of comparing the results with those obtained by Biermann and Haetman [4], the thrust coefficient, defined as:

$$C_T = \frac{T}{\rho n^2 D^4} \tag{99}$$

has been calculated. Following the experimental procedure adopted by D. Biermann and Eiiwin P. Haetman [4] the thrust force *T* has been obtained by integrating the forces along x-direction on all the blade surfaces, and subtracting the drag force due the blades alone, in case of zero thrust coefficient.

In the following figure (Fig. 26), the obtained thrust coefficients for five different advance ratio are

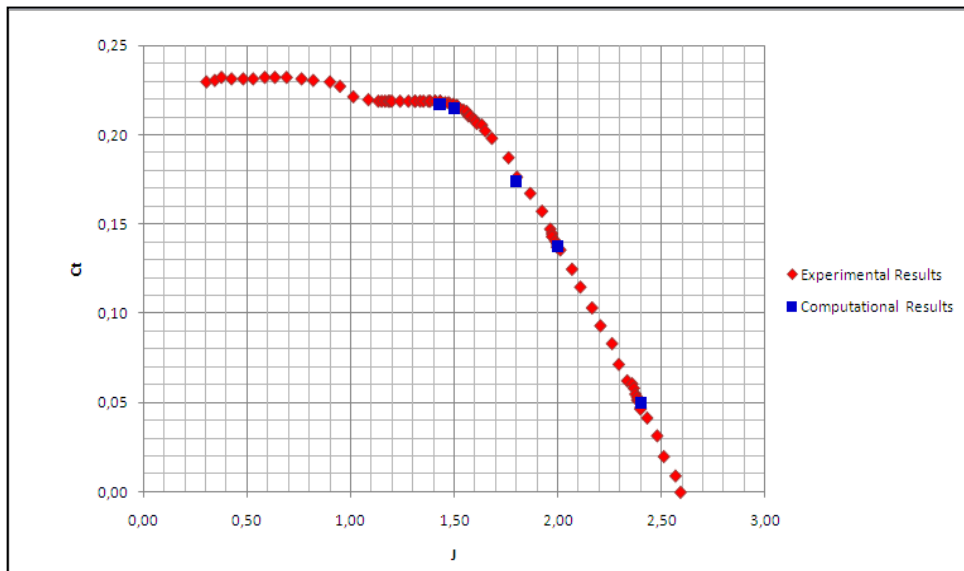Plotted and compared with those obtained by Biermann and Haetman [4].

Figure 26: Computed vs experimental thrust coefficient.

The computed thrust coefficients are in good agreement with the experimental values with (Table 4):

Table 4 Experimental and computational results for the thrust coefficient

Advance Ratio J	Experimental C_T	Computational C_T
1.43	0.2192	0.217
1.5	0.2175	0.215
1.8	0.1782	0.174
2.0	0.1374	0.1376
2.4	0.0487	0.05

As the experimental errors are unknown, it is not possible to determinate whether the computed results are or not within the range of the experimental uncertainty and to give a precise assessment of the quality of the results.

2.3. Results for the four-blade single-rotating propeller + spinner + wing (inviscid)

Steady Euler results for the propeller+spinner+wing are presented in this section. The grid is generated with ICEM-CFD (Fig. 27) and it is made by:

- 2173935 nodes

- 10718702 elements
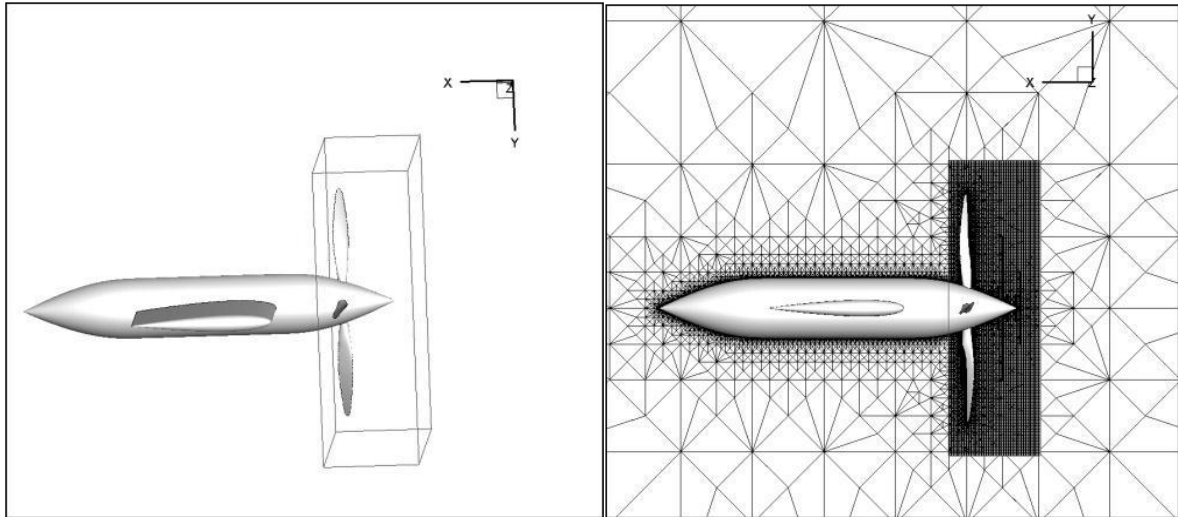
Figure 27: Rotating block within the mesh: a) propeller, b) mesh inside the block.

A rotational velocity has been imposed for the nodes inside the block around the blades, as indicated in Fig. 27. The investigated operating conditions are the same of the previous case. The pressure gradients in spanwise direction are moderate except for the wing-nacelle juncture region. At that location a typical pattern is obtained that demonstrates a small loss of lift. Although the pressure distribution changes dramatically (large differences between wing upper and lower side) when the angle of attack is increased, still a rather small spanwise gradient is maintained. This is important with respect to the changes that the slipstream exhibits when it strikes the wing (Fig. 28).

Although some disturbances are found at the wing tip, it is expected that the wing tip flow pattern has only minor influence on the propeller-wing interactive flow at the more inboard located position.
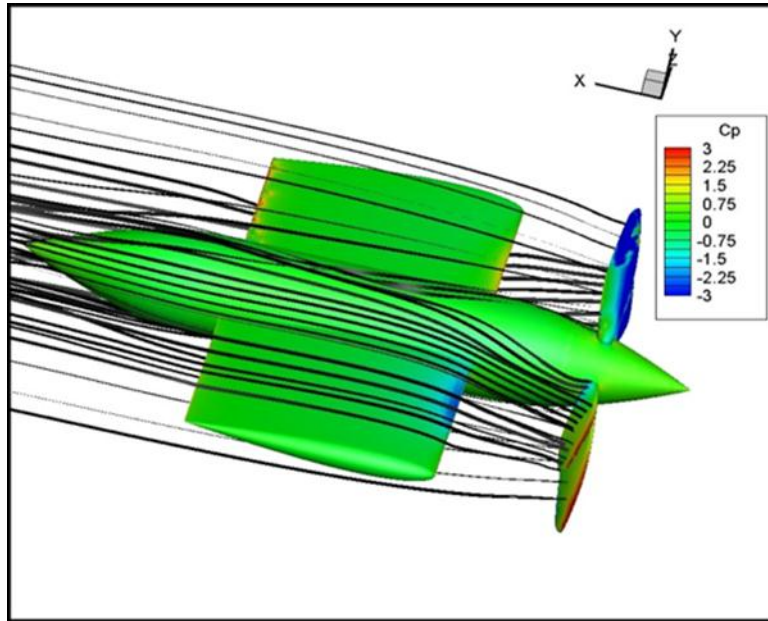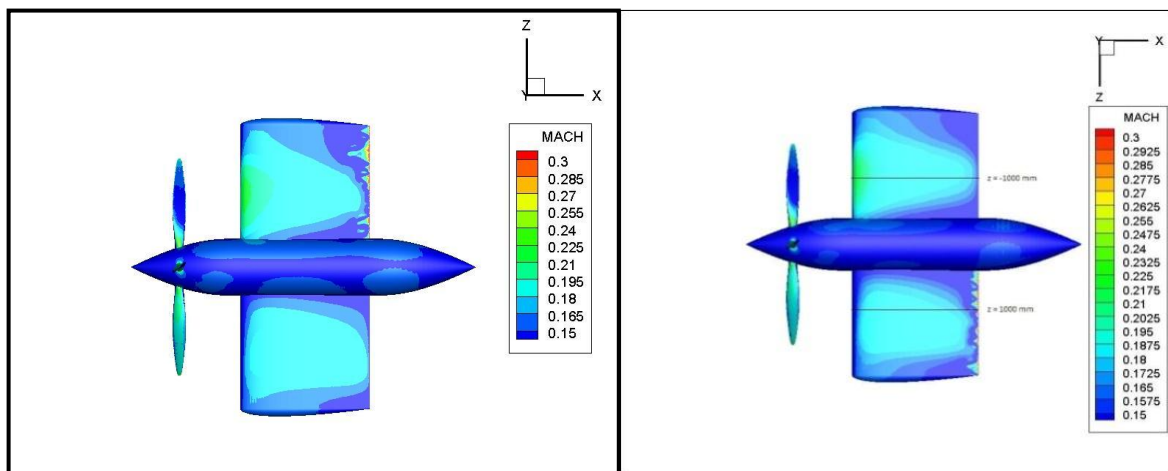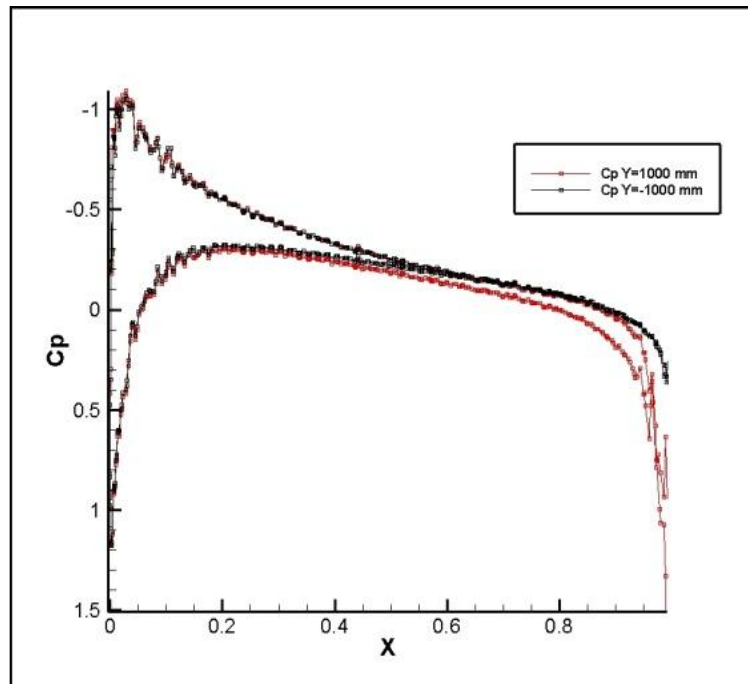
Figure 28: Sleapstream around the propeller for J=1.43

Figure 29: Mach number: a) upper side for J=1.8, b) lower side for J=1.8; c) Cp on surface for y=1000 mm and y=-1000 mm.

The Mach distributions in Fig. 29 clearly show the effect of the propeller slipstream that washes the wing. Especially, the impact of the swirl velocity component is very pronounced. The high axial velocity induced by the propeller increase the dynamic pressure of the fluid in the slipstream.

It is clear that the Mach number distribution on the section has changed due to the slipstream.

The swirl velocity of the slipstream changes the local attack angle of the wing which immerse in it.

The propeller induced upwash at the up going blade side leads to an increased local attack angle while downwash at the down going blade side leads to a decreased local attack angle.

The wing has an increased lift at the up going blade side and decreased lift at the down going blade side.

The capability of the UNS3D code to incorporate the deformation of the slipstream, as sketched in Fig. 28, is essential for a detailed analysis of the propeller-wing interactive flow.

The strongest point of the UNS3D code in the analysis of the propeller-wing interaction problem is its intrinsic modeling of the swirl recovery effects. Furthermore, no user intervention is needed to prescribe the slipstream position within the computational domain.
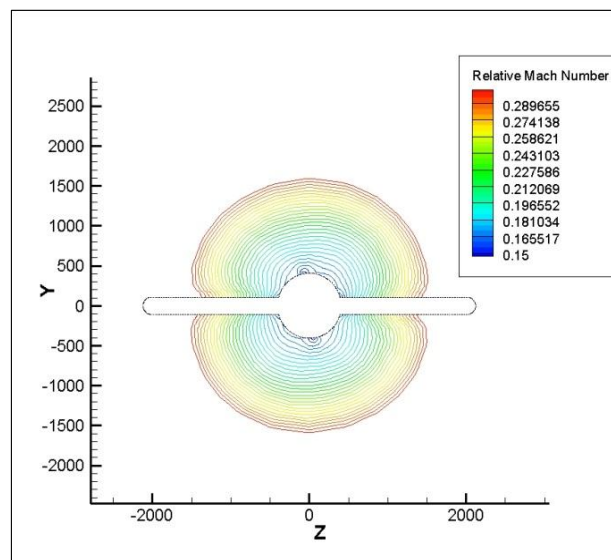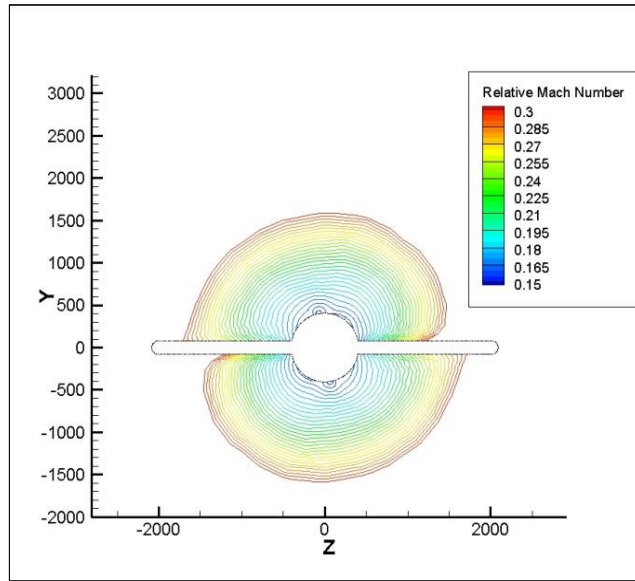
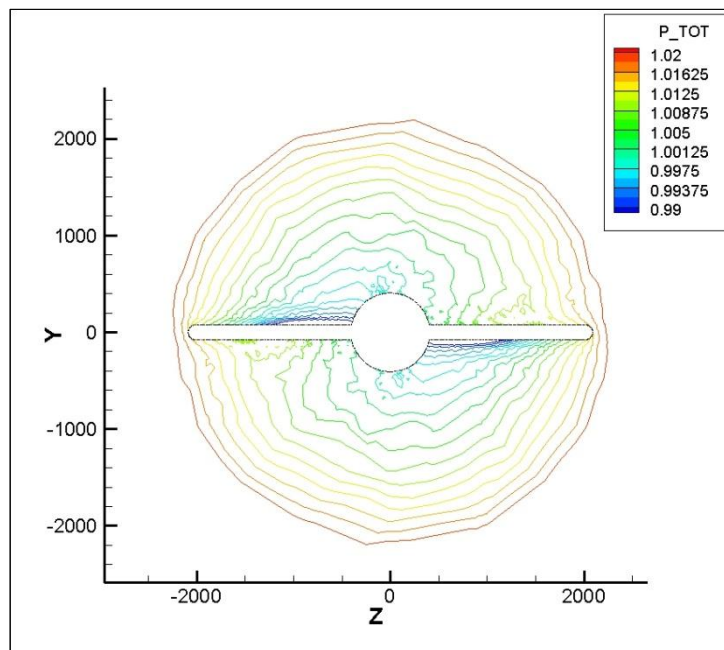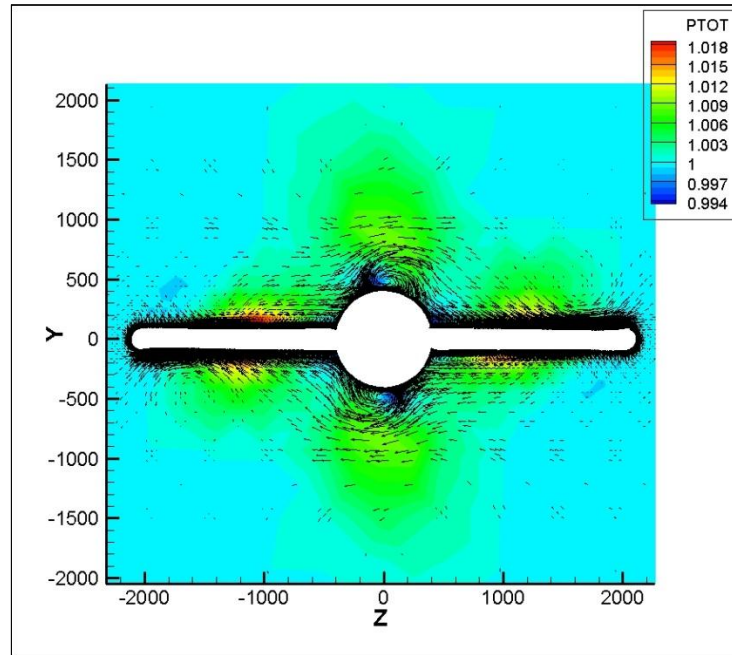**Figure 30:** Relative Mach number in x =1000 mm and x = 1500 mm for J=1.8

**Figure 31:** Total pressure contours in the plane (y,z) for J=1.43

Figure 32: Total pressure and streamline in the plane (y,z) for J=1.43

It should be reminded that the relative Mach number distributions (Fig. 30), like so the total pressure distributions, as presented in Fig. 31-32, are affected both by the local propeller induced flow angles and the dynamic pressure increasing in the slipstream.

Since the slipstream consists of a swirl and an axial velocity component as well as a pressure jump, with reference to the undisturbed flow, the lift distribution and with it the overall wing coefficients, are strongly affected. As a result of the modified flow pattern due to the propeller the effects are not confined to the wing part within the slipstream but to parts outside of it as well.

The axial and the swirl velocity induced by the propeller both have their own very specific influence on the flow over the wing. The axial velocity (or alternatively the dynamic pressure) increase does not change the local lift and drag coefficient when based on the local flow conditions inside the slipstream, the local forces, however, are strongly affected. The axial velocity distribution is non-uniform; it changes radically in radial direction. Depending on the vertical position of the propeller the wing cross sections are thus more or less affected with

higher dynamic pressure values leading to higher values of the local lift- and drag coefficient, based on the undisturbed flow conditions. With the axial velocity distribution symmetrical with respect to the propeller thrust axis the effect on the wing load is equal for both the inboard and outboard side of the nacelle (Fig. 33).
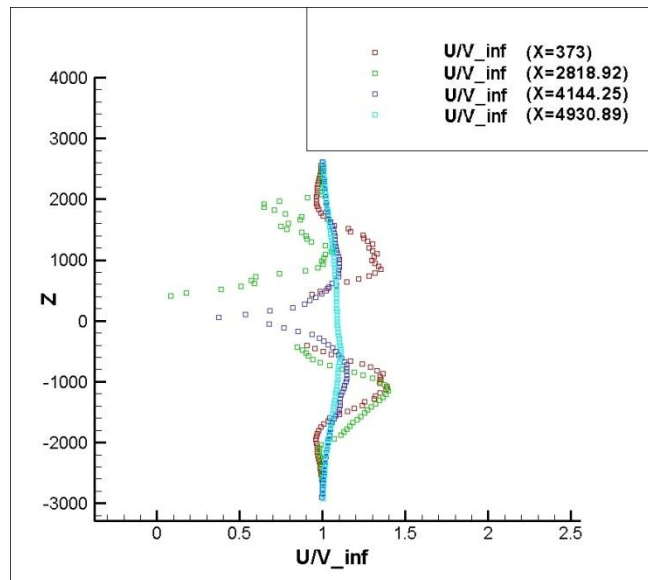
Figure 33: Axial velocity for J=1.43

Contrary to this, the effect of the swirl velocity component is anti-symmetrical. The propeller induced upwash at the upgoing blade side (UBS) introduces an angle of attack increase while the component at the downgoing blade side (DBS) leads to a decreased local wing angle of attack. With the wing at a positive angle of attack the wing generates a positive lift that results in an augmented lift at the UBS and decreased lift at the DBS.

Due to the anti-symmetrical character of the swirl velocity the rotation direction of propeller dominates the final shape of the spanwise wing loading distribution.

Combining the effects of the axial and the tangential velocity components in the slipstream and taking into account changes in the loading distribution outside the slipstream domain the picture becomes more complicated. As sketched in Fig. 28-29 wing regions are directly influenced by the slipstream that washes the wing. The lift effect of the propeller swirl

85

velocity, that changes the local wing angle of attack, is enhanced by the increased dynamic pressure. Considering the inboard up rotation case, in W-III these two slipstream effects counteract each other. The result is a smaller difference between the powered and unpowered case in this region. It can be clearly seen that the propeller effect is not limited to the wing part (with a span equal to the contracted slipstream diameter) directly behind the propeller. Due to the changed wing inflow conditions generated by the propeller the loading in some particular regions changes as well, both for the inboard up and outboard up running propeller. This is the result of the distorted vorticity sheet that leaves the wing.

The total pressure distribution on each blade face is a superposition of the pressure due to the thickness effect which produces no lift, on the pressures arising from the effects of "non-planar" thickness camber and angle of attack of the blade and of spatial non-uniformity of the inflow field.

The last four components contribute to the lift because each produces a pressure difference between the back and front faces of the blade surface.
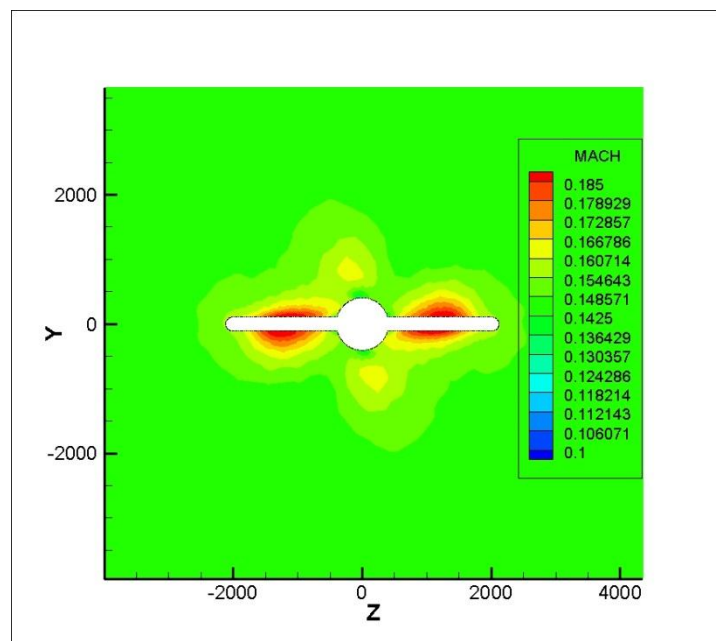
Figure 34: Mach number in the plane (y,z) for J=1.8

86
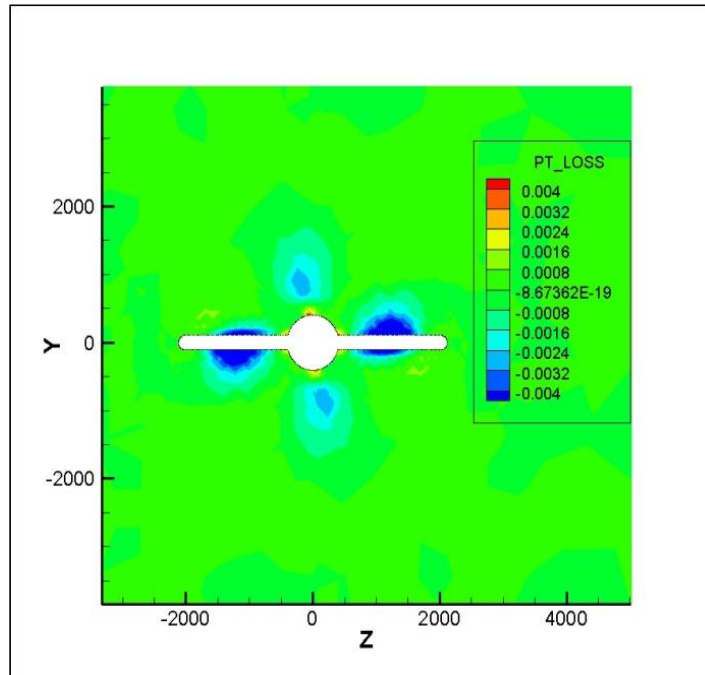
Figure 35: Total pressure loss in the plane (y,z) for J=1.8

An-other phenomenon that is clearly visible, due to the interference between the propeller and the wing, is the rise of vortices around the juncture of spinner and wing (Fig. 36). A shedding of these vortices can be individuated, which is indicative of the high gradient of spanwise load on the wing.

The vortices can be followed in their evolution as long as the resolution of the computational grid is reasonably good, whereas are rapidly damped when the grids stretches towards the outflow. In the Fig. 32-36 are also visible the vortices that form at the root of the blades and eventually merge into the hub vortex. From the Fig. 30 can be clearly seen the contraction of the flow tube caused by the acceleration induced by the propeller and, from a numerical standpoint, the rapid destruction of the vortex due to the mesh coarsening.
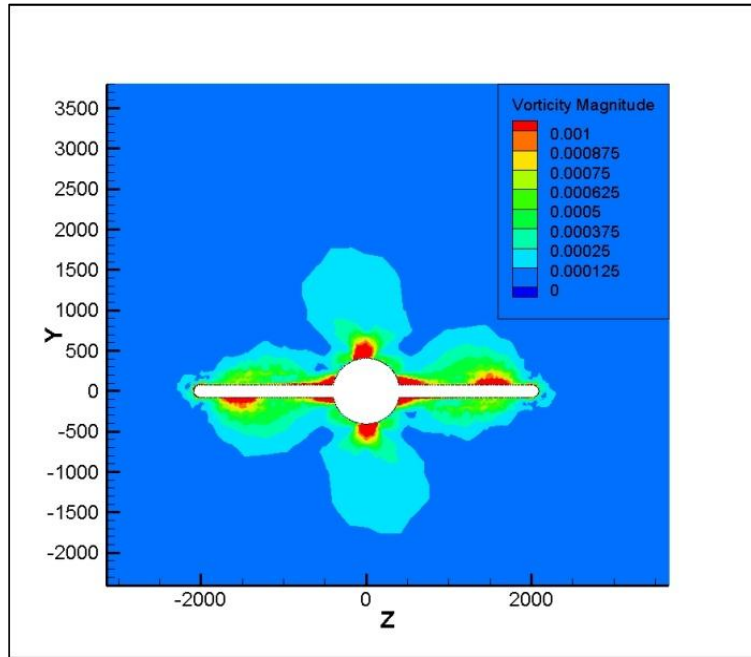
Figure 36: Vorticity magnitude in the plane (y,z) for J=1.8.
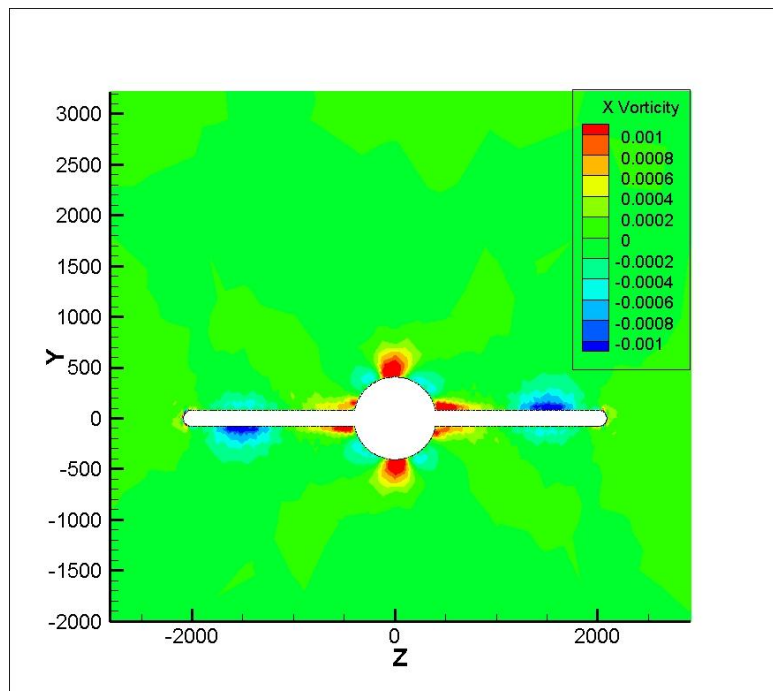
Figure 37: X-vorticity magnitude in the plane (y,z) for J=1.8.

In fact, the streamwise and spanwise locations of blade vortices are staggered on the upper and lower surfaces of wing and interacted vortices are induced near spinner.

In order to make a further verification of the method the numerical calculations have been compared to experimental data (Fig. 38).
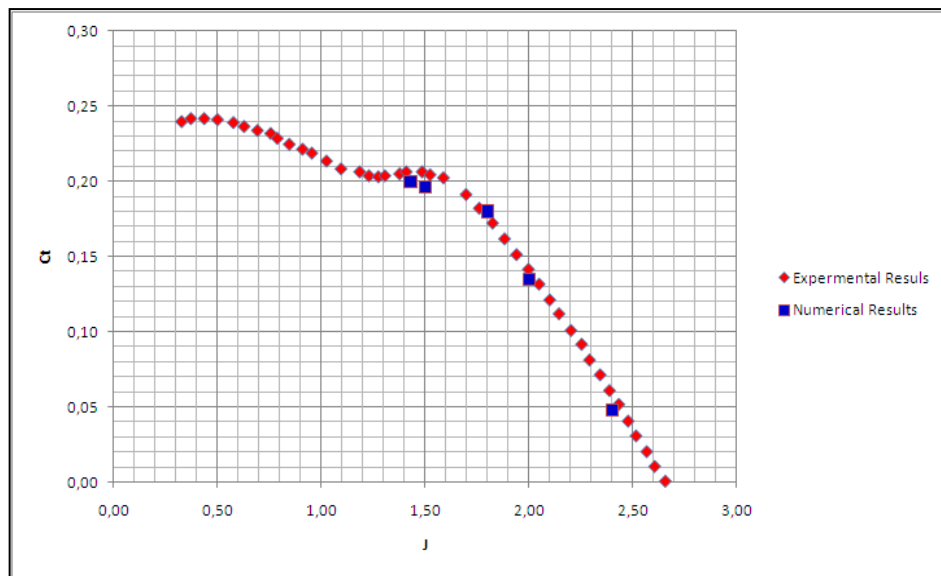
Figure 38: Computed vs experimental thrust coefficient

Again, the computational results are in good agreement with the experiment and the maximum error is around 5% (Table 5). Also in this case the experimental errors is unknown.

Once accurate results are needed for the propeller-wing interference problem and details of the flow are needed to determine the secondary flow effects that influence the drag performance of the model, which is very important for the estimation of the thrust force, the UNS3D code becomes indispensable.

This approach facilitated the identification of typical flow phenomena, like the deformation of the slipstream when passing the wing. The spanwise distributions of the drag force are sensitive to the form the velocity distribution in the slipstream as well as the way the

slipstream deforms when passing the wing. Hence, a calculation model based on the NS-equation, respect to the other mathematical models (Appendix A), yields a more realistic estimation of the propeller wing interactive flow since the slipstream is allowed to develop and deform freely and no artificial swirl recovery is needed.

Table 5 Experimental and computational results for the thrust coefficient

Advance Ratio J	Experimental C_T	Computational C_T
1.43	0.206	0.2
1.5	0.2052	0.196
1.8	0.175	0.18
2.0	0.14	0.135
2.4	0.049	0.054

Chapter V

Conclusions

The Alenia Aermacchi UNS3D code was modified, introducing the capability of flow simulations in a non inertial frame of reference. The modified code was at first applied to the computation of damping derivatives of a rotating profiles, then to the prediction of the performance of a propeller, following the experimental test case described by Biermann and Haetman [5], for different rotational speeds. In the first case, good agreement has been obtained with the numerical results of [10]. In the second, the results are in good agreement with the experimental data within the propeller operating range. The computational results clearly showed the effect of the swirl velocity and the increased total pressure on the spinner and the wing. Therefore, this approach facilitates the identification of typical flow phenomena, like the deformation of the slipstream when passing the wing, being able to model aerodynamic phenomena linked to the propeller-airframe integration.

Appendix A

Engineering methods for the estimation of propeller data

1.   Introduction

To be able to work with the flow phenomena that occur in propeller flow it is beneficial to shortly restate the typical propeller flow characteristics and discuss methods by which both the propeller force as well as the slipstream parameters can be obtained.

A logical step towards the analysis of the propeller is to consider a propeller that operates in an undisturbed uniform flow generating a slipstream that is free of any disturbance caused by the proximity of a nacelle or any other airframe part. The flow field that is generated is very similar to that of a wing. The local lift on the blade section at any radial position is associated with the local circulation around the blade. This circulation varies from the blade root to the blade tip resulting in the shedding of a vortex sheet from the blade trailing edge, as sketched in Fig. A.1.
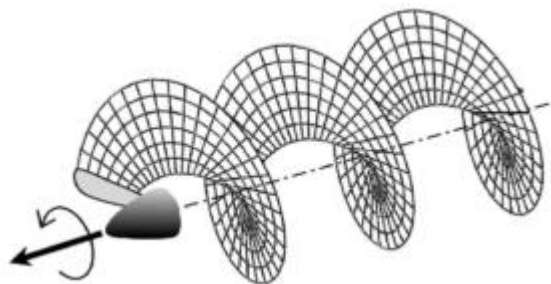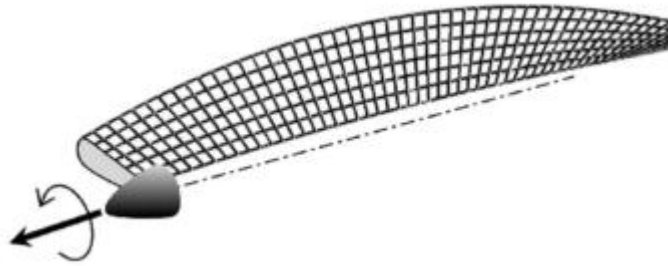
Figure A.1: Sketch of a vortical wake generated by a propeller blade

The vortex sheets of all blades pass downstream in a helical path together forming the slipstream. The vortex sheets springing from all propeller blades are free to move under their own self-induced influence and the influence of the other sheets. The resulting slipstream shows a contraction as it moves downstream due to the increasing axial velocity inside the slipstream tube. The bound vorticity on the propeller blades and the trailing vorticity generate a propeller induced velocity vector. This local induced velocity can be added vectorially to the free stream velocity and the local rotational velocity of the blades to form the total local velocity vector in a fixed (Eulerian) frame of reference. Once the slipstream is generated in the form of helical wakes its geometry will change gradually as it progresses downstream. This deformation of the slipstream tube is the result of both the contraction and the rolling up of the vorticity sheets into a discrete tip and root vortex. The distance over which this process takes place is dependent on the propeller loading since this strongly determines the advance ratio of the blade wakes (see Fig. A.1).

An attractive starting point to describe possible losses and gains for the propeller is found in the description of the so-called free air thrust. This is the thrust of the propeller blades without any other aircraft part present. The induced losses are typically the effect of the axial and swirl velocity components generated by the helical vortex sheets that emanate from the

blades. In case of interference with other aircraft parts these velocities will of course be strongly affected.

The loss in efficiency due to blade airfoil drag is related to the drag of the blade airfoil sections and are insofar rather independent on the selection of the three-dimensional propeller blade geometry and the propeller position relative to other aircraft parts. To reduce the profile losses the airfoil sections will be designed to produce a high lift to drag ratio, C_l/C_d, over a wide range of propeller inflow conditions, i.e. a range of advance ratios that the propeller experiences going from take-off to cruise condition. The final selection of the airfoils is therefore based on a compromise aiming at high efficiency at a specified flight condition (generally the cruise phase) whilst maintaining acceptable penalties for other flight phases. Accordingly the profile loss associated effects are part of the propeller design process which is only loosely related to the propeller wing interference problem.

On the other hand, the induced loss of the propeller is an important issue when treating the propeller wing interaction effects. Because the inflow conditions of the

propeller are mainly dictated by the propeller-airframe configuration the loading distribution on the propeller blades and, consequently, the trailing vortex system will change with reference to the uninstalled propeller condition. Even though the free air efficiency is an interesting property as far as propeller design is concerned the most important condition for the treatment of the performance of the complete aircraft will be the installed propeller case. In the next sections first of all the main features of the uninstalled propeller and various methods to calculate the performance will be discussed.

2. Actuator disk theory

The thrust delivered by a propeller can be achieved by imparting axial momentum to the passing fluid to force a backward motion. The energy associated to the fluid is an inevitable loss. The original theory, as first formulated by Rankine and Froude, excludes the viscous effects, the rotation of the slipstream, and the uneven load distribution, with the scope of evaluating the ideal efficiency of such a propulsive system (also called actuator disc).

The rotor is degenerated into a disc perpendicular to the direction of the thrust, and is capable of sustaining a pressure difference between its two sides, and of generating/imparting linear momentum to the fluid that passes through it. The determination of the thrust requires the evaluation of the mass flow through a stream tube bounded by the disc. In a later refinement the load distribution on the disc was taken into account with the momentum equation, and led to the conclusion that the load (i.e. the pressure difference), in fact, must be constant over the actuator disc to produce optimal thrust (e.g. with minimum energy losses). With this in mind the actuator disk theory is discussed briefly.

The momentum theory of propellers, as proposed decades ago by Rankine and Froude, provides a basic understanding of various aspects related to the performance of propellers. As sketched in Fig. A.2 the propeller is approximated by an infinitely thin actuator disk across
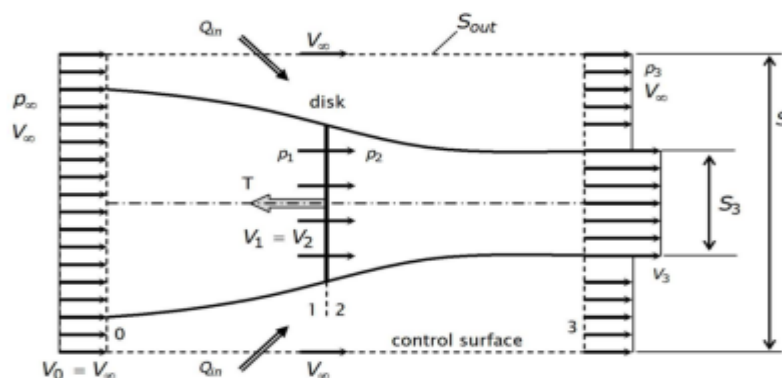
Figure A.2: Actuator disk model with control volume for the application of the momentum equation

which the static pressure rises in a discontinuous way. Important simplifications that are applied in this model can be summarized as follows:

- both the pressure and the velocity are distributed uniformly over the disk

- the rotation (swirl) imparted to the flow as it passes the disk plane is completely neglected

- the flow passing through the propeller disk can be separated from the rest of the flow by a streamtube

- the flow is assumed to be incompressible

In order to apply the momentum theory, four planes, 0 to 3, all perpendicular to the thrust axis, are defined. Planes 0 and 3 are assumed to be lying far upstream and far downstream of the disk respectively. Planes 1 and 2 are positioned just in front of and behind the propeller (Fig. A.2). This means that the local static pressure in the these planes is constant and equal to the undisturbed pressure, p.

A volume exists across the inflow plane, with surface area S, the outflow plane with the same area and the cylindrical surface S. The flux passing out of the surface across plane 3 minus the flux entering across plane 0 will be:

$$\Delta Q = S_3 V_3 + (S - S_3)V_\infty - SV_\infty \qquad (A.1)$$

$$\Delta Q = S_3(V_3 - V_\infty) \qquad (A.2)$$

If $V_3 \neq V_\infty$, a flux enters the control volume from the side. When the cylindrical control volume is chosen large enough the external pressure forces cancel out. In this case the momentum equation results in:

$$T = \rho S_3 V_3^2 + \rho(S - S_3)V_\infty^2 - \rho S V_\infty^2 - \rho \Delta Q \, V_\infty \qquad (A.3)$$

With equation (A.2) this leads to:

$$T = \rho S_3 V_3 (V_3 - V_\infty) \qquad (A.4)$$

Where $\rho S_3 V_3$ is equal to the mass flux passing through the propeller plane. Alternatively

the thrust of the propeller can be derived from the pressure force acting on the actuator disc plane:

$$T = S_p(p_2 - p_1) \qquad (A.5)$$

Where $S_p = S_1 = S_2$ is the propeller disk area.

To relate p_1 and p_2 Bernoulli's equation can be applied both for the domain upstream and downstream the propeller:

$$p_\infty + \frac{1}{2}\rho V_\infty^2 = p_1 + \frac{1}{2}\rho V_1^2 \qquad (A.6)$$

$$p_2 + \frac{1}{2}\rho V_2^2 = p_\infty + \frac{1}{2}\rho V_\infty^2 \qquad (A.7)$$

Subtracting equation (A.6) from equation (A.7) and noting that the velocity is continuous across the propeller disk leads to:

$$p_2 - p_1 = \frac{1}{2}\rho(V_3^2 - V_\infty^2) \qquad (A.8)$$

From the continuity equation it follows that :

$$S_p V_p = S_3 V_3 \qquad (A.9)$$

Combining this with equations (A.4)-(A.5)-(A.8) results in:

$$V_p = \frac{V_3 + V_\infty}{2} \qquad (A.10)$$

So, we conclude that the velocity at the location of the propeller is equal to the average of the velocity far upstream and far downstream of the propeller. With the propeller induced axial velocity increase at the propeller plane, v_a:

$$V_p = V_\infty + v_a \qquad (A.11)$$

the thrust can be written as:

$$T = 2\rho S_p (V_\infty + v_a) v_a \qquad (A.12)$$

To determine the efficiency of the propeller a relation for the power has to be established. From the increase in kinetic energy of the flow the power can be written as:

$$P = \frac{1}{2}\rho S_p (V_\infty + v_a)\{(V_\infty + 2v_a)^2 - V_\infty^2\} \qquad (A.13)$$

Substitution of equation (A.12) leads to the following important result:

$$P = T(V_\infty + v_a) \qquad (A.14)$$

The efficiency of the propeller is the ratio between the useful power and the power that is absorbed. Hence:

$$\eta = \frac{TV_\infty}{P} = \frac{TV_\infty}{T(V_\infty + v_{a)}} \qquad (A.15)$$

or:

$$\eta = \frac{1}{1 + v_a/V_\infty} \qquad (A.16)$$

Solving equation (A.12) for v_a leads to:

$$v_a = \frac{1}{2}\left(-V_\infty + \sqrt{V_\infty^2 + (2T/\rho S_p)}\right) \qquad (A.17)$$

With the definition for the thrust coefficient, $C_T = T/\frac{1}{2}\rho V_\infty^2 S_p$, the combination of equation (A.16) and (A.17) the efficiency of the propeller can be written as:

$$\eta = \frac{2}{1 + \sqrt{1 + C_T}} \qquad (A.18)$$

This means that the propeller efficiency approaches unity when the disk loading (and therefore the thrust coefficient) approaches zero.

Expression (A.18) represents the theoretical maximum value of the efficiency. This value is however not attainable in practice since the momentum equation neglects viscous losses due to the boundary layer on the propeller blades. Moreover, additional induced losses arise due to the loss of lift near the propeller tips. The helically shaped vortex system that is produced as a result reduces the efficiency even further similar to the performance degradation of a wing due to the tip vortices.

Although the actuator disk model, based on the momentum equation, fails to accurately predict the power of a propeller it is very useful for estimating the propeller induced axial velocity in the slipstream, as indicated above.

3. Vortex Theory

The actuator disk theory helped in the understanding of propellers but failed to relate the blade loading with the propeller geometry and operating conditions. Prandtl [32] introduced the lifting line theory in which he described the lift of finite wings in three dimensional flow introducing the idea of a trailing vortex sheet. The basis effect of the vortex sheet is to induce velocities at the location of the wing (or bound vortex) which can be calculated with the Biot-Savart Law. For the special case of an elliptically loaded wing the induced angle of attack will be constant.

In reality, the vortex sheet is not stable and tends to roll up behind the wing into two distinct "tip vortices". If however if the vortex sheet that leaves the wing is assumed to stay flat its position will vary in a state of uniform motion perpendicular to itself. The downwash angle far downstream will then be twice the value as found at the location of the wing. This picture led the way to the vortex theory of propellers assuming that an equivalent vortex system will be produced by the rotating propeller blades .

The vortex theory, developed by Betz [25], assumes a rigid "wake" and can be used to design a minimum induced loss propeller in analogy with the elliptical wing which produces minimum induced drag. The optimum distribution of the circulation along the propeller blade produces a propeller with maximum efficiency excluding any viscous losses due the profile drag of the propeller blade sections.

From the known optimum circulation distribution the optimum value of the local loading, expressed in $C_l \cdot c$, is found for one specific operation condition of the propeller. Now combinations of blade angle distributions and chord distributions can be produced delivering an optimum (minimum induced loss) propeller.

If the focus is on the analysis of a given propeller, rather than the design of a new propeller, the vortex theory of propeller is of little use. Especially when the slipstream characteristics of a given propeller are the subject of research a more extended procedure as outline in section 4 is to be used as a starting point. One concept however that can be described based on the original vortex theory of propellers is the so-called "Tip loss factor", denoted with F. To understand its importance for the description of the inflow field of a propeller the derivation of an expression for F will be summarized here, based on the so-called displacement velocity.

Consider an elementary helical vortex filament being part of in a helical vortex sheet which forms part of the slipstream of a propeller as shown in Fig. A.4. The vortex filament is constrained to move everywhere perpendicular to itself with a velocity w_s, which is the same as the local slipstream velocity. When the local helix angle is φ_s, the axial velocity becomes $w_s \cos(\varphi_s)$ and the circumferential velocity $w_s \sin(\varphi_s)/r_s$, where r_s is the local helix radius. For an observer that is unaware of the angular velocity it seems that the vortex filament has a displacement velocity:

$$v_n = w_s \cos(\varphi_s) \qquad (A.19)$$

Betz [25] shows that for a propeller of minimum induced loss the displacement velocity is constant in blade spanwise direction (i.e. radially constant). The axial component and the swirl component of the vortex sheet are then given by:
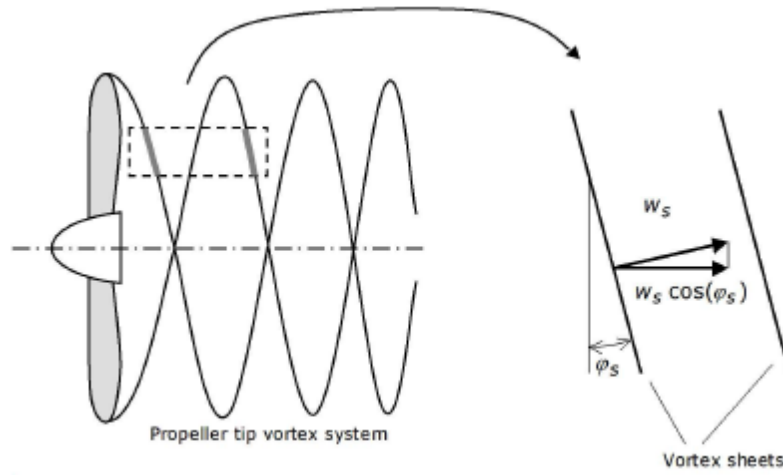
Figure A.3: True and apparent transport velocity of the vortex sheets behind the propeller blade

$$
\begin{aligned}
w_{ax} &= w_s \cos(\varphi_s) = v_n cos^2(\varphi_s) \\
w_{sw} &= w_s \sin(\varphi_s) = v_n \cos(\varphi_s) \sin(\varphi_s)
\end{aligned}
\qquad (A.20)
$$

When the advance ratio is small or the number of blades is high enough the distance between the vortex sheets, produced by two succeeding blades, will be small.

Based on this model Prandtl showed that the fluid velocity between the sheets is a fraction F of the vortex sheet velocity. Prandtl realized that that at small values of r_s the velocity between the vortex sheets will be approximately the same as the local displacement velocity of the sheets.

Further he indicated that then local flow velocity at the outer edge of the vortex sheet will be different from the displacement velocity. This flow type now exhibits much similarity with the 2-dimensional flow along the edges of parallel plates in a uniform flow as sketched in Fig. A.4.

For this particular flow field the ratio between the local average flow velocity between the plates, $\overline{v_n}$ and the speed of the plates with reference to the undisturbed flow at great distance from the plate, v_n, becomes:

$$\frac{\overline{v_n}}{v_n} = \frac{2}{\pi} \arccos\left(e^{-\frac{\pi d}{s}}\right) \qquad (A.21)$$
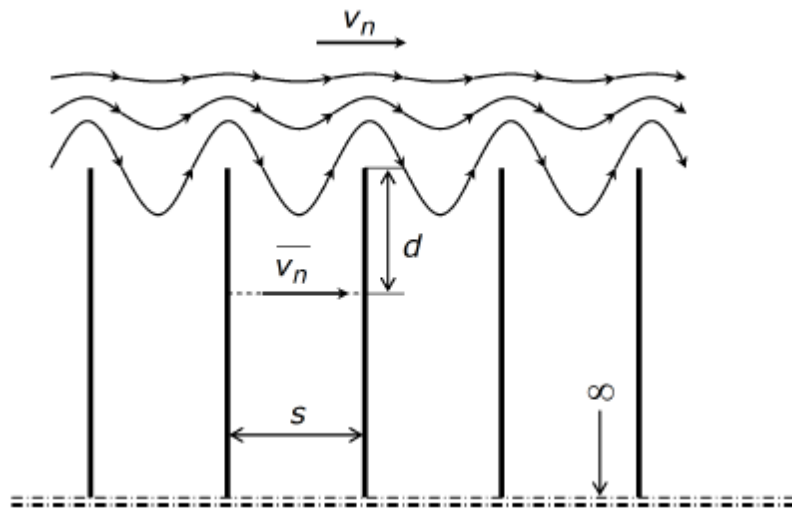
Figure A.4: 2D potential flow along a row of semi-infinite parallel plates as used by Prandtl in the derivation of the tip loss factor F

To put this in a form that is directly related to the propeller vortex sheet geometry, distance d is replaced by $R - r$ and s by the distance between the two succeeding tip vortices (index t):

$$s = \frac{2\pi R}{B}\sin\left(\varphi_{t_3}\right) \qquad (A.22)$$

where index 3 again indicated plane 3 far downstream of the disk. Thus for a circle with radius r:

$$\frac{\overline{v_{a_3}}}{v_{a_3}} = \frac{\overline{v_{t_3}}}{v_{t_3}} = F \tag{A.23}$$

where:

$$F = \frac{2}{\pi}\arccos(e^{-f}) \tag{A.24}$$

and:

$$f = \frac{\pi(R - r)}{\frac{2\pi R}{B}\sin(\varphi_t)} = \frac{B(1 - \xi)}{2\sin(\varphi_t)} \tag{A.25}$$

where $\xi = r/R$. It should be noted that for the limiting case were the propeller is lightly loaded the induced velocities become very small.

4. Blade Element Theory

As indicated before, in order to estimate the performance of the propeller and assess the slipstream that is generated it is necessary to examine the aerodynamics of the blade in detail. A relatively simple method of predicting the performance of a propeller is the use of blade element theory. The propeller is divided into a number of independent sections along the blade spanwise direction.
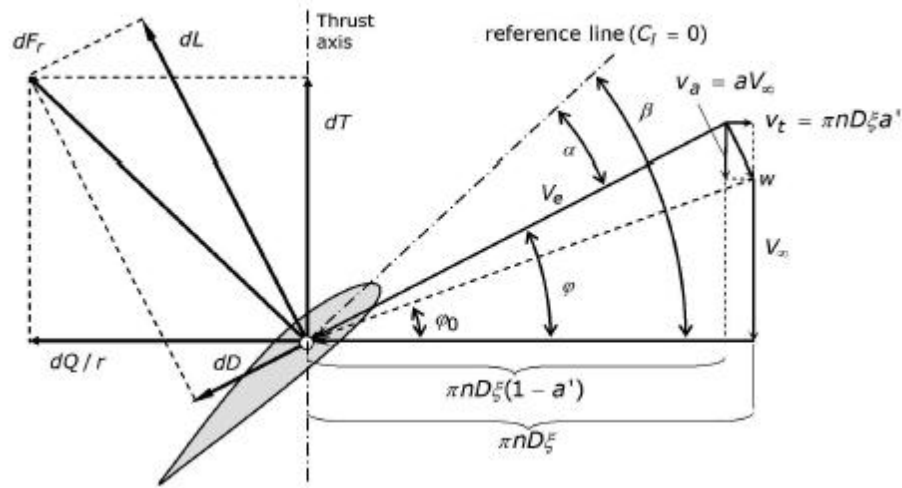
Figure A.5: Velocity and force diagram acting on a propeller blade section

Fig. A.5 contains the velocity and force diagram for a blade section positioned at radius , r. Before the forces acting on the propeller can be determined from the known airfoil characteristics of the blade sections, it is necessary to calculate the effective velocity, V_e, or equivalent : the induced velocity components, v_a and v_t.

To calculate the induced velocities one could start using the Biot-Savart law in the process of calculating the velocity induced by every single vortex filament in the slipstream. This leads to a rather laborious calculation technique that not necessarily produces more accurate results than the method based on conservation of momentum as sketched hereafter. In case the number of propeller blades is limited the induced velocity components will exhibit a fluctuating character at the location of the propeller disk. This again makes the Biot-Savart techniques complex since unsteady equations have to be solved. However, a very acceptable result is obtained by considering the case that the number of blades $B = \infty$ [24].

Following a simplified conservation of momentum approach only requires the availability of the Prandtl tip loss factor. Considering a circular streamtube, between r and $r + dr$ the conservation law of momentum in axial direction becomes:

$$2\pi r \; dr \; \rho\left(V_\infty + \bar{v}_{a_3}\right) = dT_0' \qquad (A.26)$$

where index 0 refers to the condition were the profile drag of the blade element is zero ($C_d = 0$). The right hand side, dT_0', is the force acting on the fluid inside the tube element which is equal to B times the force acting on the blade element. In tangential direction we may write:

$$2\pi r \; dr \; \rho\left(V_\infty + \bar{v}_{a_3}\right) = \frac{dQ_0'}{r} \qquad (A.27)$$

The attribute $C_d = 0$ is essential since the left hand sides of the equations (A.26) and (A.27) are based on an idealized vortex system in which the effect of the profile drag is not represented for the moment. With the lift force dL acting on the blade element the thrust and torque can also be expressed as:

$$dT_0' = B \; dL \cos(\varphi) = BC_l \frac{1}{2}\rho V_e^2 c \; dr \cos(\varphi) \qquad (A.28)$$

$$\frac{dQ_0'}{r} = B \; dL \sin(\varphi) = BC_l \frac{1}{2}\rho V_e^2 c \; dr \sin(\varphi) \qquad (A.29)$$

where dL denotes the lift force acting on an element of a single propeller blade. The velocity V_e can be written as :

$$V_e = \frac{V_\infty + v_a}{\sin(\varphi)} = \frac{V_\infty(1 + a)}{\sin(\varphi)} \qquad (A.30)$$

or

$$V_e = \frac{\Omega r - v_t}{\cos(\varphi)} = \Omega r \frac{(1 - a')}{\cos(\varphi)} \qquad (A.31)$$

The axial and tangential velocity ratio at the location of the propeller and at cross section 3 may be approximated by:

$$\frac{\overline{v_a}}{v_a} = \frac{\overline{v_t}}{v_t} = \frac{\overline{v_{a_3}}}{v_{a_3}} = \frac{\overline{v_{t_3}}}{v_{t_3}} = F \qquad (A.32)$$

In theory $\overline{v_a}/v_a$ will be different from $\overline{v_{a_3}}/v_{a_3}$ due to the influence of the bound circulation on the blades and the "development" of the trailing vortex system that is infuenced by self-induction. However, the angle φ_{w_3} will differ only slightly from φ_{w_2}. This is especially the case for lightly loaded propellers. Accepting the value of F as calculated by the method described in section A.4, the blade element model now proceeds as follows.

Substitution of equations (A.32) and (A.28) into equation (A.26) leads to:

$$4\pi r \rho (V + F v_a) F v_a = B C_l \frac{1}{2} \rho V_e^2 c \, dr \cos(\varphi) \qquad (A.33)$$

Thus:

$$\frac{V + F v_a}{V + v_a} \frac{F v_a}{V + v_a} = \frac{B c}{2\pi r} \frac{C_l \cos(\varphi)}{4 \sin^2(\varphi)} \qquad (A.34)$$

In an analogue way for the tangential direction we find:

$$\frac{V + F v_a}{V + v_a} \frac{F v_t}{\Omega r - v_t} = \frac{B c}{2\pi r} \frac{C_l}{4 \cos(\varphi)} \qquad (A.35)$$

For the known values of V, Ω, r, B, β and c equations (A.34) and (A.35) constitute a relation between the induced velocities v_a; v_t and the angle φ (or α). The value of the lift coefficient C_l for all blade sections is known at every angle of attack from a look-up table. Remember that α

is simply found from $\alpha = \beta - \varphi$. The Prandtl tip-loss-factor, F, is known for a given value of φ but an initial guess is needed for φ_{t_3} which is unknown at the start of the calculation process.

For a lightly and optimal loaded propeller $V + w_3$ may be approximated as being independent of r. Hence:

$$tan(\varphi_{t_3}) = \frac{r}{R} tan(\varphi_{w_3}) \qquad (A.36)$$

Using the assumptions based on the use of the Prandtl tip-loss-factor it is beneficial and acceptable to start the calculation process with $sin(\varphi_{tw_3}) = \frac{r}{R} sin(\varphi_{w_3})$.

Thus factor f in equation (A.25) becomes:

$$f = \frac{B\left(1 - \frac{r}{R}\right)}{\frac{2r}{R} sin(\varphi_{w_3})} \qquad (A.37)$$

Initially the relation between φ_{w_3} and φ must be predicted appropriately. For lightly loaded propellers a start value of $\varphi_{w_3} = \varphi$ is acceptable. For a non-zero flight speed, V_∞, equations (A.34) and (A.35) may be put in the form :

$$\frac{1 + Fa}{1 + a} \frac{Fa}{1 + a} = \sigma \frac{C_l \cos(\varphi)}{4 sin^2(\varphi)} \qquad (A.38)$$

$$\frac{1 + Fa}{1 + a} \frac{Fa'}{1 - a'} = \sigma \frac{C_l}{4 \cos(\varphi)} \qquad (A.39)$$

where $\sigma = B c/2\pi r$ denotes the solidity of the propeller blade section. With equation (A.38) the axial induction factor can be determined for all values of φ. Subsequently the value of the tangential induction factor, a', can be calculated with equation (A.39).

In cases where the axial velocity increase, v_a, is small compared to the undisturbed flow velocity (i.e. cruise condition), the term $(1 + Fa)/(1 + a)$ may be approximated by 1. Thus equations (A.38) and (A.39) become:

$$\frac{a}{1+a} = \sigma \frac{C_l \cos(\varphi)}{4F sin^2(\varphi)} \qquad (A.40)$$

$$\frac{a'}{1-a'} = \sigma \frac{C_l}{4F cos(\varphi)} \qquad (A.41)$$

These expressions relate the induction factors a and a' with the flow angle φ. To calculate these three variables a third equation is needed which fluxes the operating condition of the propeller. For this purpose the advance ratio, J, is used :

$$J = \pi\xi \frac{V(1+a)(1-a')}{\Omega r(1-a')(1+a)} = \pi\xi \tan(\varphi) \frac{1-a'}{1+a} \qquad (A.42)$$

Equations (A.40), (A.41) and (A.42) now have to be solved for a, a' and φ by performing an iterative process.

In reality the propeller blade section, beside the lift force, produces a profile drag force which means that equations (A.28) and (A.29) have to be rewritten as :

$$dT_0' = B(C_l \cos(\varphi) - C_d sin(\varphi)) \frac{1}{2}\rho V_e^2 c\, dr \qquad (A.43)$$

$$\frac{dQ_0'}{r} = B(C_l \sin(\varphi) + C_d cos(\varphi)) \frac{1}{2}\rho V_e^2 c\, dr \qquad (A.44)$$

With $Ve = V(1 + a)/\sin(\varphi)$ and $dP = \Omega dQ$ and the definitions for the thrust and power coefficient, the equations (A.43) and (A.44) can be rewritten :

$$\frac{dC_T}{d\xi} = J^2 B \frac{c}{R} \frac{(1+a)^2}{8 sin^2(\varphi)} (C_l \cos(\varphi) - C_d sin(\varphi)) \qquad (A.45)$$

$$\frac{dC_P}{d\xi} = J^2 \frac{r}{R} B \frac{c}{R} \frac{\pi(1+a)^2}{8sin^2(\varphi)} (C_l \sin(\varphi) + C_d \cos(\varphi)) \qquad (A.46)$$

and the propeller efficiency can be calculated from :

$$\eta = \frac{C_T}{C_P} J \qquad (A.47)$$

With these equations the system that determines the propeller characteristics is now complete. As input parameters we need the blade geometry (chord and blade angle distribution) and the characteristics of the blade airfoil sections. The latter may be taken either from experiments or calculations on 2D-airfoils. Two factors that need further attention before appropriate lift and drag coefficients can be used in the BEM-analysis, as discussed above, are the effect of compressibility and the tip relief effect (TRE).

5. Effect of Compressibility

In contrast to the Mach numbers that are attained on the wing, the local propeller blade section Mach number may be quite high. At a flight speed of $V = 100$ m/s with a 3.65m diameter propeller running at an RPM of 2200 in standard atmosphere at height of $h = 3000$m the tip Mach number already reaches a value of $M = 0.815$. This means that the lift and drag characteristics taken from experiments or calculations under incompressible conditions should be corrected for compressibility effects. For Mach numbers below 0.7 the Prandtl-Glauert correction may be applied, leading to acceptable results:

$$C_{x_{corr}} = \frac{C_x}{\sqrt{1 - M_\infty^2}} \qquad (A.48)$$

where the coefficient C_x is either the lift or the drag coefficient of the blade airfoil section. For $M > 0.7$ the airfoil characteristics have to be corrected through dedicated prediction codes or should directly be taken from appropriate high speed windtunnel tests.

6. Tip Relief Effect

Experiments on rotating propeller blades have shown that the pressure distribution and the local lift curve slope, $C_{l\alpha}$, may diffeer significantly from the 2D-airfoil data of the particular blade section [26]. This phenomenon can be attributed to the existence of the centrifugal and Coriolis forces that act on the boundary layer flow over the propeller blades. The total effect is comparable to a favorable pressure gradient. Fig. A.6 shows the situation on the propeller blade.
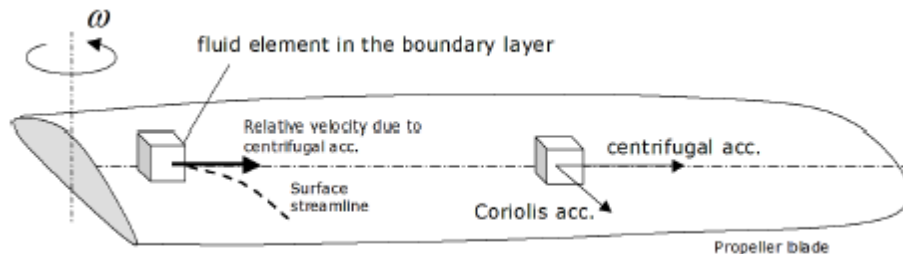

Figure A.6: Effect of the Coriolis force on the propeller blade boundary layer

We see that material in the boundary layer that moves with the propeller is swept outward due to the centrifugal acceleration while the Coriolis force depends on the direction of the relative velocity vector, V_r. In case V_r is directed outward due to the action of the

centrifugal acceleration, the Coriolis force will be in the direction of the blade trailing edge, as indicated in Fig. A.7.
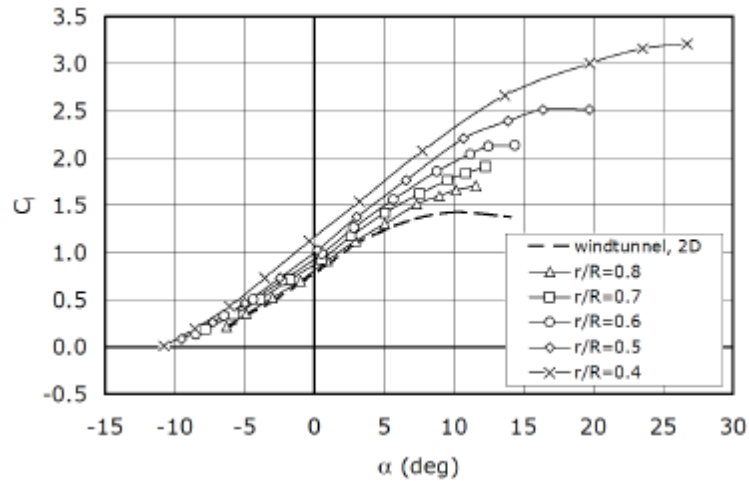

Figure A.7: Example of the effect of the blade rotation on the sectional lift coefficient of the propeller blade [27]

Comparison of results of boundary layer calculations of rotating blades with those of 2-dimensional stationary ones showed that the secondary flow induced over the rotating blades has strong effects by suppressing the boundary layer growth which results in delayed transition and separation of the boundary layer [26].

An indication of these effects can be found from the measurements of Himmelskamp [27]. Himmelskamp performed measurements on a rotating propeller and determined the local blade section lift coefficients from surface pressure measurements.

Some of his results are reproduced in Fig. A.7 where the C_l-α curves at various radial stations are compared with 2D windtunnel data. A significant increase in lift coefficient can be found going from the tip to the hub, combined with separation delayed to a higher angle of attack.

112

These effects on the lift curve slope can be explained by the influence of the Coriolis force acting on the boundary layer material. Additionally the centrifugal force transports boundary layer material away from the hub. The resulting boundary layer at the inner portion of the blade thus becomes thinner, leading to favorable C_l–α behavior.

To incorporate these effects in the calculation process of the propeller forces the lift coefficients should somehow be corrected. This procedure however is not straightforward since the correction needed depends very much on the state of the local boundary layer. Several attempts have been made to derive a convenient correction formula. A quite acceptable method was developed by ECN and NLR as described by Bosschers [28] in the form of an empirical formula. This method is based on the work of Snel [29] on incompressible boundary layers. The method proposed is particularly suited for high lift conditions were separated flow is affected by the Coriolis force pressure force and shear stresses. An acceptable correlation between the predicted and the measured data was found for some typical wind turbine applications. The empirical relation for the rotational effects on the flow in the stall region is based on the difference between the 2D inviscid and the viscous lift curve slope, Cl_α, as expressed by:

$$C_{l_{3D,rot}} = C_{l_{2D,vis}} + \left(C_{l_{2D,vis}} - C_{l_{2D,inv}} \right) \cdot f_c(c/R) \qquad (A.49)$$

where $C_{l_{3D,rot}}$ is the local blade lift coefficient on the rotating propeller, $C_{l_{2D,vis}}$ and $C_{l_{2D,inv}}$ are the 2D lift coefficients for the viscous and the inviscid flow respectively.

The function $f_c(c/R)$ is a function of the chord distribution. Although it is evident that f_c will be affected by parameters like the airfoil shape, local Reynolds number, etc. the following approximation produces interesting results :

$$f_c(c/R) = \tanh(3(c/R)^2) \qquad (A.50)$$

The procedure as described above should however be treated carefully since the boundary layer transition process may influence the lift enhancement process [30].

The resulting decrease in lift and increase in skin friction drag complicates the effect of blade rotation which in general is thought to increase lift and decrease drag for the inboard blade sections.

7. Nacelle Effects

In most cases the nacelle has a relative large dimension compared to the blade root chord and the propeller tip radius. The presence of the nacelle therefore alters the flow field by changing the axial flow velocity, u, and the radial flow velocity, v_r, as sketched in Fig. A.8.
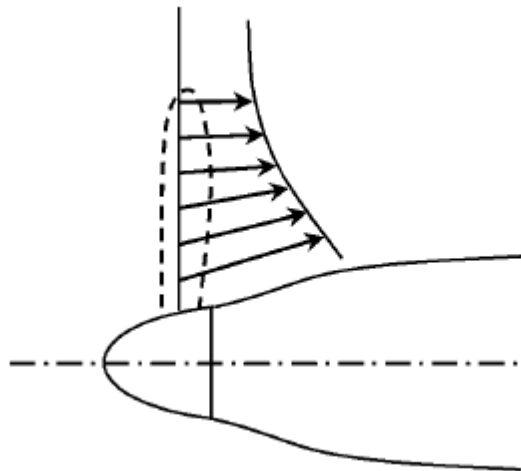
Figure A.8: Axial velocity increase due to the blockage effect of the nacelle

To get a first estimate of the performance of the installed propeller the axial force acting on the nacelle can be estimated by calculating the change in static pressure upstream and downstream of the thrusting propeller. For this purpose the approximate relation as presented by Koning [31] can be used. Downstream of the propeller, the static pressure change becomes:

$$\frac{\Delta p}{\frac{1}{2}\rho V_\infty^2} = \frac{T_c}{2}\left(1 - \frac{x/R}{\sqrt{(x/R)^2 + 1}}\right) \qquad (A.51)$$

while upstream:

$$\frac{\Delta p}{\frac{1}{2}\rho V_\infty^2} = -\frac{T_c}{2}\left(1 + \frac{x/R}{\sqrt{(x/R)^2 + 1}}\right) \qquad (A.52)$$

Here x is the distance downstream of the propeller. The axial pressure gradient that exists causes a buoyancy force on the nacelle that can be calculated with the known area distribution $S_n(x)$:

$$\Delta C_D = \frac{1}{S_{ref}}\int_0^{L_n}\left(\frac{\Delta p}{\frac{1}{2}\rho V_\infty^2}\right)\left(\frac{dS_n}{dx_n}\right)dx_n \qquad (A.53)$$

where S_{ref} is the reference area used in the calculation of drag coeffcients, L_n is the nacelle length. The net thrust of the propeller-nacelle configuration then becomes:

$$C_{T_n} = C_T\left(1 - \frac{S_{ref}}{\pi R^2}\Delta C_D\right) \qquad (A.54)$$

8. Propeller at angle of attack

The effective velocity vector at the blade section in the propeller axis reference system is the sum of the undisturbed flow vector and the induced flow vectors induced by all aircraft parts (index ap) and by the propeller itself (index p) :

$$\left(V_{eff}\right)_p = (V_\infty)_p + \left(V_{ap}\right)_p + \left(V_p\right)_p \qquad (A.55)$$

This velocity vector is defined in the orthogonal propeller axis system, denoted by $(\blacksquare)_p$. To find the velocity vector in the cylindrical propeller axis system, denoted by $(\blacksquare)_{pc}$, the velocity vectors have to be transformed from the global axis system. Thus:

$$(V)_{pc} = M \cdot N \cdot V_{gl} \qquad (A.56)$$

where M and N are the transformation matrices respectively from global to orthogonal propeller axis system and from orthogonal to cylindrical propeller axis system. Index gl denotes the global axis system.

The general form of the matrix M is:

$$M = \begin{pmatrix} i \cdot i_p & j \cdot i_p & k \cdot i_p \\ i \cdot j_p & j \cdot j_p & k \cdot j_p \\ i \cdot k_p & j \cdot k_p & k \cdot k_p \end{pmatrix} \qquad (A.57)$$

where $i,\ j,\ k$ and $i_p,\ j_p,\ k_p$ are the unit vectors in the global and the orthogonal axis system respectively and the vector product merely represent the cosine of the angles between the different axes. The matrix N simply becomes:

$$N = \begin{pmatrix} 1 & 0 & 0 \\ 0 & \sin(\theta) & \cos(\theta) \\ 0 & \cos(\theta) & -\sin(\theta) \end{pmatrix} \qquad (A.58)$$

In flight there will generally be some angle of attack to the free stream and therefore a component of the forward speed will act in the plane of the propeller that will combine with the rotational component to produce a periodic variation of the angle of attack as the propeller rotates. To get some understanding of the resulting effects on the propeller performance assume the propeller flow is only affected by a plain α_p-effect.

In this case M becomes:

$$M = \begin{pmatrix} \cos(\alpha_p) & 0 & -\sin(\alpha_p) \\ 0 & 1 & 0 \\ \sin(\alpha_p) & 0 & \cos(\alpha_p) \end{pmatrix} \qquad (A.59)$$

and the effective velocity vector can be written as:

$$V_{eff} = \begin{pmatrix} V_\infty(1+a)\cos(\alpha_p) \\ V_\infty \sin(\alpha_p)\cos(\theta) \\ V_\infty sin(\alpha_p)\sin(\theta) + \pi n D\xi(1-a') \end{pmatrix} \qquad (A.60)$$

This means that the expressions for the local thrust and power of the blade element change to:

$$\frac{dC_T}{d\xi} = J^2 B \frac{c}{R} \frac{(1+a)^2}{8sin^2(\varphi')}(C_l \cos(\varphi') - C_d\sin(\varphi'))cos^2(\alpha_p) \qquad (A.61)$$

$$\frac{dC_P}{d\xi} = J^2 \frac{r}{R} B \frac{c}{R} \frac{\pi(1+a)^2}{8sin^2(\varphi')}(C_l \sin(\varphi') + C_d\cos(\varphi'))cos^2(\alpha_p) \qquad (A.62)$$

with:

$$\tan(\varphi') = \frac{V_\infty(1+a)\cos(\alpha_p)}{V_\infty sin(\alpha_p)\sin(\varphi') + \pi n D\xi(1-a')} \qquad (A.63)$$

The coefficients now show a periodic variation which will cause an asymmetric loading over the propeller disk and moments about the axes normal to the propeller axis.

Appendix B

Slipstream contraction

1. Introduction

Due to the velocity increase induced by the propeller the slipstream will contract.

This is an important aspect as this results in a region of influence that is smaller than the volume occupied by the cylinder with constant radius R. Besides this the slipstream contraction causes an inflow angle that affects the local angle of attack of the wing.

An attractive way to study the slipstream contraction is to realize that its form is determined by the forces that the propeller exerts on the air. In view of the fact that in general the problem in its most general form is very complex it is beneficial to simplify the propeller again as a this disk. Realizing that the function of the propeller is to generate a force in x-direction it is expected that the axial components of the general force system will dominate the slipstream geometry. Accepting the simplification that these axial forces are constant over the propeller disk we arrive at the definition of the so-called "ideal propeller".

To be able to find the velocities that in their turn determine the slipstream boundary and contraction the flow is simplified even further by neglecting the effects of viscosity and compressibility.

A simple procedure that can be followed to find a first estimate for the contraction, is described here.

The boundary of the slipstream can be modeled as a body of revolution with a radius, R_s, that changes with the axial coordinate, x. By considering the law of continuity the amount of fluid that has passed the propeller disc is equal to the amount found in all cross section of the slipstream. With the acceptance of a uniform velocity distribution this leads to:

$$\pi R_s^2 V_\infty (1 + v_x) = \pi R^2 V_\infty (1 + a) \qquad (B.1)$$

Here a is the axial inflow factor representing the axial velocity increment at the location of the disc. Its value follows from the axial momentum theory of propellers, in which the tangential velocity component, v_t, is neglected:

$$a = \frac{1}{2}\left(-1 + \sqrt{1 + \frac{8}{\pi} T_c} \right) \qquad (B.2)$$

For a given value of the axial inflow factor the contraction ratio, R_s/R, depends on the streamwise development of the axial velocity perturbation, $v_x(x)$. This function can be determined by considering the Navier-Stokes equations for inviscid, incompressible flow with only an external force in x-direction active. For small perturbations due to the propeller:

$$\rho V \frac{\partial v_x}{\partial x} = -\frac{\partial p}{\partial x} + F_x \qquad (B.3)$$

$$\rho V \frac{\partial v_y}{\partial y} = -\frac{\partial p}{\partial y} \qquad (B.4)$$

$$\rho V \frac{\partial v_z}{\partial z} = -\frac{\partial p}{\partial z} \qquad (B.5)$$

$$\frac{\partial v_x}{\partial x} + \frac{\partial v_y}{\partial y} + \frac{\partial v_z}{\partial z} = 0 \qquad (B.6)$$

The external force only acts on the disc while the pressure, apart form the propeller disc surface, is continuous everywhere. By eliminating the velocity components, v_x, v_y and v_z, from equations (B.3)-(B.5) combined with equation (B.6) the Laplace equation for the pressure is found:

$$\frac{\partial^2 p}{\partial x^2} + \frac{\partial^2 p}{\partial y^2} + \frac{\partial^2 p}{\partial z^2} = 0 \qquad (B.7)$$

The potential function for p can now be obtained by a distribution of doublets of strength (p_2 - p_1) per unit disc area. Point 1 is taken in front of the propeller disc and point 2 directly behind it. The pressure in a point Q located at a distance l_Q from any point on the disc then becomes:

$$p_Q = \frac{p_2 - p_1}{4\pi} \int_S \frac{\partial}{\partial n}\left(\frac{1}{l_Q}\right) dS \qquad for\ l_Q > 0 \qquad (B.8)$$

Rewriting equation (B.8) in cylindrical coordinates leads to:

$$p_Q = \frac{p_2 - p_1}{4\pi} \int_0^R \int_0^{2\pi} r_1 \frac{\partial}{\partial x_1}\left(\frac{1}{l_Q}\right) dr_1 d\theta_1 \qquad (B.9)$$

The flow inside and outside the slipstream has a velocity potential and it shows a discontinuity in v_x at the disc. Let the value of p at $r = 0$ be representative for the flow in the slipstream (uniform velocity distribution). In this case the expression for the pressure becomes:

$$p = \frac{p_2 - p_1}{4\pi} \int_0^R \int_0^{2\pi} \frac{x r_1}{[r_1^2 + x^2]^{3/2}} dr_1 d\theta_1 = \frac{p_2 - p_1}{2}\left(\frac{x}{\sqrt{x^2}} - \frac{x}{\sqrt{R^2 + x^2}}\right) \qquad (B.10)$$

For $x > 0$ this leads to:

$$p = \frac{p_2 - p_1}{2}\left(1 - \frac{x}{\sqrt{R^2 + x^2}}\right) \qquad (B.11)$$

Integrating the equation (B.3) and combining this with equation (B.11) results in:

$$v_x = \frac{p_2 - p_1}{2\rho V_\infty}\left(1 + \frac{x}{\sqrt{R^2 + x^2}}\right) \qquad (B.12)$$

which represents the streamwise development of the axial induced flow velocity in the slipstream. Combining equation (B.1) and equation (B.11) now determines the slipstream radius as a function of the streamwise x-coordinate:

$$\pi R_s^2 V_\infty\left(1 + \frac{p_2 - p_1}{2\rho V}\left(1 + \frac{x}{\sqrt{R^2 + x^2}}\right)\right) = \pi R^2 V_\infty(1 + a) \qquad (B.13)$$

At $x = 0$ the axial component becomes aV, hence the term $(p_2 - p_1)/2\rho V$ can be replaced by aV. Working out equation (B.13) results in the contraction ratio, R_s/R:

$$\frac{R_s}{R} = \sqrt{\frac{1 + a}{1 + a\left(1 + \frac{x}{\sqrt{R^2 + x^2}}\right)}} \qquad (B.14)$$

Accepting the assumptions made with respect to the actuator disc with uniform axial force distribution over the disc, expression (B.14) produces very acceptable values of the contraction ratio. It should be noted however that the introduction of a nacelle has strong effects on the contraction due to the mirror vortex system inside the nacelle geometry. Mindless usage of equation (B.14) then leads to erroneous results.

List of References

[1] Agarwal R.K., and Deese, J.E., "Euler Calculations for Flowfield of a Helicopter Rotor in Hover", AIM 4th Applied Aerodynamics Conference.

[2] A. Hellsten, "New Advanced k-ω Turbulence Mode For High-Lift Aerodynamic", 42nd AIAA Aerospace Sciences Meeting and Exhibit.

[3] B. Chen, F. Stern, "Computational fluid dynamics of four-quadrant marine-propulsor flow", Journal of Ship Research 43 (4), pp. 218–228.

[4] D. Biermann and Eiiwin P. Haetman, "Wind tunnel tests of four- and six-blade single- and dual-rotating tractor propellers", NACA Report n.747.

[5] Hathway, M.D., Chriss, R.M., Wood, J.R., and Strazisar, A.J., "Experimental and Computational Investigation of the NASA Low-Speed Centrifugal Compressor Flow Field", 37th ASME International Gas Turbine Conference.

[6] J. M. Weiss and W. A. Smith, "Preconditioning applied to variable and constant density flows", AIAA Journal, Vol. 33, No 11.

[7] K. S. Majety, "Solutions to the Navier-Stokes equations in a non-inertial reference frame" MS Thesis, Mississippi State University.

[8] L. Djayapertapa et al.,"Time Accurate Methods", GARTEUR AD (AG38/TP154) Report.

[9] Limache, A., and Cliff, E., "Aerodynamic Sensitivity Theory for Rotary Stability Derivatives," Journal of Aircraft, Vol. 37, 2000, pp. 676–683. doi:10.2514/2.2651

[10] Limache, A. C., "Aerodynamic Modeling Using Computational Fluid Dynamics and Sensitivity Equations," Ph.D. Thesis, Virginia Polytechnic Inst. and State Univ., Blacksburg, VA, 2000.

[11] Park, M. A., Green, L. L., Montgomery, R. C., and Raney, D. L., "Determination of Stability and Control Derivatives Using Computational Fluid Dynamics and Automatic Differentiation," AIAA Paper 1999-3136, 1999.

[12] Park, M. A., and Green, L. L., "Steady-State Computation of Constant Rotational Rate Dynamic Stability Derivatives," AIAA Paper 20004321, 2000.

[13] Quilan J, Eaton J, O'Flaherty M., "Computational investigation of propulsion integration effects on wing propeller installation", AIAA Paper 96-0673.

[14] Selmin V, Formaggia L., "A unified approach for the construction of finite element and finite volume discretizations for compressible flow", International Journal on Numerical Methods in Engineering, pp. 1–32.

[15] Wallin, S. & Johansson, A.V., "An explicit algebraic Reynolds stress model for incompressible and compressible turbulent flows", Journal of Fluid Mechanics, Vol. 403, pp. 89-132.

[16] Alexei Y. Poludnenko, Alexei M. Khokhlov, "Computation of fluid flows in non-inertial contracting, expanding, and rotating reference frames" – Journal of Computational Physics.

[17] Chima, R.V., and Yokota, J.W., "Numerical Analysis of Three-Dimensional Viscous Internal Flows," AIM Journal, Vol. 28, No. 5, May 1990, pp. 798-806.

[18] Choi, D. and Knight, C.J, "Computation of 3D Viscous Flows in Rotating Turbomachinery Blades," AIM-89-0323,27th Aerospace Sciences Meeting & Exhibit, January 9-12, 1989, Reno, NV.

[19] Bussing, T.R. and Murman, E.M., "A Finite Volume method for the Calculation of Compressible Chemically Reacting Flows," AIAA Paper 85-0331, January 1985.

[20] Johnston, R., and Sullivan, J. Propeller tip vortex interactions. In 28th Aerospace Sciences Meeting (Reno (USA), January 8-11 1990), no. AIAA 90-0437, AIAA.

[21] Tsai, T., de Jong, F., and Levy, R. Computation of the tip vortex flow field for advanced aircraft propellers. Contractor Report CR 182179, NASA, NASA Lewis Research Center (USA), 1988.

[22] Marinus, B., Bosschaerts, W., and Roger, M. Aerodynamic study of a 'humpy' propeller. In 46th Symposium of Applied Aerodynamics organized by 3AF (Orléans (France), March 28-30 2011), Association Aéronautique et Aérospatiale de France.

[23] Von Mises, R., Theory of Flight, Dover Publishing, 1959.

[24] Durand, W.F.: Aerodynamic Theory, Volume IV, Divisions J-M, Springer Verlag, 1935, p. 169-430.

[25] Prandtl, L. and Betz, A.: Schraubenpropeller mit geringstem Energieverlust, Goettinger Nachrichten, 1919.

[26] Bak, C. ; Fuglsang, P. ; Sørensen, N.N. ; Aagaard, M. ; Shen, W.Z. and Sørensen, J.N.: Airfoil characteristics for wind turbines, Risø-R-1065(EN), 1999.

[27] Himmelskamp, H.: Profiluntersuchungen an einem umlaufendenn propeller, Diss. Goettingen, 1945, Max-Planck Institut fuer Stroemungsforschung, Goettingen, Rep. No.7.

[28] Bosschers, J.: Validation of the helicopter code HERO, NLR TP 93418 L, 1993.

[29] Snel, H.: Scaling laws for the boundary layer flow on rotating wind turbine blades, Proceedings of the 4th IEA Symposium on the Aerodynamics of Wind turbines, Rome, 1990.

[30] Bosschers, J. ; Montgomerie, B. ; Brand, A.J. and Rooy, R.P.J.O.M. van: Influence of blade rotation on the sectional aerodynamics of rotational blades, NLR TP 96523 L, Sept. 1996.

[31] Koning, C.: Influence of the propeller on other parts of the airplane structure, In: Durand, W.F. (Ed.) Aerodynamic Theory, Division M, Vol IV.

[32] Prandtl, L. and Tiedjens, O.: Applied Hydro- and Aeromechanics, Dover Publ., New York, 1934.